



MASTER THESIS

THEORETICAL ASTROPHYSICS

**“Modelling turbulent gases with Finite Volume
and Discontinuous Galerkin methods ”**

submitted by

JOHANNES MARKERT

in fulfilment of the requirements for the academic degree

MASTER OF SCIENCE



I. PHYSIKALISCHES INSTITUT

Acknowledgment

First and foremost I want to express my debt of gratitude and deep respect to my supervisor, Prof. Dr. Stefanie Walch-Gassner, for inviting me to her workgroup and for her excellent guidance. Her invaluable advice, far-reaching insights and open mind were much appreciated. She granted me a lot of freedom to pursue my own interests and always had a friendly ear for any thought or idea. Even when they were stupid, retrospectively.

Likewise I want to thank Prof. Dr.-Ing. Gregor Gassner who encouraged me to write this thesis in the first place.

Many thanks to PD Dr. Volker Ossenkopf for co-reviewing my work despite his busy schedule.

I thank my family for their love, support and unlimited patience.

Examinee

Johannes Markert
I. Physikalisches Institut
Universität zu Köln
markert@ph1.uni-koeln.de

First Supervisor

Professor Dr. Stefanie Walch-Gassner
I. Physikalisches Institut
Universität zu Köln
walch@ph1.uni-koeln.de

Second Supervisor

PD Dr. Volker Ossenkopf
I. Physikalisches Institut
Universität zu Köln
ossk@ph1.uni-koeln.de

Declaration of Authorship/Selbstständigkeitserklärung

Declaration of Authorship I hereby certify that this thesis has been composed by me and is based on my own work, unless stated otherwise. No other person's work has been used without due acknowledgment in this thesis. All references and verbatim extracts have been quoted, and all sources of information, including graphs and data sets, have been specifically acknowledged. This work was neither published nor sent, in part or whole, to any other examination committee. The submitted thesis in digital form is identical to the printed version.

Selbstständigkeitserklärung Hiermit versichere ich an Eides statt, dass ich die vorliegende Arbeit selbstständig und ohne die Benutzung anderer als der angegebenen Hilfsmittel angefertigt habe. Alle Stellen, die wörtlich oder sinngemäß aus veröffentlichten und nicht veröffentlichten Schriften entnommen wurden, sind als solche kenntlich gemacht. Die Arbeit ist in gleicher oder ähnlicher Form oder auszugsweise im Rahmen einer anderen Prüfung noch nicht vorgelegt worden. Ich versichere, dass die eingereichte elektronische Fassung der eingereichten Druckfassung vollständig entspricht.

Location, Date

Signature

Abstract/Zusammenfassung

Abstract Finite Volume methods (FV) are an established numerical scheme for astrophysical turbulence simulations of molecular clouds and interstellar media (ISM). ISM simulations are characterized by supersonic turbulent flows who impose very high demands on the numerical scheme with regards to robustness and accuracy. The widely adopted fluid simulation framework FLASH¹ provides several specialized FV solvers, meeting the requirements imposed by supersonic flows.

Astrophysical turbulences show a rich variety of structure over huge time and length scales. They play a major role in several processes such as the formation of dense structures and stars as well as the stability of molecular clouds. The desire to study and understand the underlying physics has driven generations of scientists to develop more advanced numerical schemes with higher resolution capabilities. However, FV methods provide limited space for improvement due to their lack in degrees-of-freedom.

By contrast to FV schemes, modern higher-order discontinuous Galerkin methods (DG) promise to provide faster convergence rates, smaller diffusion and dispersion errors, better data volume-over-surface ratio for efficient parallel processing and better input/output handling due to the smaller volume of data. Their drawback is the impracticality in resolving shocks.

In this work, we propose a hybrid scheme which combines the accuracy of DG with the stability of FV schemes. In order to provide a proof-of-concept, the DG implementation FLEXI² is augmented to support supersonic isothermal turbulence simulations, governed by the compressible Euler equations.

A comparative study of driven and decaying turbulence setups ensures that the hybrid scheme models turbulent flows correctly. Widely adopted methods of turbulence statistics, such as density/velocity PDFs and powerspectra, give an insight into the distribution of mass, velocity and energy from large to small length scales. Well-established astrophysics solvers integrated into FLASH, namely PPM, Bouchut3 and Bouchut5, serve as a reference.

¹<http://flash.uchicago.edu/site/flashcode/>

²<https://www.flexi-project.org>

Zusammenfassung Finite Volumen Verfahren (FV) sind ein etablierter numerischer Lösungsansatz für astrophysikalische Turbulenzsimulationen von Molekülwolken und interstellaren Medien (ISM). ISM-Simulationen sind charakterisiert durch turbulente Strömungen im Überschallbereich. Das stellt höchste Anforderungen an das numerische Verfahren hinsichtlich Robustheit und Genauigkeit. Die weithin genutzte Strömungssimulationssoftware FLASH¹ bietet spezialisierte FV-Löser, die den Anforderungen supersonischer Strömungen gerecht werden.

Astrophysikalischen Strömungen zeigen eine reiche Vielfalt an Strukturen über große Zeiträume und räumliche Ausdehnungen hinweg. Sie spielen eine wichtige Rolle in vielen Prozessen, wie zum Beispiel die Formung von hochdichten Strukturen und Sternen oder in der Frage über die Langlebigkeit von Molekülwolken. Den Drang, die dahinterliegende Physik zu studieren und zu verstehen, hat Generationen von Wissenschaftlern angetrieben, immer bessere und genauere numerische Verfahren zu entwickeln. Allerdings bieten FV-Verfahren auf Grund ihrer eingeschränkten Flexibilität wenig Spielraum für Verbesserungen.

Im Gegensatz zu FV-Verfahren, versprechen moderne schrittweise glatte Galerkin-Methoden (DG) schnellere Konvergenz, weniger Diffusion und Dispersion, günstigere Volumen-zu-Oberflächen-Verhältnisse zur guten parallelen Verarbeitung und bessere Lese-/Schreibraten durch geringeres Datenaufkommen. Allerdings sind sie nicht zur Darstellung von Schockwellen geeignet. Im Rahmen dieser Arbeit, stellen wir einen Hybrid-Löser vor, welcher die Präzision von DG- mit der Stabilität von FV-Verfahren vereint. Damit wir die Machbarkeit dieses Konzepts zeigen können, erweitern wir die DG-Implementierung FLEXI² um die Möglichkeit supersonische isothermische Turbulenzen zu simulieren. Die Dynamiken werden durch die kompressiblen Euler-Gleichungen bestimmt.

Vergleichende Studien von getriebener und zerfallender Turbulenz stellen die korrekte Darstellung von Turbulenzen durch den Hybrid-Löser sicher. Gängige Methoden der Turbulenzstatistik, wie Dichte- und Geschwindigkeitsverteilungen sowie Energiespektren, geben Auskunft über die Verteilung von Masse, Geschwindigkeit und Energie auf großen und kleinen Längenskalen. Etablierte, in FLASH integrierte, numerische Löser für die theoretische Astrophysik dienen als Referenz. Zu nennen sind PPM, Bouchut3 und Bouchut5.

¹<http://flash.uchicago.edu/site/flashcode/>

²<https://www.flexi-project.org>

List of Figures

1	Source: [33, p. 8]. Schematic of the Kolmogorov picture of turbulence showing the spatial energy powerspectrum over k . The mathematical definition is given by eqn. 50. The physical meaning of the marked ranges are detailed in the text.	8
2	Source: [47]. Multiple snapshots at successive timesteps of the initial condition $u(x, 0) = 1 - \cos(x)$ evolving under the inviscid Burger's equation (eqn. 60). It eventually develops a shock and becomes multi-valued, which is unphysical.	11
3	Source: [47]. Intersecting characteristics (eqn. 61) of the inviscid Burger's equation (cf. eqn. 60) are symptoms of a shock wave. The left area where lines diverge from each other is called <i>rarefaction</i> fan. Converging lines are part of the <i>compression</i> fan. The region of intersection marks the shock discontinuity, where the solution (cf. fig. 2) becomes multi-valued.	12
4	Examples of spurious oscillation of the discontinuous Galerkin method solving the one-dimensional advection equations with a discontinuous initial condition. The domain is divided into 50 elements each containing a third-order polynome. Gauss and Gauss-Lobatto are two types of distributing interpolation nodes within each element (cf. sec. 3.4).	12
5	The one-dimensional Lagrange polynome of third order ($N_p = 3$) needs four anchor nodes with their associated values in order to approximate the exact function. Note the minor deviation from the original. This is the interpolation error. Beyond the fringes the Lagrange polynome goes to infinity.	15
6	Early-stage snapshot taken immediately after first-time turbulent forcing on the first three modes. The simulation was done in dimensionless units.	21
7	Shell-averaged velocity powerspectrum (cf. sec. 2.2.1) obtained from the velocity (or Mach number in this case) field in fig. 6. The solvers from FLEXI are shown. Obviously, there is a small difference (consider log-log scale!) between the FV-only and hybrid schemes. The distorted spectra on larger modes might be a sign of already emerging oscillations.	22
8	Fully developed Mach-10 turbulence snapshot, simulated with Bouchut5. Forcing was applied on the first three modes and the picture was taken after four crossing times. The formerly smooth large scale waves in fig. 6 compress and smash into each other, yielding tenuous filaments.	22
9	First four expansion modes for the Lagrange and the Legendre basis. They are related by a coordinate transformation from <i>nodal</i> to <i>modal</i> space. The presence of higher modes in modal space signifies a strongly oscillating interpolant in nodal space.	23
10	Pressure and Mach Number slices of a Mach-10 driven turbulence similar to fig. 8. Below are the <i>smoothness</i> indicators s_A (eqn. 93 and s_B (eqn. 94) derived from the pressure.	25
11	Probability Distribution of <i>smoothness</i> indicators s_A (eqn. 93 and s_B (eqn. 94) in a Mach-10 driven turbulence shown in fig. 10. Due to the high spike of indicator A, it is well-suited for distinguishing strong shocks in the pressure field. A more detailed explanation is provided in the text.	26

12	Two finite elements containing four cells/volumes. From top to bottom: Gauss-Lobatto nodes ($N_p = 3$), Gauss nodes ($N_p = 3$), body-centered and face-centered nodes. DG schemes are defined on Gauss and Gauss-Lobatto nodes while FV methods anchor their data at the center of the volumes/cells (body-centered). The exchange of information (flux functions: cf. sec. 2.4.3) happens at the cell boundaries (face-centered).	26
13	Example of a two-dimensional exact third-order Lagrange interpolation of a second-order polynomial. The relative error $\Delta_{\text{RMS}} = 0.000000\%$ (cf. eqn. 96) is below machine precision.	27
14	Column densities plots of interpolated supersonic (Mach 10) turbulence (see fig. 8) from FLASH to FLEXI. Left side: The density is interpolated via a third-order (four nodes per element) Lagrange interpolation as described in the text. The relative interpolation error is estimated as $\Delta_{\text{RMS}} = 0.118763 \approx 12\%$ (cf. eqn. 96). Right side: The interpolation can be improved by introducing a Gaussian blur before the interpolation step: $\Delta_{\text{RMS}} = 0.2808160 \approx 3\%$	28
15	Comparison of one-dimensional density profiles and residuals through a supersonic (Mach 10) turbulent box with original simulation data (flash) and transferred interpolated data (flexi). The density ray is extracted from same data already shown in fig. 8 and fig. 14. The smoothing (before the interpolation) was done via a Gaussian blur which minimizes the residual considerably.	29
16	Canonical density profile at the conventional time $t = 0.2$ with anticipated regions and discontinuities outlined in the plot. The formula of the analytical solution is given in [42].	31
17	Isothermal density profile at conventional time $t = 0.2$ with expected regions and discontinuities outlined in the plot. The contact discontinuity gets suppressed due to polytropic cooling.	31
18	Adiabatic density snapshots depicting the movement of a strong shock wave from left to right. Note: Only the right half of the domain is shown. The pedestal of the rightmost wave ($t_d = 0.04$) has gone out of visible range.	32
19	Isothermal density snapshots depicting the movement of a strong shock wave from left to right. Note: Only the right half of the domain is shown.	33
20	Time evolution of the root-mean-square Mach number \mathcal{M} . After a steep elevation to $\mathcal{M} = 2.5$ the forcing routines keep the solvers from decaying by perpetually injecting small amounts of kinetic energy. Taking a closer look (zoomed picture) a distinct saw-tooth profile appears.	35
21	Turbulent phase: Column Sonic Mach Number and column density along z-axis at the time when forcing is stopped: $t_d = 4.0$	36
22	Turbulent Phase: Column Sonic Mach Number and column density along z-axis at the time when forcing is stopped: $t_d = 4.0$	37
23	Turbulent Phase: Column Sonic Mach Number and column density along z-axis at the time when forcing is stopped: $t_d = 4.0$	38
24	Decay phase: Column Sonic Mach Number and column density along z-axis during decay phase: $t_d = 5.0$	39
25	Decay phase: Column Sonic Mach Number and column density along z-axis during decay phase: $t_d = 5.0$	40
26	Decay phase: Column Sonic Mach Number and column density along z-axis during decay phase: $t_d = 5.0$	41

27	Time evolution of the ratio of Finite-Volume Elements to the total number of elements. The mode switching works both ways, otherwise the plots would reach 100%. At $t_d = 4$ the driving stops and the amount of FV elements declines. <i>Remark</i> The other solvers would stay at 100% since they operate with Finite-Volumes only.	42
28	Time evolution of the energy in the system. The total energy E is the sum of the kinetic \mathcal{K} and internal energy \mathcal{I} : $E = \mathcal{I} + \mathcal{K}$. The internal energy is held constant via polytropic cooling (cf. sec. 3.1).	43
29	Time evolution of the internal energy deprivation by measuring the energy loss right before and after polytropic cooling and dividing by the current dynamic timestep.	44
30	Cumulated energy deprivation collected by the polytropic cooling module. The plots represent the numerical integration (trapezoid rule) of the energy deprivation rates in fig. 29. By the end of the simulation circa 10 times the average energy (cf. fig. 28) was pumped through the system.	44
31	Log-log. scale volume-weighted density PDFs for the turbulent phase $t_d = [2, 4]$ (time-average) and two stages of the decaying phase: $t_d = 4.7$ and $t_d = 6.0$. The faint grey area marks the margin of error of the time-averaging. As the decay progresses, the width of the distributions decrease and the mean values return to the initial density: $\log_{10}(\rho_0) = \log_{10}(1) = 0$. The log-normal fit (dotted lines) were done with eqn. 58.	45
32	Time evolution of the sonic mach number over time derived from the width of the volume-weighted density PDFs via relation eqn. 58 ($b = 2/3$). The dashed line represents the root-mean-square velocity of the PPM solver and serves as a reference. Due to the log-normal relationship, each individual fit yields very low error margins. Hence, the error bars are to small to see.	46
33	Volume-weighted velocity PDFs computed from the checkpoint files for the turbulent phase $t_d = [2, 4]$ (time-average) and two stages of the decaying phase: $t_d = 4.7$ and $t_d = 6.0$. The faint grey area marks the margin of error of the time-averaging. The Midpoint schemes yield strong fluctuation of high velocities during the turbulent phase (cf. fig. 34).	47
34	Maximum root-mean-square velocity over time retrieved from the checkpoint files. The Midpoint schemes show very strong maximum velocity bursts up to Mach 30 and beyond during the turbulent phase.	47
35	Log-log. scale mass-weighted velocity PDF time-averaged over the turbulent phase ($t_d = [2, 4]$). The gray areas mark the margin of error. The solvers from FLASH have a greater amount of slowly moving mass than the others. The bulge on the right side in fig. 33 is gone due to fewer mass in the high-velocity range.	48
36	Powerspectra of the volume-weighted mean kinetic energy field shown for the turbulent phase $t_d = [2, 4]$ (time-average) and two stages of the decay phase: $t_d = 4.5$ and $t_d = 6.0$. When the total kinetic energy declines, the powerspectrum shifts downwards. The inertial range starts at $k = 4$ since forcing is applied on $k_{drive} = 1, 2, 3$. The beginning of the dissipative range is estimated to $k_{diss} \approx 25$ when the spectra start the bend down. The study in [22] came to the same conclusion for equal grid resolution of 512^3	49

37	Powerspectra of the volume-weighted velocity field for the turbulent phase $t_d = [2, 4]$ (time-average) and at the end of the decaying phase $t_d = 6.0$. The inertial range starts at $k = 4$ since forcing is applied on $k_{drive} = 1, 2, 3$. The black solid line marks the expected slope $m_{vw} = -19/9$ (cf. sec. 2.2.1). In agreement with [22] (resolution: 512^3), the beginning of the dissipative range is estimated to $k_{diss} \approx 25$, where the spectra start the bend down.	50
38	Powerspectra of the mass-weighted velocity field for the turbulent phase $t_d = [2, 4]$ (time-average) and at the end of the decaying phase $t_d = 6.0$. The black solid line marks the expected slope $m_{vw} = -5/3$ (cf. sec. 2.2.1). In agreement with [22] (resolution: 512^3), the beginning of the dissipative range is estimated to $k_{diss} \approx 25$, where the spectra start the bend down.	50
39	Time evolution of the inertial range's slope of the volume-weighted velocity powerspectra. See fig. 37.	51
40	Time evolution of the root-mean-square mach number.	53
41	Decaying Turbulence from Mach 10: Column Sonic Mach Number and column density along z-axis at $t_d = 1.0$ when the root-mean-square mach number has fallen to $\mathcal{M} = 4.2$	55
42	Decaying Turbulence from Mach 10: Column Sonic Mach Number and column density along z-axis at $t_d = 1.0$ when the root-mean-square mach number has fallen to $\mathcal{M} = 4.2$	56
43	Decaying Turbulence from Mach 10: Column Sonic Mach Number and column density along z-axis at $t_d = 1.0$ when the root-mean-square mach number has fallen to $\mathcal{M} = 4.2$	57
44	Decaying Turbulence from Mach 10: Column Sonic Mach Number and column density along z-axis at $t_d = 2.0$ when the root-mean-square mach number has fallen to $\mathcal{M} = 2.4$	58
45	Decaying Turbulence from Mach 10: Column Sonic Mach Number and column density along z-axis at $t_d = 2.0$ when the root-mean-square mach number has fallen to $\mathcal{M} = 2.4$	59
46	Decaying Turbulence from Mach 10: Column Sonic Mach Number and column density along z-axis at $t_d = 2.0$ when the root-mean-square mach number has fallen to $\mathcal{M} = 2.4$	60
47	Decaying Turbulence from Mach 10: Column Sonic Mach Number and column density along z-axis at $t_d = 3.0$ when the root-mean-square mach number has fallen to $\mathcal{M} = 1.9$	61
48	Decaying Turbulence from Mach 10: Column Sonic Mach Number and column density along z-axis at $t_d = 3.0$ when the root-mean-square mach number has fallen to $\mathcal{M} = 1.9$	62
49	Decaying Turbulence from Mach 10: Column Sonic Mach Number and column density along z-axis at $t_d = 3.0$ when the root-mean-square mach number has fallen to $\mathcal{M} = 1.9$	63
50	Time evolution of the fraction of vinite volume elements to the total number of elements. <i>Remark</i> The other solvers would stay at 100% since they operate solely with finite volumes.	64
51	Time evolution of the energy. The logarithmic scaling helps to visually distinguish to course of total and kinetic energy. The total energy E is the sum of the kinetic \mathcal{K} and internal energy \mathcal{I} : $\log_{10}(E) = \log_{10}(\mathcal{I} + \mathcal{K})$	65

52	Time evolution of the kinetic energy dissipation in logarithmic scale $\log_{10}(-\frac{dK}{dt_d})$. The averaged area (numerical integration) under the plots amounts to $\int dt_d - \frac{dK}{dt_d} = 48.251 \pm 0.007$ which is almost all of the initial kinetic energy: $K_0 = 48.75 \pm 0.03$	65
53	Log-log scale volume-weighted density PDFs. As the decay progresses, the widths of the distributions decrease and the mean values return to the initial density: $\log_{10}(\rho_0) = \log_{10}(1) = 0$. The solid black curve depicts the density distribution of the smoothed initial state (cf. fig. 14). The applied Gaussian blur truncated the high density range. The log-normal fit (dotted lines) were done with eqn. 58.	66
54	Time evolution of the sonic mach number over time derived from the width of the volume-weighted density PDFs of the decaying turbulence. The dashed line represents the root-mean-square velocity of the PPM solver and serves as a reference. Due to the lognormal relationship, the fit yields very low error margins. Hence, the error bars are too small to see. The spike on the left is caused by the originally smoothed initial state. The turbulence has to redevelop in order to yield sensible results. However, the Mach number estimation via relation eqn. 58 ($b = 2/3$) is systematically below the reference. This agrees with the results in the decay phase of the driven turbulence (cf. sec. 4.2.5).	67
55	Log-log. scale volume-weighted velocity PDFs moving from right to left with increasing time due to kinetic energy decline of the decaying turbulence. The median point of the initial PDF at $t_d = 0$ is precisely over Mach 10: $\mu_0 = \log_{10}(1) = 10$. A non-existent dispersion of the PDFs over time indicates no bulk motion which is a good sign (cf. sec. 4.2.5).	67
56	Powerspectra of the volume-weighted mean kinetic energy field shown for three stages of decay: $t_d = 0$, $t_d = 3.0$ and $t_d = 6.0$. Since the total kinetic energy declines over time the powerspectra shift downwards. The strange looking spectrum from $t_d = 0$ is the result of the applied Gaussian blur on the initial state. In agreement with [22] (resolution: 512^3), the beginning of the dissipative range is estimated to $k_{diss} \approx 25$, where the spectra start the bend down.	68
57	Powerspectra of the volume-weighted velocity field for three stages of decay: $t_d = 0$, $t_d = 3.0$ and $t_d = 6.0$. Since the total kinetic energy declines over time, the powerspectra shift downwards. The strange looking spectrum from $t_d = 0$ is the result of the applied Gaussian blur on the initial state. In agreement with [22] (resolution: 512^3), the beginning of the dissipative range is estimated to $k_{diss} \approx 25$, where the spectra start the bend down.	69
58	Powerspectra of the mass-weighted velocity field for three stages of decay: $t_d = 0$, $t_d = 3.0$ and $t_d = 6.0$. Since the total kinetic energy declines over time, the powerspectra shift downwards. The strange looking spectrum from $t_d = 0$ is the result of the applied Gaussian blur on the initial state. In agreement with [22] (resolution: 512^3), the beginning of the dissipative range is estimated to $k_{diss} \approx 25$, where the spectra start the bend down.	69

List of Tables

1	Sod-Shock: Initial Condition	30
2	Overview of conducted runs for the Sod Shock Tube Problem	30
3	Outline of initial condition for all driven turbulence simulations	34
4	Outline of Driven Turbulence Simulations	34

5	Comparison of Gaussian Fitting Results of the Log-normal Density PDF averaged over the turbulent phase: $t_d = [2, 4]$. See relation eqn. 58. $b = 2/3$. The PDF Mach number \mathcal{M}_{PDF} of the Midpoint FV overshoots due to the influence of the runaway. Compare fig. 32.	46
6	Comparison of the three types of powerspectra averaged over the turbulent phase: $t_d = [2, 4]$	51
7	Outline of the Decaying Turbulence Setup. Note the small CFL number for PPM, which turned out to be necessary in order not to crash. There is a slight variance among the initial Mach numbers/kinetic energies. They stem from the fact that these values were measured at simulation runtime, when subjected to minor numerical errors.	53

List of Symbols and Acronyms

Symbol	Meaning
\mathcal{M}	sonic Mach number
u_{rms}	root-mean-square velocity
ε	kinetic energy dissipation rate
\mathcal{P}	momentum
E	total energy
\mathcal{K}	kinetic energy
\mathcal{I}	internal energy
m	mass
ρ	density
p	pressure
u	velocity
V	volume
L	characteristic length
μ_{visc}	dynamic viscosity
$\mu_{n-\text{visc}}$	numerical viscosity
ϵ	artificial viscosity
Re	Reynolds number
γ	adiabatic constant
c	speed of sound
R	gas constant
c_v, c_p	specific heat capacity at constant volume and pressure
T	temperature
C_p	polytropic constant
Γ	polytropic exponent
\mathbb{T}	strain-energy tensor
\mathcal{P}	bulk motion
\mathbf{B}	magnetic flux density
Δ_{RMS}	root-mean-square error norm
$\Delta_{\text{RMS,rel.}}$	relative root-mean-square error norm
T_d	turn/turning time, crossing time, dynamic time scale
t_d	dynamic time
k	spatial wave number, mode in Fourier space
ζ	ratio of compressive to solenoidal driving
η, τ, v	Kolmogorov microscales: length, time and velocity
$\mathbf{i} = (i, j, k)$	multi-index
N_p	polynomial order
$l_i(x)$	one-dimensional Lagrange polynome
$L_{\mathbf{i}}(\mathbf{x})$	three-dimensional Lagrange polynome
ϕ	smooth test function
ψ	Lagrange/Legendre basis function
ω_k	integration weights
∇	nabla operator
Ω	integration domain

Acronym	Meaning
MHD	magneto-hydrodynamics
ISM	interstellar medium
CPU	central processing unit
CFL	Courant–Friedrichs–Lewy condition
CFD	computational fluid dynamics
RMS	root-mean-square
RMSV	root-mean-square velocity
FV	Finite Volume
DG	Discontinuous Galerkin
FLASH	FV based fluid dynamics framework
FLEXI	DG based fluid dynamics framework
PPM	Piece-wise Parabolic Method
B3	Bouchut 3
B5	Bouchut 5
EU	(explicit) Euler
MP	(explicit) Midpoint
RK3	Third-order Runge-Kutta
EU-FV	Euler Finite Volume
EU-HY	Euler Hybrid
MP-FV	Midpoint Finite Volume
MP-HY	Midpoint Hybrid
RK3-FV	Third-order Runge-Kutta Finite Volume
RK3-HY	Third-order Runge-Kutta Hybrid
FCG	face-centered grid
BCG	body-centered grid
GNG	Gauss nodal grid
LNG	Gauss-Lobatto nodal gridd

Contents

1	Introduction	1
2	Theory	2
2.1	Governing equations	2
2.1.1	Compressible Euler Equations	2
2.1.2	Weak Formulation	4
2.2	Turbulence Statistics	5
2.2.1	Energy Cascade & Powerspectrum	7
2.2.2	Probability Distribution Functions	10
2.3	Supersonic Shocks	11
2.4	Finite Element Schemes	13
2.4.1	Discontinuous Galerkin Method	13
2.4.2	Time Integration	16
2.4.3	Flux Functions	18
3	Numerical Prerequisites	19
3.1	Computational Frameworks	19
3.2	Turbulent Forcing	20
3.3	Shock Capturing	22
3.4	Interpolation & Data Transfer	26
4	Results & Discussion	30
4.1	SOD Shock Tube Problem	30
4.1.1	Adiabatic & Isothermal Shock	30
4.1.2	Adiabatic & Isothermal Sod with Strong Shock	31
4.1.3	Summary	33
4.2	Driven Turbulence	33
4.2.1	Mach Number Evolution	34
4.2.2	Column Density & Velocity	35
4.2.3	FV-DG Mode Switching	41
4.2.4	Energy Dissipation	43
4.2.5	Density & Velocity Distributions	45
4.2.6	Energy & Velocity Powerspectra	48
4.2.7	Summary	52
4.3	Decaying Turbulence	53
4.3.1	Mach Number Evolution	53
4.3.2	Column Density & Velocity	54
4.3.3	FV-DG Mode Switching	64
4.3.4	Energy Dissipation	64
4.3.5	Density & Velocity Distributions	66
4.3.6	Energy & Velocity Powerspectra	68
4.3.7	Summary	70
5	Conclusion & Outlook	71

1 Introduction

Astrophysical turbulence simulations of interstellar gases play a vital role in the understanding and modelling of star formation (cf. [31]). A multitude of numerical schemes and computational fluid dynamics software has been developed, each with their own merits and drawbacks.

Finding the best numerical solver for a specific problem domain is a vibrant field of research as of today, even though the first pioneers began to conduct simple physics simulations many decades ago. A lot has changed since these days. The present explosion in computing power, paralleled by a striking inflation of operational costs, passes on a mighty tool to the astrophysics community, which opens the door to numerical experiments unfeasible ten years ago.

Alongside the advent of new technical possibilities, modern numerical schemes appear which are better suited for utilizing latest CPU architectures to gain better performance. Especially, the aeronautics and car industries push forward the development of new simulation software. They are interested in modelling flight characteristics for new airplane designs, the aerodynamic drag of cars or want to increase the efficiency of combustion engines. Consequently, innovative numerical schemes have to be highly flexible with regards to meshing complex geometries, high accuracy, massively scalability and blazing performance. The demands for the underlying physical model are rather moderate. The Navier-Stokes equations suffice on most occasions. One of the latest specimen of their kind is the high-order accurate CFD software FLEXI¹ developed by teams at the MATHEMATICAL INSTITUTE (Univ. of Cologne) and the INSTITUTE OF AERODYNAMICS AND GAS DYNAMICS (Univ. of Stuttgart). Special credit goes to Prof. Dr.-Ing. Gregor Gassner, who is the initiator of the project, and his former supervisor Prof. Dr. Claus-Dieter Munz. Their idea is to introduce piecewise polynomial functions of higher order. The underpinning scheme is called *discontinuous Galerkin method*. The implementation details of FLEXI are discussed in [17, 18, 15].

In contrast to air flow models, the demands for turbulence simulations of astrophysical gases are quite the opposite. Free space does not imply complex geometries. But the physical model becomes very complex, when electro-magnetic fields, radiation, chemistry and gravity are introduced to the governing equations. Furthermore, a huge range of scales in time, space, energy, density and pressure must be covered as well. As if this is not enough, high Mach numbers in the flow give rise to strong shock conditions or discontinuities, which challenge the stability and accuracy of every numerical solver. Up to now, the astrophysics community considers finite volume schemes of first/second order to be the only viable option for conducting this kind of simulation. FLASH², originally developed by researchers at the University of Chicago, is the name for a well established nuclear and astrophysics simulation software with *finite volumes* as their foundational scheme. FLASH is, for example, discussed in [14, 29, 48].

This thesis is a first attempt to introduce higher order Galerkin methods to astrophysical turbulence simulations. The statistical evaluation of simple turbulence setups, run by FLASH and FLEXI, are expected to give an insight into the potential, Galerkin schemes might offer to the astrophysics community.

¹<https://www.flexi-project.org>

²<http://flash.uchicago.edu/site/flashcode/>

2 Theory

2.1 Governing equations

In astrophysics, the *interstellar medium* (ISM) is the matter that exists in the space between the star systems in a galaxy. It contains gas in ionic, atomic, and molecular form, as well as dust and cosmic rays. ISM fills interstellar space and blends smoothly into the surrounding intergalactic space. The medium is composed primarily of atomic hydrogen followed by helium with traces of carbon, oxygen, nitrogen and metals. Magnetic fields and turbulent motions also provide pressure in the ISM, and are typically more important dynamically than the thermal pressure.

Many theoretical models for ISM are based on the ideal *Magneto-Hydrodynamic equations* which are a blend of the *compressible Euler equations* and the *Maxwell equations*, describing the hydrodynamics and (electro-)magnetodynamics, respectively.

In this thesis we solely focus on the hydrodynamics.

2.1.1 Compressible Euler Equations

In 1757 LEONHARD EULER (1707-1783) published a set of equations for inviscid flow, known as the Euler equations. They are hyperbolic conservation equations which model perfect fluids without any interaction of their constituents. Hence, we assume no heat conduction ($\mathbb{T}^{i0} = \mathbb{T}^{0i} := 0$, $i \in \{1, 2, 3\}$), no viscosity ($\mathbb{T}^{ij} := p \mathbb{I}$, $i, j \in \{1, 2, 3\}$) and no gravity $g = 0$. Within the comoving frame the *stress-energy tensor* $\mathbb{T} \in \mathbb{R}^{4x4}$ then reads:

$$\mathbb{T}^{\alpha\beta} = \text{diag}(\rho c^2, p, p, p) = \left(\rho + \frac{p}{c^2} \right) u^\alpha u^\beta + p \mathbb{G}^{\alpha\beta} \quad \text{with } \alpha, \beta \in \{0, 1, 2, 3\}, \quad (1)$$

where ρ , p , u , c and \mathbb{G} are the density, pressure, velocity, speed of sound and the *metric tensor*. In flat spacetime the metric tensor is set to $\mathbb{G} = \text{diag}(-1, 1, 1, 1)$. The total energy E and the number of particles n are conserved.

$$\partial_\beta \mathbb{T}^{\alpha\beta} = 0 \quad (2)$$

$$\partial_\alpha (n u^\beta) = 0 \quad (3)$$

Taking the non-relativistic limit, we arrive at the conservative differential form of the Euler equations.

$$\partial_t \rho + \nabla \cdot (\rho \mathbf{u}) = 0 \quad \text{mass conservation} \quad (4)$$

$$\partial_t (\rho \mathbf{u}) + \nabla \cdot (\rho \mathbf{u} \mathbf{u}^T) + \nabla p = \mathbf{F} \quad \text{momentum conservation} \quad (5)$$

$$\partial_t E + \nabla \cdot (\mathbf{u} (E + p)) = 0, \quad \text{energy conservation} \quad (6)$$

where ∂_t is the partial derivative in time, $\nabla = (\partial_x, \partial_y, \partial_z)^T$ is the *Nabla-operator* and $\mathbf{u} = (u^x, u^y, u^z)^T$ is the velocity vector. The total energy E is the sum of the internal energy \mathcal{I} and the kinetic energy \mathcal{K} .

$$E = \mathcal{I} + \mathcal{K} = \frac{p}{\gamma - 1} + \frac{\rho}{2} u^2, \quad (7)$$

with γ being the *adiabatic constant*. The source term \mathbf{F} (F for forcing) allows us to perpetually inject a force field which gets important in the discussion of driven turbulence later on. See sec. 3.2.

Equation of State All simulations follow the *ideal gas law*.

$$p = \frac{c^2}{\gamma} \rho = R T \rho = \frac{R}{c_v} \mathcal{I} = (\gamma - 1) \mathcal{I}, \quad (8)$$

where R is the specific ideal gas constant, T is the gas temperature and $c_v = \frac{\gamma-1}{R}$ is the specific heat capacity at constant volume. The γ is set to

$$\gamma = \frac{c_p}{c_v} := \frac{5}{3}, \quad (9)$$

which represents a mono-atomic gas without interacting forces. c_p is the specific heat capacity at constant pressure. During the numerical simulation the equation of state is enforced via the *polytropic process* (also called *polytropic cooling*) at every timestep.

$$p = C_P \rho^\Gamma \quad (C_P = \text{const}), \quad (10)$$

where the *polytropic exponent* is set to $\Gamma := 1$ which is equivalent to an isothermal process. A thorough derivation can be found in [20, p. 2 ff.]. The speed of sound c is constant due to the polytropic relation. Comparing eqn. 8 with eqn. 10 we get the squared *isothermal* speed of sound.

$$C_P = c^2 = \gamma \frac{p}{\rho} = \text{const}. \quad (11)$$

Dimensionless Euler Equations We want to show that the Euler equations are invariant to changes of units. This discussion is useful since most numerical frameworks do not support physical units and rescaled physical quantities avoid truncation errors due to the limits of floating point operations. For this, we choose a characteristic length l_r , a characteristic velocity u_r and a characteristic density ρ_r . Multiplying suitable combinations of these constants with the Euler equations yields

$$[\partial_t \rho + \nabla \cdot (\rho \mathbf{u})] \cdot \frac{l_r}{\rho_r u_r} = 0 \quad (12)$$

$$[\partial_t (\rho \mathbf{u}) + \nabla \cdot (\rho \mathbf{u} \mathbf{u}^T) + \nabla p - \mathbf{F}] \cdot \frac{l_r}{\rho_r u_r^2} = 0 \quad (13)$$

$$[\partial_t E + \nabla \cdot (\mathbf{u} (E + p))] \cdot \frac{l_r}{\rho_r u_r^3} = 0 \quad (14)$$

We simplify and get

$$\partial_{\tilde{t}} \tilde{\rho} + \tilde{\nabla} \cdot (\tilde{\rho} \tilde{\mathbf{u}}) = 0 \quad (15)$$

$$\partial_{\tilde{t}} (\tilde{\rho} \tilde{\mathbf{u}}) + \tilde{\nabla} \cdot (\tilde{\rho} \tilde{\mathbf{u}} \tilde{\mathbf{u}}^T) + \tilde{\nabla} \tilde{p} - \tilde{\mathbf{F}} = 0 \quad (16)$$

$$\partial_{\tilde{t}} \tilde{E} + \tilde{\nabla} \cdot (\tilde{\mathbf{u}} (\tilde{E} + \tilde{p})) = 0, \quad (17)$$

where $t_r = \frac{l_r}{u_r}$ (characteristic time) and

$$\tilde{t} = \frac{t}{t_r}, \quad \tilde{\rho} = \frac{\rho}{\rho_r}, \quad \tilde{\mathbf{u}} = \frac{\mathbf{u}}{u_r}, \quad \tilde{\nabla} = l_r \nabla, \quad \tilde{E} = \frac{E}{\rho_r u_r^2}, \quad \tilde{p} = \frac{p}{\rho_r u_r^2}, \quad \tilde{\mathbf{F}} = \mathbf{F} \frac{l_r}{\rho_r u_r^2}. \quad (18)$$

Consequently, the dimensionless Euler equations do not change under unit transformation. If not stated otherwise, we drop the tilde sign ($\tilde{\cdot}$) and assume always dimensionless quantities from now on.

Choice of parameters One consequence of dimensionless units is the free choice of parameters. We exploit this feature in order to choose a sensible set of parameters. Considering the Euler equations in conservative form (eqn. 4), their functions in space and time

$$\rho = \rho(t, x, y, z), \quad (\rho \mathbf{u}) = (\rho \mathbf{u})(t, x, y, z), \quad E = E(t, x, y, z) \quad (19)$$

are completed with

$$R := 1, \langle \rho \rangle := 1, \langle c \rangle = c := 1, \quad (20)$$

From that we derive

$$\langle p \rangle = \frac{c^2}{\gamma} \cdot \langle \rho \rangle = 0.6, \quad \langle \mathcal{I} \rangle = \frac{\langle p \rangle}{\gamma - 1} = 0.9, \quad \langle T \rangle = \frac{\langle c \rangle^2}{\gamma R} = 0.6, \quad (21)$$

where $\langle \cdot \rangle$ is the *volume-weighted average* or *mean value* over the domain Ω .

$$\langle q \rangle = \frac{\int_{\Omega} q d\Omega}{\int_{\Omega} d\Omega} \quad (22)$$

This set of parameters define the global state at all times.

2.1.2 Weak Formulation

A natural way to define a generalized solution of the Euler equations that does not require differentiability is going back to the integral form of the conservation law.

The basic idea is to take the PDE, multiply it by a smooth *test function*, integrate one or more times over some domain, and then use integration-by-parts to move derivatives off the function q and onto some smooth test function ϕ . The result is an equation involving fewer derivatives on q , and hence requiring less smoothness.

In this section we want to derive the *weak formulation* of the governing equations. This establishes the basis for the polynomial formulation which is the core idea of all DG methods. First, the Euler equations get split up into terms resembling the independent one temporal and three spatial dimensions with respect to the linear differential operator.

$$\partial_t \mathbf{U} + \partial_x \mathbf{F}(\mathbf{U}) + \partial_y \mathbf{G}(\mathbf{U}) + \partial_z \mathbf{H}(\mathbf{U}) = \mathbf{S}, \quad (23)$$

where

$$\mathbf{U} = (\rho, \rho u_1, \rho u_2, \rho u_3, E)^T \quad (24)$$

$$\mathbf{F}(\mathbf{U}) = (\rho u_1, \rho u_1^2 + p, \rho u_1 u_2, \rho u_1 u_3, u_1(E + p))^T \quad (25)$$

$$\mathbf{G}(\mathbf{U}) = (\rho u_2, \rho u_2 u_1, \rho u_2^2 + p, \rho u_2 u_3, u_2(E + p))^T \quad (26)$$

$$\mathbf{H}(\mathbf{U}) = (\rho u_3, \rho u_3 u_1, \rho u_3 u_2, \rho u_3^2 + p, u_3(E + p))^T \quad (27)$$

$$\mathbf{S} = (0, f_1, f_2, f_z, 0)^T \quad (28)$$

Defining a vector-valued test function $\phi = (0, \dots, 0, \phi_i, 0, \dots, 0)^T$ ($i \in 1, \dots, 5$), multiplying component-wise with above equation and integrating over the domain Ω , we get

$$\int_{\Omega} \left(\partial_t U_i \phi^i + \partial_x F_i(\mathbf{U}) \phi^i + \partial_y G_i(\mathbf{U}) \phi^i + \partial_z H_i(\mathbf{U}) \phi^i + S_i \phi^i \right) d^3x = 0. \quad (29)$$

Integration-by-parts rearranges the integral into a *source term*, *surface term* and *volume term*.

$$\int_{\Omega} \partial_t U_i \phi^i d^3x = \int_{\Omega} S_i \phi^i d^3x \quad (30)$$

$$+ \int_{\partial\Omega} \left(F_i(\mathbf{U}) \phi^i n_x + G_i(\mathbf{U}) \phi^i n_z + H_i(\mathbf{U}) \phi^i n_z \right) d^2x, \\ - \int_{\Omega} \left(F_i(\mathbf{U}) \partial_x \phi^i + G_i(\mathbf{U}) \partial_y \phi^i + H_i(\mathbf{U}) \partial_z \phi^i \right) d^3x \quad (31)$$

where $\mathbf{n} = (n_x, n_y, n_z)^T$ is the outward surface normal to $\partial\Omega$.

Unfortunately, weak solutions are not unique, and so an additional problem is to identify which weak solution is the physically correct *vanishing-viscosity* solution. Again, one would like to avoid working with the viscous equation directly, but it turns out that there are other conditions one can impose on weak solutions that are easier to check and will also pick out the correct solution. These are called *entropy conditions* by analogy with the gas dynamics case, where a discontinuity is physically realistic only if the entropy of the gas increases as it crosses the shock. So called *entropy-stable* numerical solver take this into account (cf. [10]).

2.2 Turbulence Statistics

Turbulences are common phenomena in nature. It names a flow regime in fluid dynamics characterized by chaotic changes in pressure and flow velocity and contrasts *laminar* flow which occurs when a fluid flows in parallel layers with no disruption between them.

In astrophysics turbulence is suspected to play a major role in star formation within interstellar media (cf. [23]). Hence, a theoretical understanding of the underlying mechanics is crucial in order to correctly model turbulences in numerical simulations. While the problem for incompressible media has been thoroughly studied in the past (*Kolmogorov scaling*: cf. sec. 2.2.1), the additional dynamics introduced by compressibility are still an active field of research.

It is important not to forget that real ISM turbulence is neither isothermal, nor polytropic. The real ISM has a local temperature that is not a simple function of density but results from the evolution of the thermal energy due to ongoing heating and cooling processes. Gravity takes over control of the most dense regions. Magnetic fields lead to effects like frozen filaments called *Alfvén's frozen in theorem* (cf. [37]).

Reynolds Number An important dimensionless quantity in fluid mechanics used to help predict flow patterns in different fluid flow situations is the *Reynolds number* Re . The Irish-British physicist OSBORNE REYNOLDS (1842-1912) discovered this fundamental relationship during his famous flow tube experiments in the second half of the 19th century. It represents the ratio between *inertial* and *viscous* forces and is calculated by

$$Re = \frac{\text{inertial force}}{\text{viscous force}} = \frac{\rho u L}{\mu_{vis}}, \quad (32)$$

where ρ , u , L , μ_{vis} are the fluid density, fluid velocity, characteristic length and dynamic viscosity, respectively. Since the governing equations are defined to be the inviscid Euler equations (cf. sec. 2.1), in theory, there is no viscosity anywhere present.

$$\mu_{vis} \equiv 0 \implies Re = \infty \quad (33)$$

This has far-reaching consequences because the Reynolds number predicts the transition from *laminar* to *turbulent* flow. Laminar flow becomes unstable when the inertial forces dominate over the viscous forces: $Re \gg 1$. Consequently, the Euler equations lead to chaotic motion over all time and length scales for large Re .

Reynolds Decomposition Turbulences are characterized by a random fluctuation q' of a flow variable q (density, pressure, velocity, temperature, etc.) over time, measured at a fixed point in space. Their evolution can be described with the *Reynolds decomposition*.

$$q(t) = \langle q \rangle_t + q'(t), \quad \langle q' \rangle \equiv 0 \quad (34)$$

where

$$\langle q \rangle_t = \frac{\int_{t_0}^{t_1} q(t) dt}{t_1 - t_0} \quad (35)$$

is the time-average of the flow property $q(t)$. Turbulent flows are globally described in terms of their mean values of properties like density, velocity and pressure. The velocity fluctuations are independent of the axis of reference, i.e. invariant to translation, rotation and reflection; they are *isotropic*. *Isotropic turbulence* is by its definition always homogeneous. In such a situation, the gradient of the mean velocity does not exist, the mean velocity is either zero or constant throughout.

As the Reynolds decomposition suggests it does not make sense to talk about a turbulence at one specific point in time or space. Thus, we define important average properties or *mean values* who help to quantify the current state of the turbulent system as a whole.

Root-mean-square Velocity is defined as the mass-weighted average squared velocity of the system.

$$u_{\text{rms}} = \sqrt{\frac{\int_{\Omega} \rho \mathbf{u}^2 d\Omega}{\int_{\Omega} \rho d\Omega}} \quad (36)$$

We utilize mass-weighting since the conducted turbulence simulations are highly compressible.

Sonic Mach Number is directly related to u_{rms} via

$$\mathcal{M} = \frac{u_{\text{rms}}}{\langle c \rangle}. \quad (37)$$

From $\langle c \rangle = 1$, according to eqn. 20, follows that Mach number and root-mean-square (RMS) velocity are equivalent and, if not stated otherwise, used interchangeably.

Remark We break the convention since usually the Mach number is measured with the volume-weighted RMS velocity.

Turning time represents a time span characterizing large scale turbulent motions. Under sec. 2.1 a characteristic time scale $t_r = \frac{L}{u_{\text{rms}}}$ was introduced exhibiting the invariance of the Euler equations under unit transformations. Now it gets a practical meaning since we define a *turning time* that tells how long it takes for a turbulence vortex to traverse the length L of the physical domain.

$$T_{\text{turn}} = \frac{L}{u_{\text{rms}}} \quad (38)$$

Equivalent terms for the turning time are *crossing time* or *dynamic time scale*.

Dynamic time is the scaled *physical* time t .

$$t_d = \frac{t}{T_{turn}} \quad (39)$$

All time evolution plots presented in this thesis are scaled to dynamic time which sets the time axis in relation to the analyzed turbulence.

Remark The dynamic time here is not to be confused with the *free-fall time* in gravity-driven simulations.

Bulk Motion is the integrated momentum over the whole domain.

$$\mathcal{P} = \int_{\Omega} \rho \mathbf{u} d\Omega \quad (40)$$

For turbulences in closed systems, say a periodic box (three-dimensional torus), bulk motion distorts the measurement of mean values like the sonic Mach number. In the worst case scenario the whole fluid would coherently move in one direction pretending to be a turbulent flow of a certain Mach number. Correction of bulk motion is a crucial subject in turbulence simulations.

Total Kinetic Energy is important in the discussion of energy accounting, especially in closed systems where the total energy $E = \mathcal{I} + \mathcal{K} = \text{const}$ is conserved.

$$\mathcal{K} = \int_{\Omega} \frac{\rho}{2} \mathbf{u}^2 d\Omega \quad (41)$$

Total Kinetic Energy Dissipation Rate is the negated time derivative of the total kinetic energy.

$$\varepsilon = -\frac{d\mathcal{K}}{dt} \quad (42)$$

It quantifies how fast kinetic energy gets transformed into internal energy at a certain point in time.

$$\frac{dE}{dt} = \frac{d\mathcal{I}}{dt} + \frac{d\mathcal{K}}{dt} = 0 \iff \frac{d\mathcal{I}}{dt} = -\frac{d\mathcal{K}}{dt} \quad (43)$$

2.2.1 Energy Cascade & Powerspectrum

Real turbulences always have a three-dimensional character and they lead to rotational flow structures, called turbulent eddies, with a wide range of length and energy scales.

Fluid particles which were initially separated by a large distance can be brought close together by eddying motions. Consequently, mass, heat and momentum are very effectively exchanged. It is an established fact that this property has a profound influence in birth of stars, solar systems and cosmic structures.

ANDREY KOLMOGOROV (1903-1987) was a pioneering mathematician who provided a statistical treatment of turbulent flows, the *Kolmogorov picture*, with methods from *dimensional analysis* (cf. [50, p. 33ff], [5, p. 26ff]). The spatial wavenumber k for an eddy of diameter λ is defined as

$$k = \frac{2\pi}{\lambda}. \quad (44)$$

For the sake of clarity, k is scaled to $\tilde{k} = k/2\pi$. We drop the tilde and refer to the scaled wave number $k := \tilde{k}$ from now on.

Based on k the eddies in a turbulent flow are arranged into a hierarchy or more precisely, a *spectrum*. The largest eddies interact and transfer energy from the mean flow. We call it the range of *large scales*. Since large eddies are of the same order of the characteristic length L and velocity scale u_{rms} , the flow is inviscid and their dynamics are dominated by inertial effects. At the *inertial range* kinetic energy gets transferred down to smaller eddies via *vortex stretching*. An *energy cascade* from larger to smaller length scales takes shape. The so called *Kolmogorov microscales* (cf. [24]), denoting the smallest scales in the spectrum, form the *viscous* or *dissipative sublayer range* where the energy input from nonlinear interactions and the energy drain from viscous dissipation are in exact balance. The Reynolds number is 1 (eqn. 32) and the laminar flow dominates.

$$\eta = \left(\frac{\mu_{\text{visc}}^3}{\rho^3 \varepsilon} \right)^{1/4} \quad \text{Kolmogorov length scale} \quad (45)$$

$$\tau = \left(\frac{\mu_{\text{visc}}}{\rho \varepsilon} \right)^{1/2} \quad \text{Kolmogorov time scale} \quad (46)$$

$$v = \left(\frac{\mu_{\text{visc}} \varepsilon}{\rho} \right)^{1/4} \quad \text{Kolmogorov velocity scale} \quad (47)$$

where ρ is the ambient density and ε is the kinetic energy dissipation rate defined in eqn. 42. Fig. 1 gives an illustration of the energy spectrum of a turbulent flow as just described.

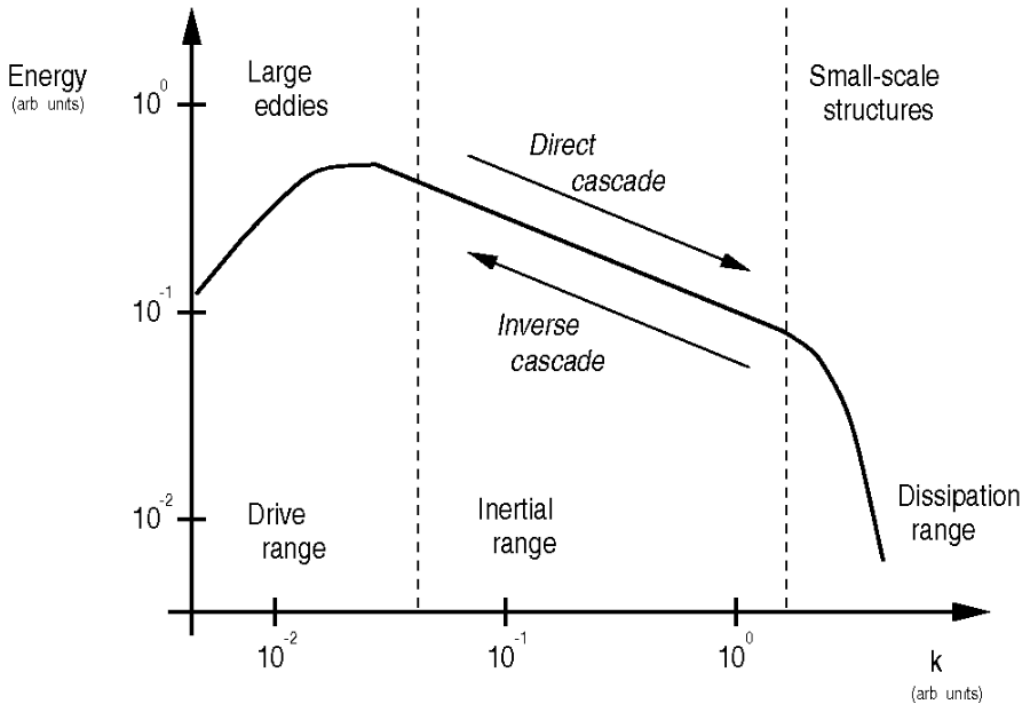


Figure 1: Source: [33, p. 8]. Schematic of the Kolmogorov picture of turbulence showing the spatial energy powerspectrum over k . The mathematical definition is given by eqn. 50. The physical meaning of the marked ranges are detailed in the text.

Numerical Viscosity By the very definition of the Euler equations there is no viscosity: $\mu_{\text{visc}} \equiv 0$. This would mean turbulent flow all the way down. The dissipation range is non-existent. It is rather evident that no physical simulation, running on a machine with computing power and memory limits, is able to model this flow. The profound consequence is that ISM simulations are, no matter what, always under-resolved.

Every numerical scheme introduces a so called *numerical* viscosity $\mu_{\text{n-visc}}$ that marks the very limit of length, time and velocity scale this scheme is still capable to resolve. The exact amount of $\mu_{\text{n-visc}}$ is in general unknown but should be unique for every numerical method. For grid based schemes it is possible to estimate a lower limit of the length scale η . The *Nyquist–Shannon sampling theorem* (cf. [40]) states that:

If a function $x(t)$ contains no frequencies higher than B Hertz, it is completely determined by giving its ordinates at a series of points spaced $1/(2B)$ seconds apart.

Applying this theorem to a uniform grid with N nodes, the smallest length scale would then become $\eta = 2/N$. With eqn. 45 we arrive at a relation between kinetic energy dissipation and numerical viscosity.

$$\mu_{\text{n-visc}} = (\eta^4 \varepsilon)^{1/3} = 2^{4/3} \left(\frac{\varepsilon}{N^4} \right)^{1/3} \propto \varepsilon^{1/3} \quad (48)$$

When the grid resolution N is equal among different numerical schemes, their capability of resolving smallest scales can be compared by looking at the kinetic energy dissipation rate.

Remark The term *dissipation* might mistakenly suggest a physical process causing the loss in kinetic energy. This is not the case! It is the sum of scattering effects that the coarseness of grids imposes on small scale structures. One might call it *numerical* dissipation.

Kinetic Energy Powerspectrum Fig. 1 shows the schematic of the shell-averaged kinetic energy spectrum $\overline{P_K}$ of a fully developed turbulence. The powerspectrum P_K is defined as

$$P_K = \hat{\mathcal{K}}(\mathbf{k}) \cdot \hat{\mathcal{K}}^\dagger(\mathbf{k}), \quad (49)$$

where $\mathbf{k} = (k_1, k_2, k_3)^T$ is the spatial wave vector analog to eqn. 44, $\hat{\mathcal{K}}(\mathbf{k})$ is the Fourier transformed kinetic energy field $\mathcal{K}(\mathbf{x})$ and $\hat{\mathcal{K}}^\dagger(\mathbf{k})$ its complex conjugate. Taking the shell-average over P_K yields

$$\overline{P_K} dk = 4\pi k^2 \hat{\mathcal{K}}(\mathbf{k}) \cdot \hat{\mathcal{K}}^\dagger(\mathbf{k}) dk = 4\pi k^2 \hat{\mathcal{K}} \cdot \hat{\mathcal{K}}^\dagger dk. \quad (50)$$

The pre-factor $4\pi k^2$ is a contribution from the differential volume of a thin sphere at radius $k = |\mathbf{k}| \geq 0$. The area under $\overline{P_K}$

$$A_{K^2} = \frac{1}{V_\Omega} \int_0^\infty 4\pi k^2 \hat{\mathcal{K}} \cdot \hat{\mathcal{K}}^\dagger dk \quad (51)$$

is equal to the total squared kinetic energy \mathcal{K}^2 of the system in accordance with PARSEVAL's theorem

$$\int_{-\infty}^\infty |Y(x)|^2 dx = \int_{-\infty}^\infty |\hat{Y}(k)|^2 dk. \quad (52)$$

Velocity Powerspectrum It has been shown that the descent of the energy cascade among turbulences is universal. See [12, 41, 6, 22]. By determining the slope of log-log scale velocity powerspectra one can determine if the turbulence is modeled correctly.

For each velocity component we take the Fourier transform of the velocity field $\mathbf{u} = (u_1, u_2, u_3)^T$. We denote these Fourier transforms as $\hat{\mathbf{u}} = (\hat{u}_1, \hat{u}_2, \hat{u}_3)^T$. Analog to above we define the powerspectrum as

$$P_u = \frac{1}{2} \hat{\mathbf{u}} \cdot \hat{\mathbf{u}}^\dagger. \quad (53)$$

Taking the shell-average we get

$$\overline{P_u} dk = 4\pi k^2 \frac{1}{2} \hat{\mathbf{u}} \cdot \hat{\mathbf{u}}^\dagger dk, \quad (54)$$

which we call the *volume-weighted* velocity powerspectrum. By mass-weighting the velocity beforehand, $\rho^{1/2} \mathbf{u}$, we get the *mass-weighted* velocity powerspectrum.

$$\overline{P_{mu}} dk = 4\pi k^2 \frac{1}{2} (\widehat{\rho^{1/2} \mathbf{u}}) \cdot (\widehat{\rho^{1/2} \mathbf{u}})^\dagger dk \quad (55)$$

The study in [22] lists slopes for the inertial range of the volume-weighted and mass-weighted powerspectra, as they are defined here. They amount to $m_{vw} = -19/9$ and $m_{mw} = -5/3$, respectively. We consider these values as reference which we are trying to reproduce in our turbulence simulations.

2.2.2 Probability Distribution Functions

Another tool to verify the properness of a turbulence simulation are density and velocity distributions. According to various studies [13, 19, 34, 25], a fully developed turbulence yields a nearly log-normal density distribution.

$$PDF_s(s) = \frac{1}{\sqrt{2\pi}\sigma_s} \exp\left[-\frac{(s-s_0)^2}{2\sigma_s^2}\right], \quad (56)$$

where $s = \ln(\rho/\rho_0)$. The standard deviation σ_s of the distribution is related to the sonic Mach number \mathcal{M} of the turbulence via (cf. [13, 25])

$$(2\sigma_s)^2 = \ln(1 + b^2 \mathcal{M}^2) \quad (57)$$

Reordering yields an explicit expression for the Mach number

$$\mathcal{M}_{PDF} = \frac{\sqrt{\exp((2\sigma_s)^2) - 1}}{b} \quad (58)$$

The proportionality constant b depends on the ratio of compressible to solenoidal forcing $\zeta \in [0, 1]$ and the number of spatial dimensions $D = 1, 2, 3$.

$$b = 1 + (D^{-1} - 1)\zeta \quad (59)$$

Numerical simulations (cf. [35]) show that $b \approx 0.5$ for a thermal mix of solenoidal and compressive modes (cf. sec. 3.2).

2.3 Supersonic Shocks

Astrophysical flows often involve shock waves. Shocks, or in more technical terms singular compression waves, are escalating highly localized spikes in density and pressure due to nonlinear dynamics inherent to the Euler equation. When a shock wave is emerging, the velocity behind the wave front is higher than in front of it. The medium is highly compressed until an unphysical state is reached. The velocity *characteristics* begin to cross. Nature solves this dilemma by introducing additional physics like extreme heat radiation, explosions, bangs or detachment of fluid. Either way, it involves an increase of entropy according to the second law of thermodynamics (cf. [38]). A numerical solver has to capture this kind of physics in order to prevent unphysical solutions.

Method of Characteristics The prototype for second order, hence nonlinear, differential equations is the BURGER's equation.

$$\partial_t u + u \partial_x u = \epsilon \partial_x^2 q, \quad (60)$$

where $u(x, t)$ represents the velocity at position x at time t . Eqn. 60 becomes inviscid in the limit of $\epsilon \rightarrow 0$. The characteristic equations are

$$\frac{dx}{dt} = u \quad \wedge \quad \frac{du}{dt} = 0 \quad (61)$$

with their obvious solutions $x(t) = ut + C_1$ and $u(t) = C_2$. Since C_2 must be a function of C_1 , we derive a general solution for eqn. 60 in the inviscid limit.

$$u = C_2(C_1) \iff u(x, t) = C_2(x - ut) \quad (62)$$

Now, if we set the initial condition to $u(x, 0) = 1 - \cos(x)$ and let it evolve, we get unphysical multi-valued solutions at some point in time. See fig. 2. The reason for this behaviour is the intersection of characteristics (cf. fig. 3) due to the nonlinearity of the inviscid Burgers' equation.

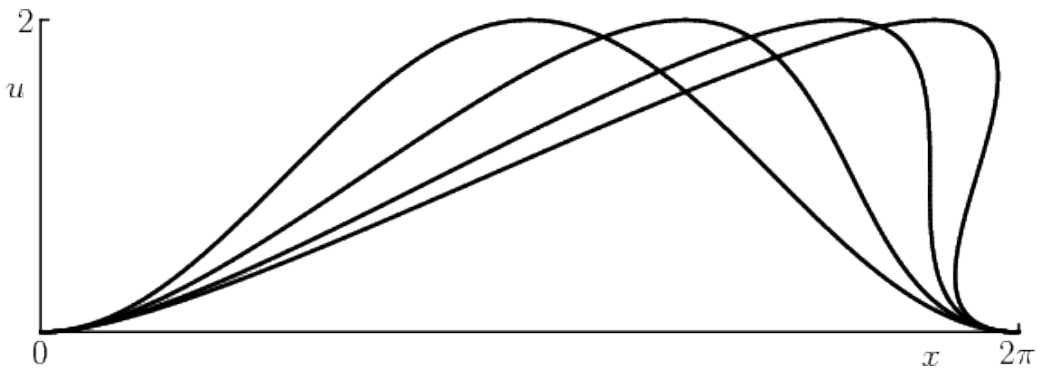


Figure 2: Source: [47]. Multiple snapshots at successive timesteps of the initial condition $u(x, 0) = 1 - \cos(x)$ evolving under the inviscid Burger's equation (eqn. 60). It eventually develops a shock and becomes multi-valued, which is unphysical.

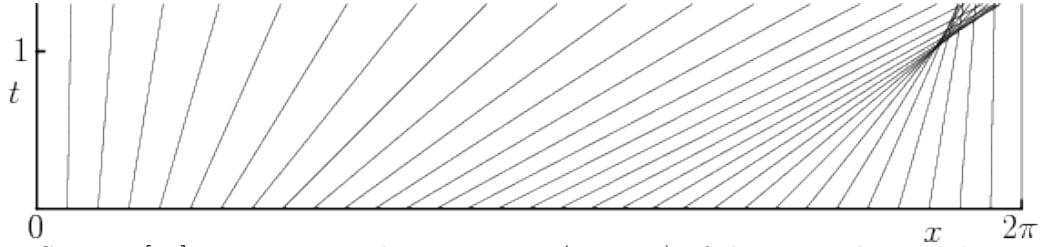


Figure 3: Source: [47]. Intersecting characteristics (eqn. 61) of the inviscid Burger's equation (cf. eqn. 60) are symptoms of a shock wave. The left area where lines diverge from each other is called *rarefaction fan*. Converging lines are part of the *compression fan*. The region of intersection marks the shock discontinuity, where the solution (cf. fig. 2) becomes multi-valued.

Riemann Problem The correct modelling of shocks is summarized under the term *Riemann problem*. It provides the theoretical basis for the correct treatment of discontinuities in solutions of nonlinear PDEs. Furthermore, the Riemann problem is an integral part of finite element schemes who approximate the exact solution by piecewise constant or polynomial functions as finite volume and discontinuous Galerkin methods, respectively, do. Further discussion follows in sec. 2.4.3.

Gibb's Phenomenon An inherent downside of schemes involving polynomials is the GIBB'S phenomenon. It states that polynomials of higher order, trying to approximate discontinuities, yield spurious oscillations. See fig. 4. There are many approaches to get the ringing near shocks under control. Two of them, *Artificial Viscosity* and *FV-DG mode switching*, are presented in sec. 3.3.

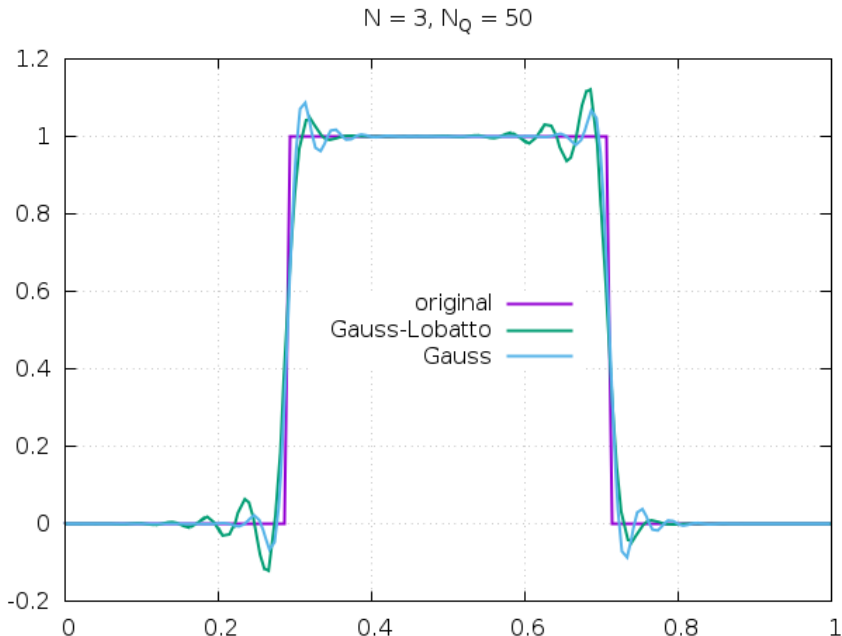


Figure 4: Examples of spurious oscillation of the discontinuous Galerkin method solving the one-dimensional advection equations with a discontinuous initial condition. The domain is divided into 50 elements each containing a third-order polynome. Gauss and Gauss-Lobatto are two types of distributing interpolation nodes within each element (cf. sec. 3.4).

2.4 Finite Element Schemes

Under the motto “Divide and Conquer” the physical domain is cut into smaller subdomains or finite elements. All finite elements methods (FEM) contain multiple stages of operation and are explained briefly.

Meshing Divide the problem domain into adjunct self-contained sub-domains, called elements or cells. Depending on the scheme and requirements this step can happen periodically. Via *Adaptive Mesh Refinement* (AMR) small scale phenomena within the simulation can be resolved where needed without degrading the overall performance disproportionately. AMR is not part of any simulation conducted in this thesis.

Reconstruction Approximate the exact solution in every element by a piecewise constant function (finite volume scheme) or polynome of order N_p (Galerkin scheme). See sec. 2.4.1.

Evolution Based on the current set of variables the governing equations (compressible Euler equations) yield a new state which gets evolved one timestep into the future. See sec. 2.4.2.

Averaging/Propagation Flux functions solve the RIEMANN problem and communicate the lately acquired state across boundaries and propagate the new information throughout the element. See sec. 2.4.3.

2.4.1 Discontinuous Galerkin Method

By refining the mesh, the error in the numerical approximation of the physical solution decays algebraically, that is, introducing more elements. Traditionally, numerical steps in space or time are labeled with the letter “h”. Hence, mesh refinement is also known as *h-refinement*.

An alternative approach is to keep the number of subdomains fixed and increase the order of the interpolating polynomials. This is called *p-refinement*. For infinitely smooth solutions p-refinement can even lead to exponential convergence rates (cf. [46]).

Discontinuous Galerkin methods combine h- and p-refinement by defining higher-order polynomial functions in each finite element to approximate the exact solution. This way, they are able to model discontinuities by solving the Riemann problem at the boundaries of each element.

DG methods have the following main advantages over finite volume methods:

- The order of accuracy only depends on the physical solution. By suitably choosing the degree of the approximating polynomials they can obtain an arbitrarily high order of accuracy. (cf. [51])
- They are highly parallelizable. Since the elements are discontinuous and transformed to a reference element, the mass matrix (eqn. 70) becomes block diagonal. The blocks must be inverted beforehand just once, since their size is equal to the number of degrees of freedom. This massively improves performance.
- In essence, they provide fast convergence, small diffusion and dispersion errors, better data volume-over-surface ratio for efficient parallel processing and better input/output handling due to the smaller volume of data.

It follows a brief derivation of the DG method. At first the physical domain Ω is divided into a *mesh* of adjunct self-contained sub-domains Ω_l ($l \in \mathbb{N}$) with well-defined boundaries. Every

element Ω_l gets transformed to the reference space $\hat{\Omega} = [-1, 1]^3$. For the sake of clarity, we assume a Cartesian grid, drop any transformation pre-factor and set $\Omega = \Omega_l = \hat{\Omega}$.

The unknown solution \mathbf{U} is now replaced by polynomials of order N_p constructed from linear combinations of orthogonal basis functions Ψ^j .

$$U_i(t, x, y, z) \approx p_i(t, x, y, z) = \sum_{j=0}^{N_p} U_i^j(t) \Psi^j(\mathbf{x}) \quad i \in \{1, 2, 3, 4, 5\} \quad (63)$$

The following treatment is analog for all five conservative variables of the Euler equation, so we ignore the index i . Remembering the general weak formulation in eqn. 30 of the solution integral,

$$\begin{aligned} & \int_{\Omega} \left(\sum_{j=0}^{N_p} (\partial_t U^j(t)) \Psi^j(\mathbf{x}) \right) \phi(\mathbf{x}) d^3x = \int_{\Omega} S(t) \phi(\mathbf{x}) d^3x \\ & + \int_{\partial\Omega} [F(t) \phi(\mathbf{x}) n_x + G(t) \phi(\mathbf{x}) n_z + H(t) \phi(\mathbf{x}) n_z] d^2x, \\ & - \int_{\Omega} \left[\left(\sum_{j=0}^{N_p} F^j(t) \Psi^j(\mathbf{x}) \right) \partial_x \phi(\mathbf{x}) + \left(\sum_{j=0}^{N_p} G^j(t) \Psi^j(\mathbf{x}) \right) \partial_y \phi(\mathbf{x}) + \left(\sum_{j=0}^{N_p} H^j(t) \Psi^j(\mathbf{x}) \right) \partial_z \phi(\mathbf{x}) \right] d^3x, \end{aligned} \quad (64)$$

where we put the time variable into the coefficients S, F, G, H and the space variables into the basis functions Ψ and test functions ϕ .

Lagrange Polynome If we associate the basis functions $\Psi^j := L^j$ and the test functions $\phi := L^i$ with LAGRANGE polynomials of equal order N_p , we can formulate an interpolation and integration scheme (*collocation*) over the domain Ω . The polynome in one dimension reads as follows

$$l_j(x) = \prod_{k=0, k \neq j}^p \frac{x - x_k}{x_j - x_k} \quad j = 0, \dots, p, \quad (65)$$

with the KRONECKER property $l_j(x_i) = \delta_{ij}$. Fig. 5 shows a third-order ($N_p = 3$) Lagrange interpolation of a smooth function at four arbitrary interpolation or *anchor* nodes.

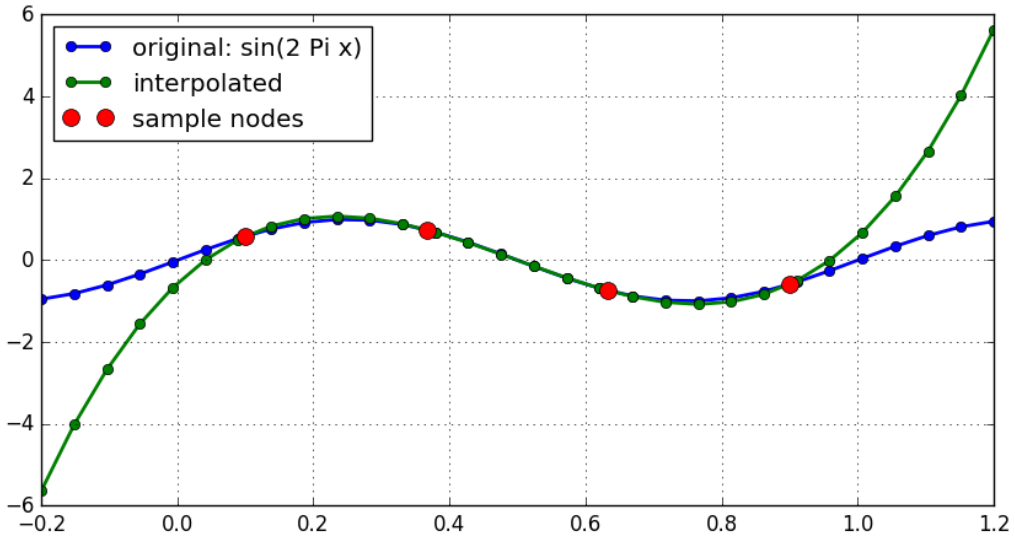


Figure 5: The one-dimensional Lagrange polynome of third order ($N_p = 3$) needs four anchor nodes with their associated values in order to approximate the exact function. Note the minor deviation from the original. This is the interpolation error. Beyond the fringes the Lagrange polynome goes to infinity.

We get to the three-dimensional formulation via the *Tensor Product Ansatz*.

$$L_{\mathbf{i}}(\mathbf{x}) = L_{ijk}(x, y, z) = l_i(x) \cdot l_j(y) \cdot l_k(z) \quad (66)$$

and write the three-dimensional interpolating polynome as:

$$P^{\mathbf{i}}(t, \mathbf{x}) = \sum_{\mathbf{i}=0}^{N_p} F_{\mathbf{i}}(t) L_{\mathbf{i}}(\mathbf{x}) = \sum_{i,j,k=0}^{N_p} f_{ijk}(t) \cdot l_i(x) \cdot l_j(y) \cdot l_k(z), \quad (67)$$

where \mathbf{i} is a three-dimensional *multi-index*.

$$\mathbf{i} = (i, j, k)^T, \quad i, j, k \in \mathbb{N}_0 \quad (68)$$

Note that the time varying part of the polynome lives in the coefficients. Keep this in mind. Going back to eqn. 64 and replacing Ψ^j and ϕ with Lagrange polynomes $L_{\mathbf{i}}(\mathbf{x})$, we get an explicit ansatz, called *Galerkin polynome*.

$$\begin{aligned} & \int_{\Omega} \left(\sum_{\mathbf{j}=0}^{N_p} \dot{U}_{\mathbf{j}}(t) L_{\mathbf{j}}(\mathbf{x}) \right) L_{\mathbf{i}}(\mathbf{x}) d^3x = \int_{\Omega} S(t, \mathbf{x}) L_{\mathbf{i}}(\mathbf{x}) d^3x \\ & + \int_{\partial\Omega} \left[F(t) n_x(\mathbf{x}) + G(t) n_y(\mathbf{x}) + H(t) n_z(\mathbf{x}) \right] L_{\mathbf{i}}(\mathbf{x}) d^2x \\ & - \int_{\Omega} \left[\left(\sum_{\mathbf{j}=0}^{N_p} F_{\mathbf{j}}(t) L_{\mathbf{j}}(\mathbf{x}) \right) \partial_x L_{\mathbf{i}}(\mathbf{x}) + \left(\sum_{\mathbf{j}=0}^{N_p} H_{\mathbf{j}}(t) L_{\mathbf{j}}(\mathbf{x}) \right) \partial_y L_{\mathbf{i}}(\mathbf{x}) + \left(\sum_{\mathbf{j}=0}^{N_p} G_{\mathbf{j}}(t) L_{\mathbf{j}}(\mathbf{x}) \right) \partial_z L_{\mathbf{i}}(\mathbf{x}) \right] d^3x \end{aligned} \quad (69)$$

Evaluating above formula at discrete nodes $\mathbf{x}_{\mathbf{i}}$ (cf. sec. 3.4) and introducing *integration weights*

$$\omega_{\mathbf{i}} = \int_{\Omega} L_{\mathbf{i}}(\mathbf{x}) d^3x \quad (70)$$

we can discretize the continuous integrals.

$$\begin{aligned}
& \sum_{\mathbf{k}=0}^{N_p} \left(\sum_{\mathbf{j}=0}^{N_p} \dot{U}_{\mathbf{j}}(t) L_{\mathbf{j}}(\mathbf{x}_{\mathbf{k}}) \right) L_{\mathbf{i}}(\mathbf{x}_{\mathbf{k}}) \omega_{\mathbf{k}} = \sum_{\mathbf{k}=0}^{N_p} S(t, \mathbf{x}_{\mathbf{k}}) L_{\mathbf{i}}(\mathbf{x}_{\mathbf{k}}) \omega_{\mathbf{k}} \\
& + \left[F^*(t) + G^*(t) + H^*(t) \right] L_{\mathbf{j}} \Big|_{\partial\Omega} \\
& - \sum_{\mathbf{k}=0}^{N_p} \left[\left(\sum_{\mathbf{j}=0}^{N_p} F_{\mathbf{j}}(t) L_{\mathbf{j}}(\mathbf{x}_{\mathbf{k}}) \right) L_{\mathbf{i}}^{(x)}(\mathbf{x}_{\mathbf{k}}) + \left(\sum_{\mathbf{j}=0}^{N_p} H_{\mathbf{j}}(t) L_{\mathbf{j}}(\mathbf{x}_{\mathbf{k}}) \right) L_{\mathbf{i}}^{(y)}(\mathbf{x}_{\mathbf{k}}) + \left(\sum_{\mathbf{j}=0}^{N_p} G_{\mathbf{j}}(t) L_{\mathbf{j}}(\mathbf{x}_{\mathbf{k}}) \right) L_{\mathbf{i}}^{(z)}(\mathbf{x}_{\mathbf{k}}) \right] \omega_{\mathbf{k}},
\end{aligned} \tag{71}$$

where $\sum_{\mathbf{k}=0}^{N_p} A_{\mathbf{ik}} B_{\mathbf{kj}}$ is the *tensor contraction* operation. The partial differential ∂_x turned into a discrete linear operator.

$$L_{\mathbf{j}}^{(x)}(\mathbf{x}) = \partial_x L_{\mathbf{j}}(\mathbf{x}) = (\partial_x l_{j_1}(x)) \cdot l_{j_2}(y) \cdot l_{j_3}(z) \tag{72}$$

$$D_{\mathbf{ij}}^{(x)} = D_{i_1 i_2 i_3 j_1 j_2 j_3}^{(x)} = l_{j_1}^{(x)}(x_{i_1}) \cdot l_{j_2}^{(y)}(y_{i_2}) \cdot l_{j_3}^{(z)}(z_{i_3}) \tag{73}$$

The operators for the y- and z-dimension are constructed in analog manner. The surface term got replaced by flux functions F^* (cf. sec. 2.4.3) where the exchange of mass, momentum and energy across subdomain/element boundaries takes place.

Weak Formulation Finally, we arrive at the semi-discrete *weak formulation* of the discontinuous Galerkin method which can be directly translated to computer code.

$$\begin{aligned}
& \sum_{\mathbf{k}=0}^{N_p} \left(\sum_{\mathbf{j}=0}^{N_p} \dot{U}_{\mathbf{j}}(t) L_{\mathbf{j}}(\mathbf{x}_{\mathbf{k}}) \right) L_{\mathbf{i}}(\mathbf{x}_{\mathbf{k}}) \omega_{\mathbf{k}} = \sum_{\mathbf{k}=0}^{N_p} S(t, \mathbf{x}_{\mathbf{k}}) L_{\mathbf{i}}(\mathbf{x}_{\mathbf{k}}) \omega_{\mathbf{k}} \\
& + \left[F^*(t) + G^*(t) + H^*(t) \right] L_{\mathbf{j}} \Big|_{\partial\Omega} \\
& - \sum_{\mathbf{k}=0}^{N_p} \left[\left(\sum_{\mathbf{j}=0}^{N_p} F_{\mathbf{j}}(t) L_{\mathbf{j}}(\mathbf{x}_{\mathbf{k}}) \right) D_{\mathbf{ki}}^{(x)} + \left(\sum_{\mathbf{j}=0}^{N_p} H_{\mathbf{j}}(t) L_{\mathbf{j}}(\mathbf{x}_{\mathbf{k}}) \right) D_{\mathbf{ki}}^{(y)} + \left(\sum_{\mathbf{j}=0}^{N_p} G_{\mathbf{j}}(t) L_{\mathbf{j}}(\mathbf{x}_{\mathbf{k}}) \right) D_{\mathbf{ki}}^{(z)} \right] \omega_{\mathbf{k}}
\end{aligned} \tag{74}$$

Remark If the polynomial order is set to one ($N_p = 1$) the formulation reduces to the first order finite volume method!

2.4.2 Time Integration

The semi-discrete weak formulation in eqn. 74 of the DG method is nothing more than an ordinary differential equation of the form

$$\frac{d}{dt} y = f(t, y). \tag{75}$$

Defining initial values $y(t_0) = y_0$, this equation can be numerically solved in the most naive way via the *explicit EULER* (EU) method. Choosing an appropriate timestep Δt we can explicitly integrate from the current state y^n to the future state y^{n+1} .

$$y^{n+1} = y^n + \Delta t \cdot f(t^n, y^n) \tag{76}$$

However, if the Δt -convergence rate is worse than the h-p-refinement (cf. sec. 2.4.1) it would render the advantages of the Galerkin method useless. A widely used class of higher-order time integration schemes with good convergence properties are the explicit Runge-Kutta methods (RK). The second-order RK, resp. *midpoint* method (MP), reads

$$y^{n+1} = y^n + \Delta t \cdot f \left(t^n + \frac{\Delta t}{2}, y^n + \frac{\Delta t}{2} \cdot f(t^n, y^n) \right), \quad (77)$$

evaluating the integrand two times per timestep. Introducing again another timestep, the integration becomes of third order (RK3):

$$y^{n+1} = y^n + \frac{1}{6} (k_1 + 4 k_2 + k_3), \quad (78)$$

where

$$k_1 = \Delta t \cdot f(t^n, y^n) \quad (79)$$

$$k_2 = \Delta t \cdot f \left(t^n + \frac{\Delta t}{2}, y^n + \frac{\Delta t}{2} \cdot f(t^n, y^n) \right) \quad (80)$$

$$k_3 = \Delta t \cdot f (t^n + \Delta t, y^n - k_1 + 2 k_2). \quad (81)$$

Courant-Friedrichs-Lowy condition To keep a numerical algorithm stable, the time step has to obey the *Courant-Friedrichs-Lowy condition* (CFL condition). It requires that the domain of dependence, that is q_i^{n+1} at future time t^{n+1} , should include the true domain of the dependence at time $t = t^n$. Or in other words: nothing is allowed to flow more than one grid spacing Δx within one time step Δt . This means quantitatively

$$\Delta t \leq \frac{\Delta x}{u} \quad (82)$$

Given a CFL number: $0 < CFL \leq 1$

$$\Delta t = CFL \cdot \min_x \left(\frac{\Delta x}{u(x)} \right) \quad (83)$$

The CFL condition is a necessary, but not sufficient, condition for the stability of any explicit differencing method. With increasing order of the Runge-Kutta scheme the stability increases though. RK3 even allows the CFL number, in some cases, to be greater 1 (cf. [21]).

In a three-dimensional orthogonal domain the timestep reads

$$\Delta t = C \cdot \min_{\mathbf{r}} \left(\frac{dx}{|v_x(\mathbf{r})| + c(\mathbf{r})}, \frac{dy}{|v_y(\mathbf{r})| + c(\mathbf{r})}, \frac{dz}{|v_z(\mathbf{r})| + c(\mathbf{r})} \right) \quad (84)$$

For supersonic regimes the sound speed c can be neglected.

2.4.3 Flux Functions

Finite Element methods must solve the Riemann problem (cf. sec. 2.3) at the element boundaries in order to exchange information. The *Rankine–Hugoniot conditions* or *shock jump conditions* require that mass, momentum and energy must be conserved when crossing the boundaries. The theoretical framework of the Riemann problem knows a procedure that provides an exact solution to a given shock problem. Unfortunately, an exact Riemann solver is in most cases hard to construct and even harder to compute due to bad convergences rates.

Hence, a wide variety of approximate Riemann solvers or *flux functions* have been proposed that can be applied much more cheaply than the exact Riemann solver and yet give results that in many cases are equally good when used in high-resolution finite element methods.

A detailed discussion about the theory of flux functions would go beyond the scope of this thesis and has been done extensively elsewhere. See [49, 11]. For reasons given in sec. 3.1, we cannot not study the influence of flux functions on the simulations separately. Hence, in this work, flux functions are just considered an integral part of the numerical scheme.

3 Numerical Prerequisites

3.1 Computational Frameworks

The analyzed numerical solvers are part of the simulation frameworks, FLASH and FLEXI. Since both frameworks have been modified, a complete set of source code is provided, available on the attached DVD. Any changes on the source code were logged by the version control system *git* (<https://git-scm.com>).

FLASH

The project page (<http://flash.uchicago.edu/site/flashcode/>, May 13, 2019) says:

The FLASH code, currently in its 4th version, is a publicly available high performance application code which has evolved into a modular, extensible software system from a collection of unconnected legacy codes. FLASH consists of inter-operable modules that can be combined to generate different applications. The FLASH architecture allows arbitrarily many alternative implementations of its components to co-exist and interchange with each other. A simple and elegant mechanism exists for customization of code functionality without the need to modify the core implementation of the source. A built-in unit test framework combined with regression tests that run nightly on multiple platforms verify the code.

The framework is widely adopted within the astrophysics community and serves as reference for testing and comparing the Galerkin schemes provided by FLEXI. Following hydrodynamics solvers came into use: PPM (cf. [9]), Bouchut 3 and Bouchut 5 (cf. [7, 8]). These solvers are specifically designed for supersonic turbulence simulations.

FLEXI

The project page (<http://www.flexi-project.org>, May 13, 2019) says:

Flexi is developed by the team of the Numerics Research Group hosted at the Institute of Aero- and Gasdynamics at the University of Stuttgart. We are interested in efficient and robust numerical methods for applications in scale resolving CFD and we apply these methods to a variety of large scale physical and industrial problems.

Modifications Flexi provides an implementation of discontinuous Galerkin methods and is primarily focused on air flow applications in research and industries. Thus, the simulation of isothermal supersonic turbulences was originally not supported. Following contributions to the source code had to be implemented beforehand:

polytropic cooling (cf. sec. 2.1/*Equation of State*)

bulk motion correction (cf. sec. 2.1/*Bulk Motion*)

turbulent forcing (cf. sec. 3.2)

shock capturing (cf. sec. 3.3)

Additionally, analysis and data transfer tools were developed (cf. sec. 3.4).

Riemann solver Flexi offers a number of approximate Riemann solvers. After many tests we settled down to the HLLE (Harten-Luv-Lax Entropy-fix) (cf. [3]) flux for two reasons. First, it is not far from the Bouchut solvers (FLASH) in technical terms and it was the only one that did not crash. The latter is the reason, a comparative study with different flux functions was not possible in this thesis.

Time Integration Three different methods of numerical time integration came into use: Euler (FV), Midpoint (MP) and third order Runge-Kutta (RK3) (cf. sec. 2.4.2).

Hybrid Scheme As pointed out in the shock discussion in sec. 2.3, pure Galerkin schemes are not suitable for supersonic turbulence simulations. Therefore, a compromise between FV and DG schemes is used (cf. sec. 3.3) where FV and DG are mixed together to a hybrid scheme (HY). In order to counter-check this scheme, the same simulations were also performed with FV only. See sec. 3.3.

ADDITIONAL TOOLS

The simulations were run on CHEOPS at the RRZK¹ (Univ. of Cologne) and on SUPERMUC² at the LEIBNIZ SUPERCOMPUTING CENTER.

For analyzing and visualizing the data we used the PYTHON scripting language with its large set of scientific libraries³: numpy, pandas, h5py, ipython and matplotlib.

Batch processing of myriads of small scripts was made possible by GNU PARALLEL (cf. [45]).

The scripts and tools are also placed on the attached DVD.

3.2 Turbulent Forcing

In equation eqn. 4, a *source* respectively *forcing* term was introduced into the Euler equations. At each time step a varying force field $\mathbf{f}(t, x, y, z)$ perpetually injects kinetic energy at largest scales (cf. sec. 2.2/*Energy Cascade*). Based on [39], we formulate an ORNSTEIN-UHLENBECK process:

$$d\hat{\mathbf{f}}(\mathbf{k}, t) = F_0 \left[-\hat{\mathbf{f}}(\mathbf{k}, t) dt + (\Theta(k_0 - |\mathbf{k}|) - \Theta(k_1 - |\mathbf{k}|)) \mathbf{P}(\zeta, \mathbf{k}) \cdot d\mathbf{W}_t \right], \quad (85)$$

where $\hat{\mathbf{f}}$ is the Fourier transformed force field $\mathbf{f} = (f_1, f_2, f_3)^T$, \mathbf{k} the wave vector (cf. sec. 2.2.1), t is the physical time, $k_0, k_1 > 0$ and $F_0 > 0$ parameters, $\Theta(k)$ the Heaviside step function and $d\mathbf{W}_t$ the WIENER process. The parameter $\zeta = [0, 1]$ sets the ratio of *compressive* (curl-free) to *solenoidal* (divergence-free) modes in the projection operator $\mathbf{P}(\zeta, \mathbf{k})$

$$(P_{ij})(\zeta, \mathbf{k}) = \zeta P_{ij}^\perp(\mathbf{k}) + (1 - \zeta) P_{ij}^\parallel = \zeta \delta_{ij} + (1 - 2\zeta) \frac{k_i k_j}{k^2}, \quad i, j = \{1, 2, 3\}. \quad (86)$$

For the sake of clarity, eqn. 85 strongly simplifies the actual implementation in FLEXI. The choice of runtime parameters in the driven turbulence setup (cf. sec. 4.2) were set in such

¹<http://rrzk.uni-koeln.de>

²<https://www.lrz.de/services/compute/supermuc/>

³<https://scipy.org>

a way that the code applies the force field as shown in eqn. 85. Due to the Heaviside step functions, a flat energy spectrum from k_0 to k_1 modes is injected. Additionally, the physical time t in eqn. 85 is scaled to the dynamic time $t_d = t/T_d$ beforehand.

Following parameters and their settings are of importance here:

rmsv Desired average *root-mean-square-velocity* of the turbulence. When the specified threshold is reached, small but perpetual injections keep the turbulence in proximity of the *rmsv* (cf. sec. 4.2). The driver modifies the force parameter F_0 via heuristics in order to avoid over- or undershoots.

kmin, kmax Range of modes where to apply forcing (cf. sec. 2.2/*Energy Cascade*). The range is set from 1 to 3. Stirring on only the first mode can be imagined as a force field with distinct features half the size of the box. Higher modes divide the box further down accordingly. Limiting forcing to only first three modes avoids imprinting a factitious powerspectrum on the system.

zeta Parameter between 0 and 1 which sets the ratio of compressive to solenoidal forcing. In this work, *zeta* is set to $\zeta = 0.5$. That is, equal forcing on both driving mechanisms.

A depiction of the velocity field after energy injection for the first time on an initially constant state is shown in fig. 6 as well as its associated velocity powerspectrum (cf. sec. 2.2/*Velocity Powerspectrum*) in fig. 7. Obviously, the majority of kinetic energy is crowded on the first three modes: $k = [1, 3]$. Gradually, the energy moves up to higher modes and creates the desired small scale structures desired for driven turbulence simulations. An example of a fully developed turbulence is shown in fig. 8.

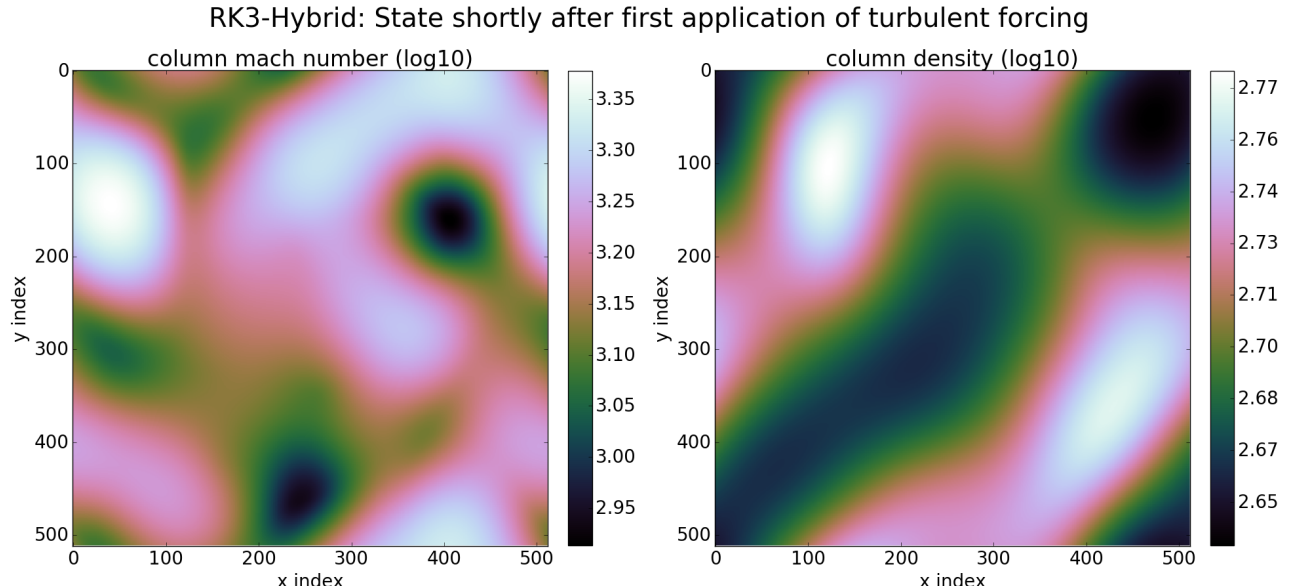


Figure 6: Early-stage snapshot taken immediately after first-time turbulent forcing on the first three modes. The simulation was done in dimensionless units.

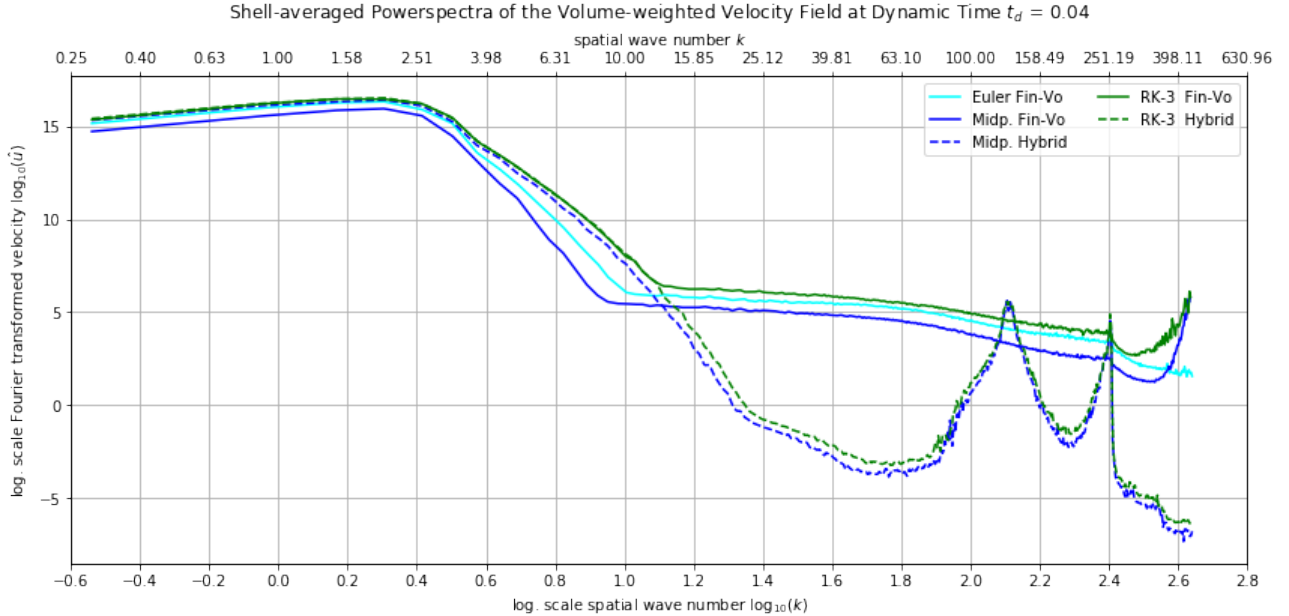


Figure 7: Shell-averaged velocity powerspectrum (cf. sec. 2.2.1) obtained from the velocity (or Mach number in this case) field in fig. 6. The solvers from FLEXI are shown. Obviously, there is a small difference (consider log-log scale!) between the FV-only and hybrid schemes. The distorted spectra on larger modes might be a sign of already emerging oscillations.

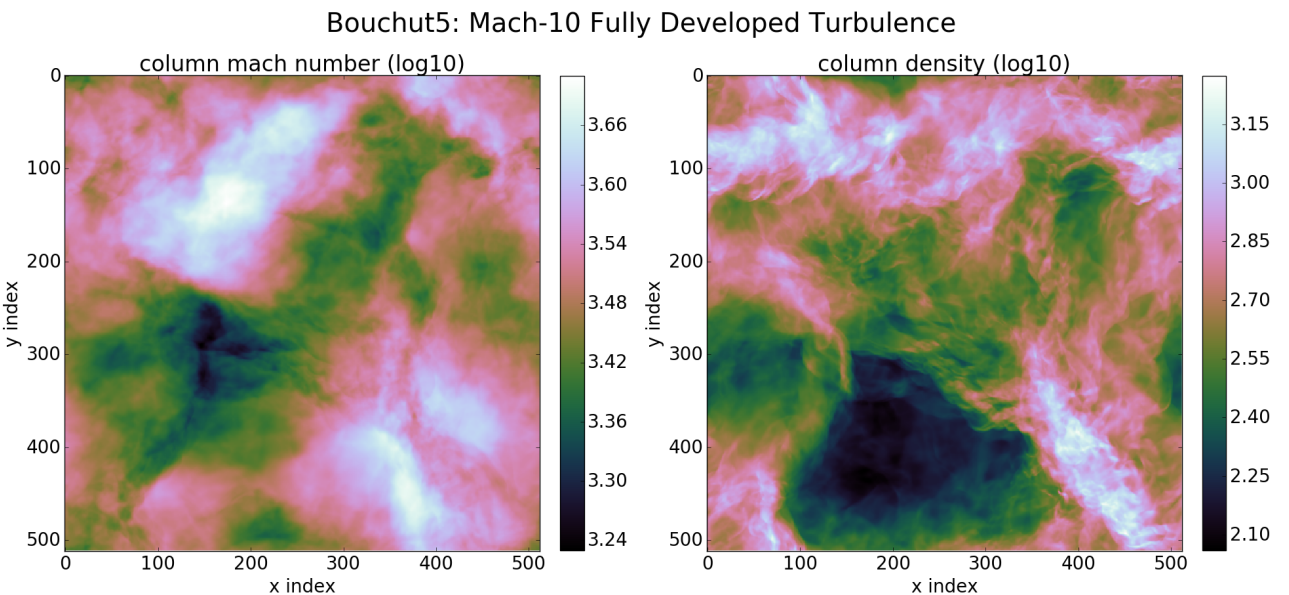


Figure 8: Fully developed Mach-10 turbulence snapshot, simulated with Bouchut5. Forcing was applied on the first three modes and the picture was taken after four crossing times. The formerly smooth large scale waves in fig. 6 compress and smash into each other, yielding tenuous filaments.

3.3 Shock Capturing

In supersonic simulations the solver has to deal with strong shocks in an accurate and robust manner. We utilize shock capturing strategies in order to alleviate the destabilizing impact of discontinuities on DG schemes.

This endeavor, however, is far from trivial because of two main reasons. The first is that the exact solution of (nonlinear) purely convective problems develops discontinuities in finite

time; the second is that these solutions might display a very rich and complicated structure near such discontinuities. Thus, when constructing numerical methods for these problems, it must be guaranteed that the discontinuities of the approximate solution are the physically relevant ones. Also, it must be ensured that the appearance of a discontinuity in the approximate solution does not induce spurious oscillations, see fig. 4, which spoil the quality of the approximation; on the other hand, while ensuring this, the method must remain sufficiently accurate near shocks in order to capture the possibly rich structure of the exact solution (cf. sec. 2.3). Finding a good balance between accuracy and stability is an active field of research (cf. [2, 30, 28]).

Within the scope of this work, three intertwining concepts are developed and implemented in FLEXI. First, we must detect (*sensoring*) a discontinuity and dampen (*artificial viscosity*) the appearing oscillations. In case this is not sufficient, the element switches to FV mode (*switching*) and endures the troubling phase till it can safely revert back to DG mode.

Sensoring Based on the PERSSON indicator (cf. [36]) we develop a *smoothness* operator which measures the variance of the highest frequencies in modal space of the Galerkin polynome. In other words we build an oscillation detector. First we express the solution q of order N_p within each element in terms of an orthogonal basis as

$$q = \sum_{i=1}^{N_p} q_i \psi_i, \quad (87)$$

where N_p is the total number of terms in the expansion and ψ_i are the LEGENDRE basis functions. See fig. 9.

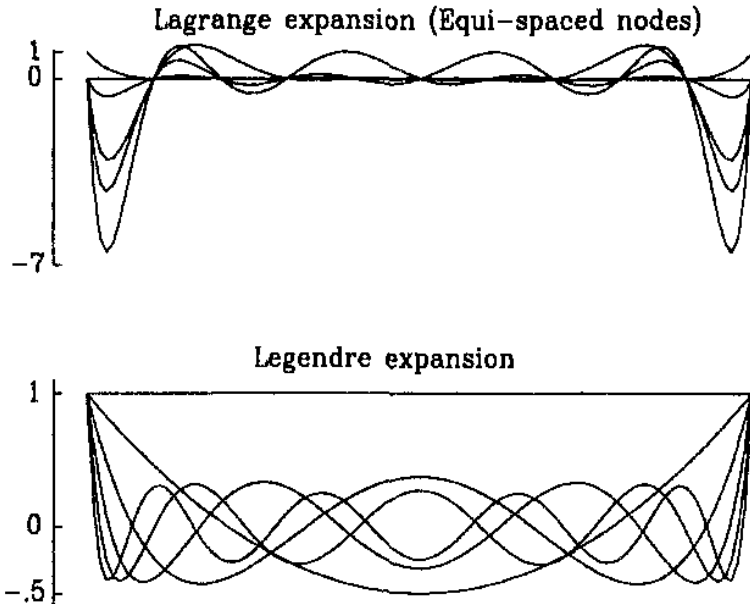


Figure 9: First four expansion modes for the Lagrange and the Legendre basis. They are related by a coordinate transformation from *nodal* to *modal* space. The presence of higher modes in modal space signifies a strongly oscillating interpolant in nodal space.

Now we only consider the terms up to order $N_p - 1$, that is

$$q_{N_p-1} = \sum_{i=1}^{N_p-1} q_i \psi_i, \quad (88)$$

Within each element Ω we define the following *smoothness* sensor

$$s = \log_{10} \frac{\langle q - q_{N_p-1}, q - q_{N_p-1} \rangle}{\langle q, q \rangle}, \quad (89)$$

where $\langle \cdot, \cdot \rangle$ is the standard inner product in $L_2(\Omega)$. The smaller the indicator s , the smoother is the approximated solution. The state variable q is mostly the pressure p , which gives the best results, because pressure jumps are generally very sharp in shocks.

Artificial Viscosity Artificial viscosity $0 < \epsilon \lll 1$ is introduced to the Euler equations by a very weakly interacting diffusion term.

$$\frac{\partial \mathbf{Q}}{\partial t} + \nabla \cdot \underline{\mathbf{F}}(\mathbf{Q}) = \nabla \cdot (\epsilon \nabla \underline{\mathcal{I}}), \quad (90)$$

with $\underline{\mathcal{I}}$ being the deviatoric stress tensor. The amount of viscosity varies for each element and depends on the current shock strength. We have to consider two cases.

If the element is in FV mode, ϵ is set quadratic proportional to the maximum root-mean-square velocity u_{rms}^l of the element l .

$$\epsilon_{FV} = \epsilon_{FV,0} \cdot \max(u_{rms}^l)^2 \quad (91)$$

with $\epsilon_{FV,0}$ being an arbitrary, but sufficiently small constant. This measure should only have an effect on extreme velocity spikes, otherwise the governing equations would get viscous and violate the timestep constraints.

In case of an element in DG mode, the amount of ϵ is based on the *Persson indicator* introduced above.

$$\epsilon_{DG} = \begin{cases} 0 & \text{if } s < s_0 \\ \epsilon_{DG,0} & \text{if } s > s_0 \\ \frac{\epsilon_0}{2} \left(1 + \sin \frac{\pi(s-s_0)}{2\kappa}\right) & \text{else} \end{cases} \quad (92)$$

The parameters $\epsilon_{DG,0}$, s_0 and κ are chosen empirically, but again, $\epsilon_{DG,0}$ must be sufficiently small.

In this thesis, the viscosity constants are set very tiny on purpose: $\epsilon_{DG,0} = \epsilon_{FV,0} = 10^{-10}$. The sole task of this module is to catch extremely high velocity spikes, which happens from time to time, and diffuse them into neighboring elements. Besides that, there is no measurable effect on the simulation.

FV-DG Mode Switching By setting a specific threshold for the *smoothness indicator* s , one can decide when to switch back and forth between DG and FV mode. FLEXI does this by setting a special flag for the element and interpolating from the nodal grid of the polynome to the body-centered grid of the finite volumes. The next section explains this further. The code, that switches between DG and FV elements, is already present in FLEXI. The studies in [4, 43], published by contributors of FLEXI, outline the implementation details. This procedure is done at every timestep, hence the elements in FV mode should follow along the shock waves throughout the domain. We propose a modification of the indicator original to FLEXI, perform a comparative study and clarify the advantage.

Based on eqn. 89 our variant, called *indicator A*, reads

$$s_A = \log_{10} \max \left(\frac{\left| q^2 - q_{N_p-1}^2 \right|^2}{\left| q^2 \right|^2}, \frac{\left| q_{N_p-1}^2 - q_{N_p-2}^2 \right|^2}{\left| q^2 - q_{N_p-1}^2 \right|^2} \right), \quad (93)$$

where $|\cdot| = \sqrt{\langle \cdot, \cdot \rangle}$. The original version, called *indicator B*, reads

$$s_B = \log_{10} \max_M \frac{\left| q - q_{N_p-M} \right|^2}{\left| q_{N_p-M} \right|^2} \quad (94)$$

Fig. 10 shows a fully developed turbulence with shocks and their associated heat maps of indicator values calculated from the pressure. A normalized distribution (PDF) of indicator values s is plotted in fig. 11. The most prominent difference is the higher sensitivity of indicator A and its limitation to only negative values. The latter is a result of the normalizing fractions in eqn. 93. Both variants trail the shock fronts with sufficient accuracy. Considering the PDF in fig. 11, one can observe spikes in both curves in the interval between -1 and 0. They herald the realm of strong shocks. The broad hill around -2.5 contains the majority of stressed elements, which were affected by a recently pervading shock front. The little spike at -4.5 stems from a bias introduced by the indicator A. Numerous tests revealed an empirical threshold of $s_0 = -4.5$ where the switching takes place. Clearly, indicator A unambiguously signalizes elements with unresolvable discontinuities. This opens the possibility to further strengthen the DG scheme for a broader coverage of the domain above $s_0 = -4.5$.

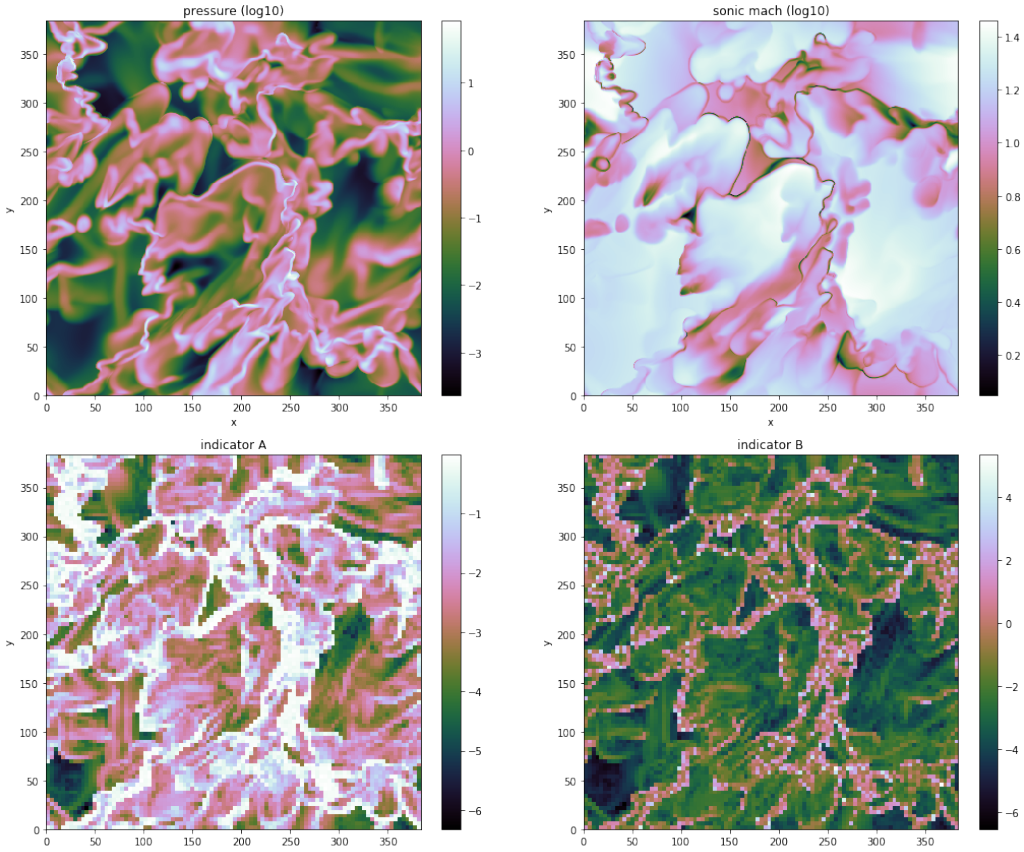


Figure 10: Pressure and Mach Number slices of a Mach-10 driven turbulence similar to fig. 8. Below are the *smoothness* indicators s_A (eqn. 93) and s_B (eqn. 94) derived from the pressure.

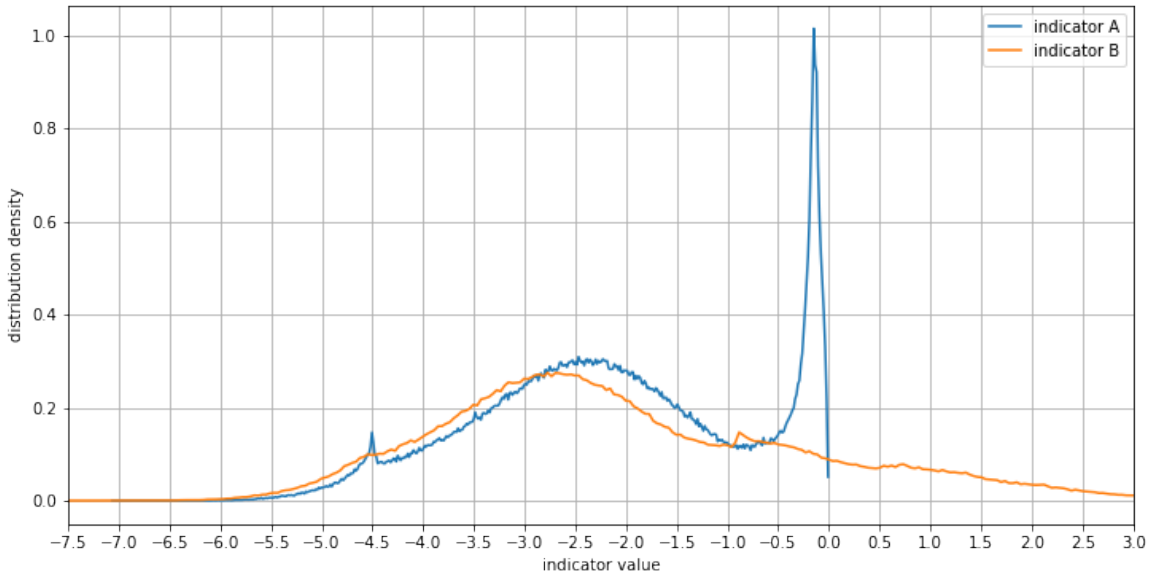


Figure 11: Probability Distribution of *smoothness* indicators s_A (eqn. 93 and s_B (eqn. 94) in a Mach-10 driven turbulence shown in fig. 10. Due to the high spike of indicator A, it is well-suited for distinguishing strong shocks in the pressure field. A more detailed explanation is provided in the text.

3.4 Interpolation & Data Transfer

Grid Spaces The term *grid space* refers to the arrangement of nodes within an element. Four types of node configurations are of importance here: *Face-centered grid* (FCG), *body-centered grid* (BCG), *Gauss nodal grid* (GNG) and *Gauss-Lobatto nodal grid* (LNG). Finite Volumes live on a BCG while the Galerkin polynomials are anchored on either GNG or LNG. Gauss and Gauss-Lobatto nodes are the roots of special polynomials. See fig. 12. They minimize the errors of the *Gauss quadrature* (numerical integration), which is one of the corner stones in the derivation of the Galerkin method as we have done sec. 2.4.1). See [16] for a comparative study of GNG and LNG and further information about this subject.

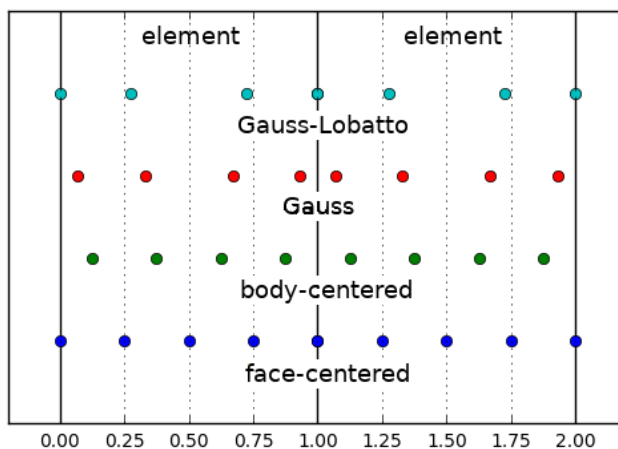


Figure 12: Two finite elements containing four cells/volumes. From top to bottom: Gauss-Lobatto nodes ($N_p = 3$), Gauss nodes ($N_p = 3$), body-centered and face-centered nodes. DG schemes are defined on Gauss and Gauss-Lobatto nodes while FV methods anchor their data at the center of the volumes/cells (body-centered). The exchange of information (flux functions: cf. sec. 2.4.3) happens at the cell boundaries (face-centered).

We only consider Gauss nodes, since the FV-DG mode switching (cf. sec. 3.3) does only support Gauss nodes at the time of writing.

In order to compare and share data between the FV and DG schemes, one has to translate between the different grids via Lagrange interpolation. Although FLEXI offers curvilinear grids, we only need the Euclidean geometry. Thus we have a one-to-one relationship between the four grid spaces and are able to directly lay them on top of each other as depicted in fig. 12.

Interpolation Error is in general inevitable but manageable. See fig. 5 for an interpolation of a trigonometric function. The quality of an interpolation procedure is determined by an error measure which we motivate in the following.

The Lagrange interpolating polynome $L(x)$ of order N is exact for a polynomial function $f(x)$ of order $M \leq N$.

Proof: The remainder $R(x) = L(x) - f(x)$ can be expressed as

$$R(x) = L(x) f^{(N+1)}|_{\zeta}, \quad x_0 \leq \zeta \leq x_N, \quad (95)$$

using Taylor series analysis (cf. [1, p. 878]). x_0, \dots, x_N are the interpolation nodes and $f^{(N+1)}(x)$ is the $(N+1)$ -th derivative of $f(x)$. Since $M \leq N$, $f^{(N+1)}(x) = 0 \Rightarrow R(x) = 0, \forall x$. \square

An example for an exact Lagrange interpolation in two dimensions is shown Fig. 13.

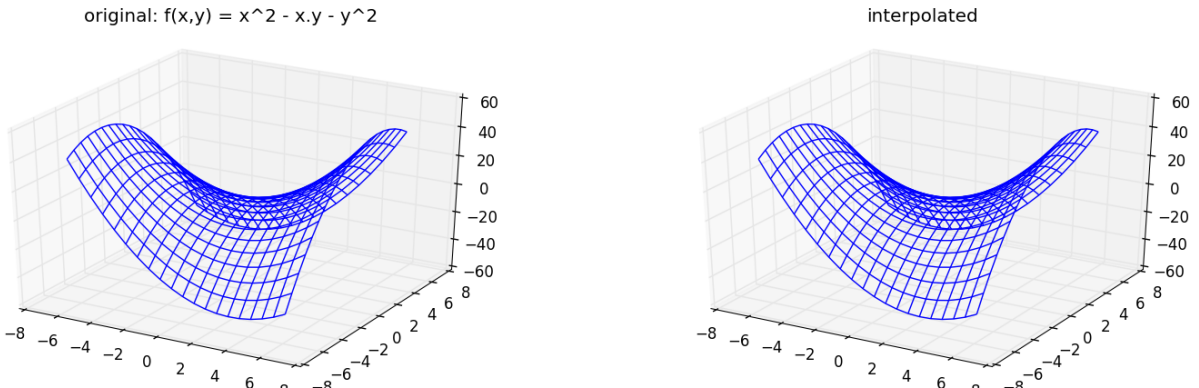


Figure 13: Example of a two-dimensional exact third-order Lagrange interpolation of a second-order polynomial. The relative error $\Delta_{\text{RMS}} = 0.000000\%$ (cf. eqn. 96) is below machine precision.

Instead of the remainder $R(x)$ we define a *root-means-square variance* as a kind of distance measure between an arbitrary function $f(x)$ and its interpolant $\tilde{f}(x)$.

$$\Delta_{\text{RMS}} = (f - \tilde{f})_{\text{RMS}} = \sqrt{\frac{1}{N} \sum_i^N (f_i - \tilde{f}_i)^2}. \quad (96)$$

The relative error is calculated by

$$\Delta_{\text{RMS,rel.}} = \frac{\Delta_{\text{RMS}}}{f_{\text{RMS}}}, \quad (97)$$

where $f_{\text{RMS}} = \sqrt{\frac{1}{N} \sum_i^N f_i^2}$.

Remark One has to ensure that f_i and \tilde{f}_i live in the same grid space.

Transferring Data from FLASH to FLEXI For the decaying turbulence simulations (cf. sec. 4.3) a transfer of initial states from FLASH to FLEXI is necessary. A brief overview of the procedure and some results are discussed.

In order to give a sense of intuition, we imagine a Cartesian grid with 512 body-centered points in each of the three dimensions. Each data point represents a finite-volume, read in from a FLASH checkpoint file. We subdivide the contiguous block of 512^3 into elements of $4^3 = 64$ nodes. Within each element the data gets transformed via three-dimensional third-order Lagrange interpolation into Gauss or Gauss-Lobatta nodal space. Finally, the new data is written to a FLEXI checkpoint file. The reverse procedure is available as well, which is useful for analysis and visualization.

Fig. 14 and fig. 15 show practical results of a data transfer from FLASH to FLEXI. They confirm the applicability of the transfer procedure within acceptable error margins. Unavoidable is the truncation of sharp spikes in the data. Evidently, critical information in the proximity of strong shocks gets lost. Considering this, it is advisable to apply a Gaussian blur before the interpolation step. This way, almost equal initial states in FLASH and FLEXI are ensured.

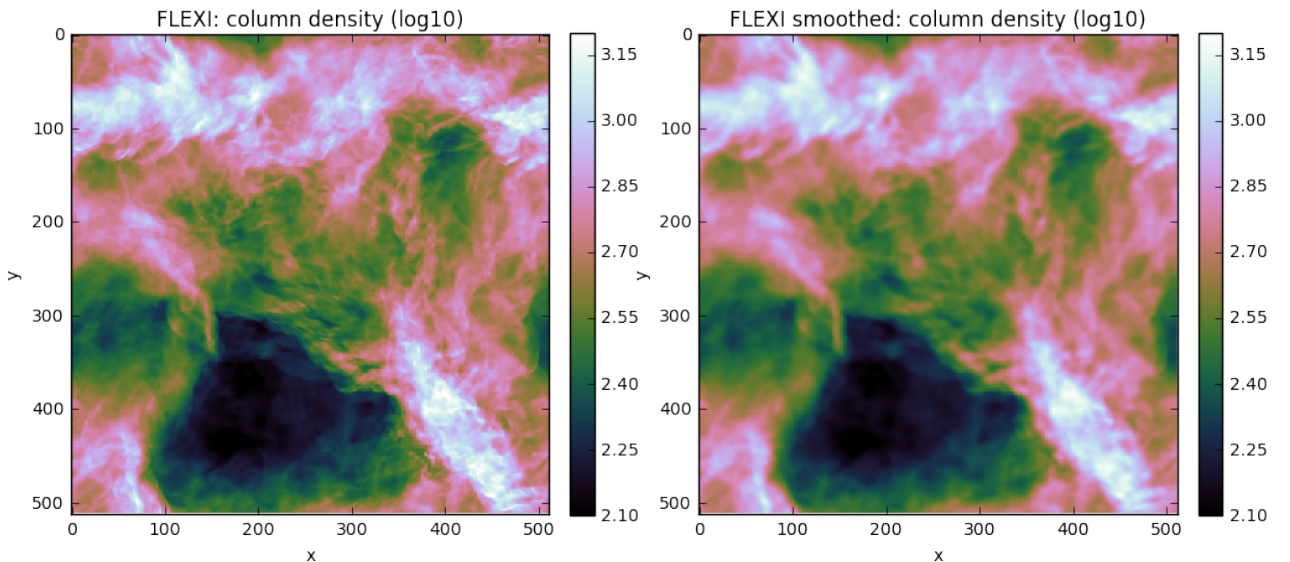


Figure 14: Column densities plots of interpolated supersonic (Mach 10) turbulence (see fig. 8) from FLASH to FLEXI. Left side: The density is interpolated via a third-order (four nodes per element) Lagrange interpolation as described in the text. The relative interpolation error is estimated as $\Delta_{\text{RMS}} = 0.118763 \approx 12\%$ (cf. eqn. 96). Right side: The interpolation can be improved by introducing a Gaussian blur before the interpolation step: $\Delta_{\text{RMS}} = 0.2808160 \approx 3\%$.

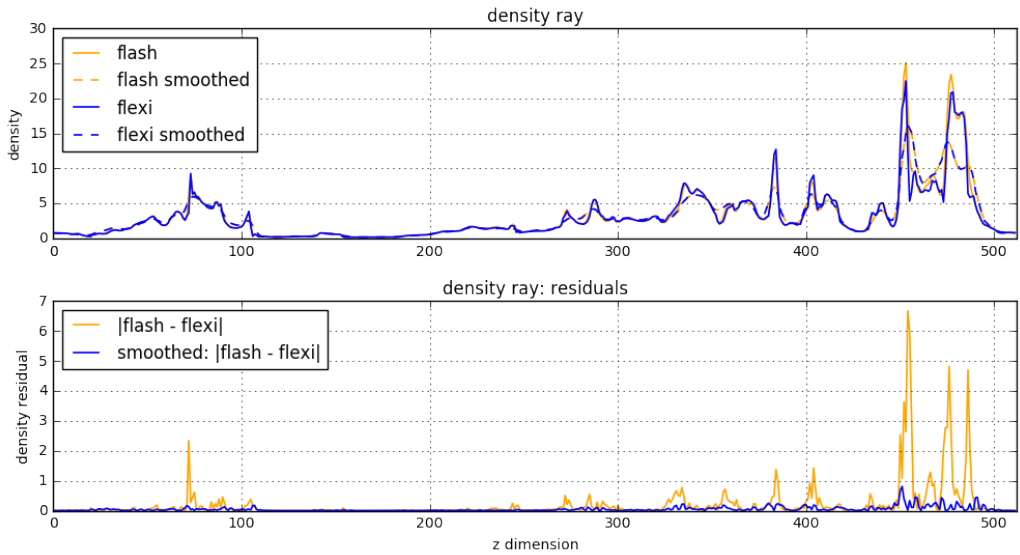


Figure 15: Comparison of one-dimensional density profiles and residuals through a supersonic (Mach 10) turbulent box with original simulation data (flash) and transferred interpolated data (flexi). The density ray is extracted from same data already shown in fig. 8 and fig. 14. The smoothing (before the interpolation) was done via a Gaussian blur which minimizes the residual considerably.

4 Results & Discussion

4.1 Sod Shock Tube Problem

Before we can discuss the results of the turbulence simulations, we need to validate the correctness of the solvers, considering the modifications explained in the previous chapter. The standard test for the correct treatment of shocks is the SOD Shock Tube Problem in one dimension. At first, we look at the classical adiabatic test case, then introduce polytropic cooling (isothermal) and finally apply a strong shock situation by setting the initial left-side velocity to $u_L = 15$. All runs took place with a conservative CFL number of $CFL = 0.4$. If not indicated otherwise the initial conditions were set like follows

Table 1: Sod-Shock: Initial Condition

Left Side			Right Side	
Name	Symbol	Value	Symbol	Value
density	ρ_L	1.0	ρ_R	0.125
velocity	u_L	0.0	u_R	0.0
pressure	p_L	1.0	p_R	0.1

We set a resolution of 512 cells for the domain $\Omega = [0, 1]$, where the discontinuity is at $x_0 = 0.5$. 512 cells resembles the same resolution applied on the turbulence simulations. This way we get a comparable insight on how well shocks can be resolved within a periodic box of equal size. Table 2 outlines the conducted experiments in tabular form.

Table 2: Overview of conducted runs for the Sod Shock Tube Problem

Setups	Adiabatic, Isothermal, Adiabatic w. Strong Shock, Isothermal w. Strong Shock
Solvers	Bouchut 3, Bouchut 5, PPM, Euler FV, Euler Hybrid ¹ , Midp. FV, Midp. Hybrid, RK3 FV, RK3 Hybrid
Resolution	512
CFL	0.4

This setup is not a convergence study or similar. The objective is to test whether FLEXI produces the same results as FLASH under identical initial conditions.

4.1.1 Adiabatic & Isothermal Shock

In fig. 16 all utilized solvers satisfy the expected density profile of the classical Sod-Shock problem with varying precision. PPM yields the most accurate result while on the other hand RK3-Hybrid smears out the discontinuities considerably. Looking closely at the zoomed area all hybrid schemes (blue, yellow and green dashed lines) tend to oscillate. The unacceptable ringing of the Euler-Hybrid is a consequence of the instability of the Euler time integration within the DG operator. Consequently, Euler-Hybrid is disqualified and discarded. Same assertions can be made for the isothermal case shown in fig. 17.

¹Euler Hybrid was only tested for adiabatic and isothermal Sod Shock since it is unstable.

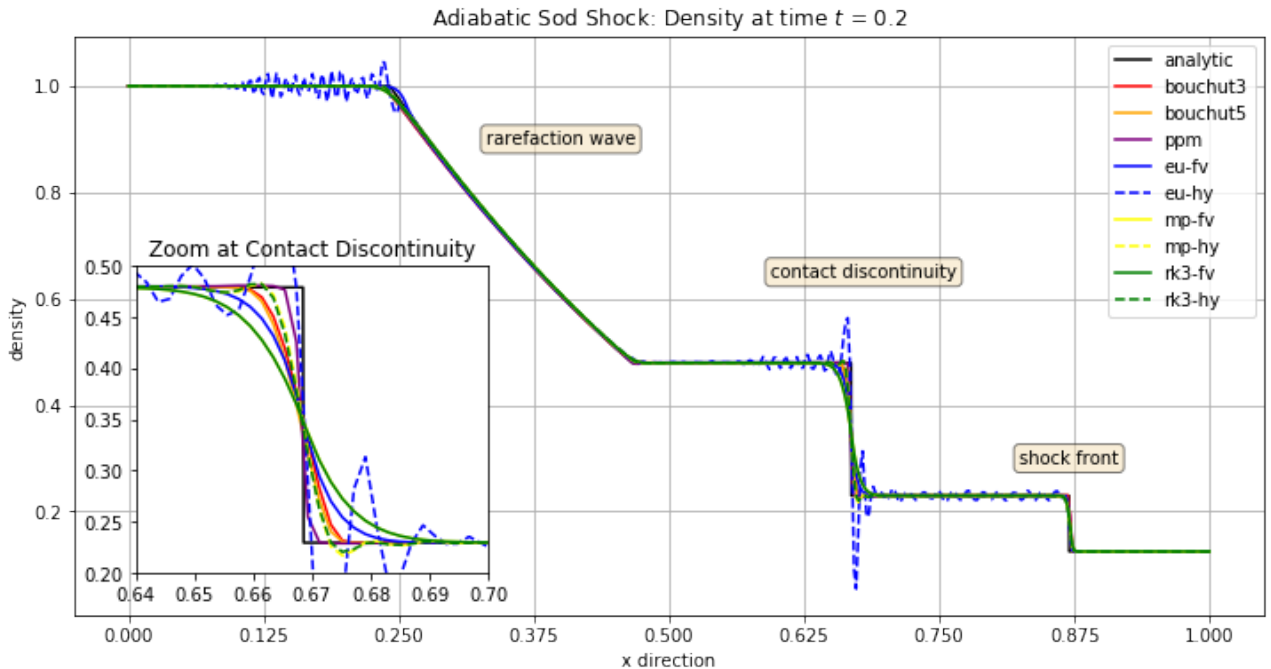


Figure 16: Canonical density profile at the conventional time $t = 0.2$ with anticipated regions and discontinuities outlined in the plot. The formula of the analytical solution is given in [42].

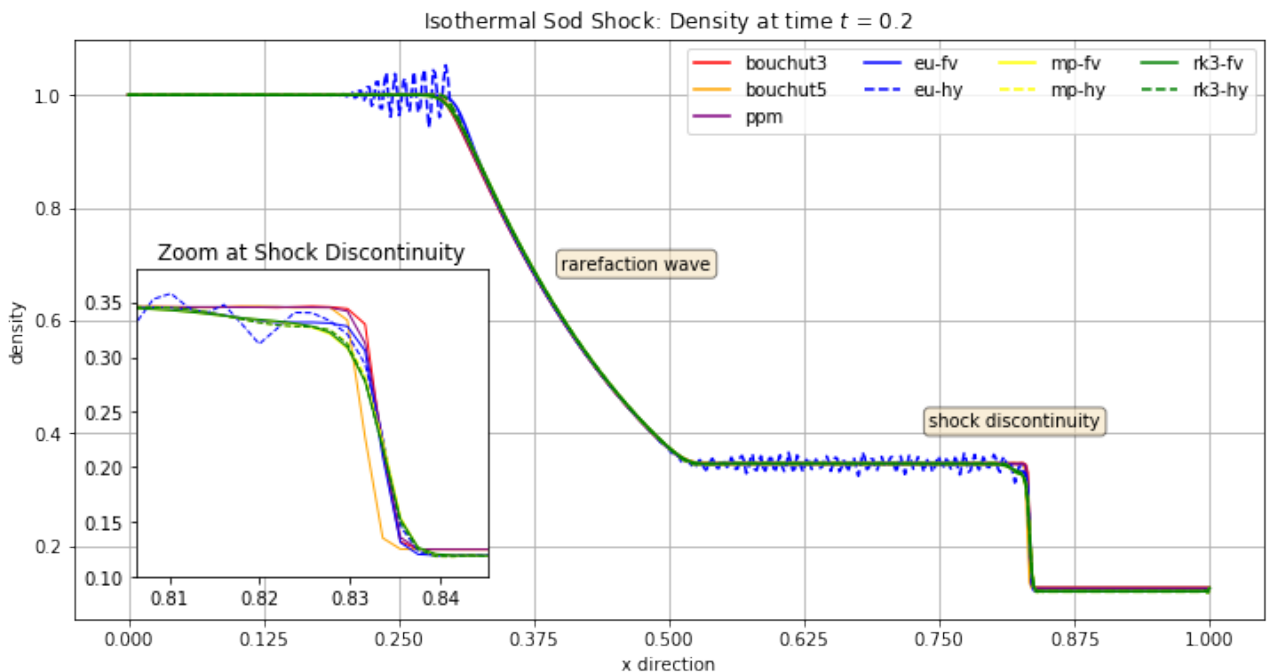


Figure 17: Isothermal density profile at conventional time $t = 0.2$ with expected regions and discontinuities outlined in the plot. The contact discontinuity gets suppressed due to polytropic cooling.

4.1.2 Adiabatic & Isothermal Sod with Strong Shock

Here we compare, how the solvers cope with a strong shock situation ($u_L = 15$), first in the adiabatic and then in isothermal setting with polytropic cooling.

Considering fig. 18 all solutions yield a quite similar profile. The shock waves build up rapidly

up to a certain height, travel at a constant speed from left to right and widen with increasing time. One can recognize two distinct parts. A fast traveling pedestal moving at the speed of the initial velocity $u_{fast} = u_L = 15$ and a slower moving peak at the speed of around two third of the fast wave $u_{slow} \approx 2/3 u_{fast} = 10$. The solutions for the strong shock setup with cooling, see fig. 19, are quite different. Most notably, the density peaks are about a factor of 10 higher and the widths are considerably more narrow than before. There are no recognizable partitions into a slow and fast moving wave. Additionally, the solvers do not agree on the shock wave speed, with the Euler FV being the slowest but highest rising one. We do not have a definite explanation for this, but it should be safe to say that the mean free path of a shock wave in a turbulence simulation does not exceed half the size of the box. Hence, the influence of the velocity dispersion among the solvers is considered negligible.

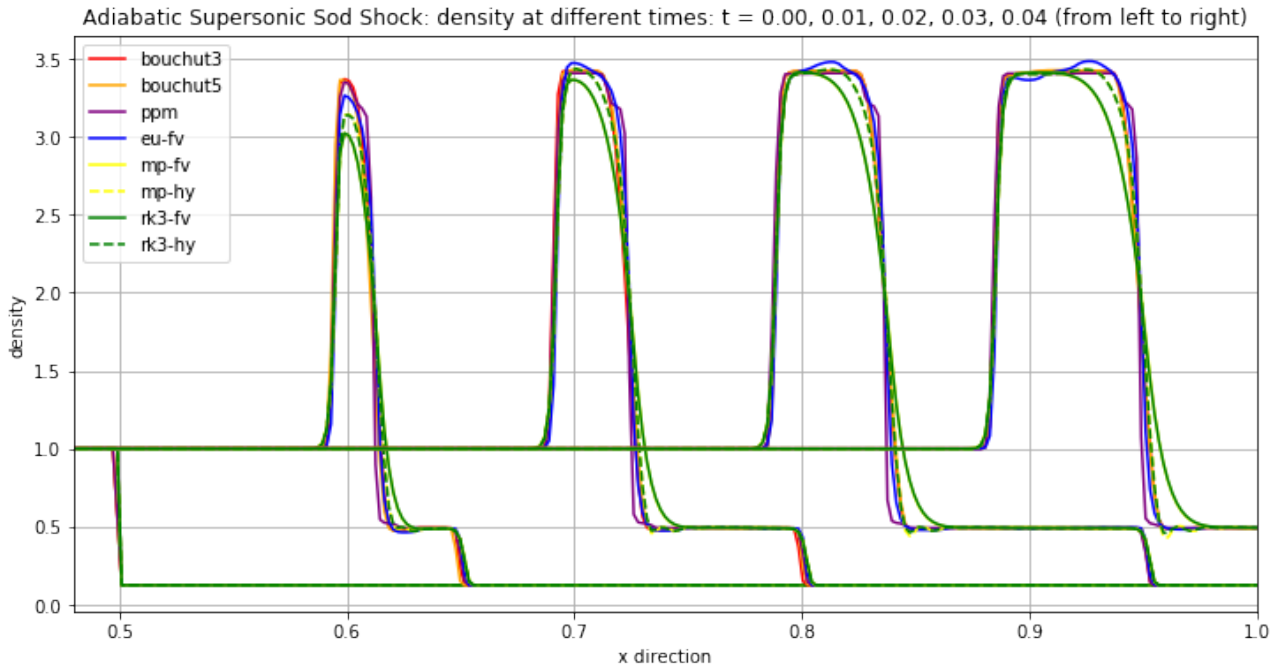


Figure 18: Adiabatic density snapshots depicting the movement of a strong shock wave from left to right. Note: Only the right half of the domain is shown. The pedestal of the rightmost wave ($t_d = 0.04$) has gone out of visible range.

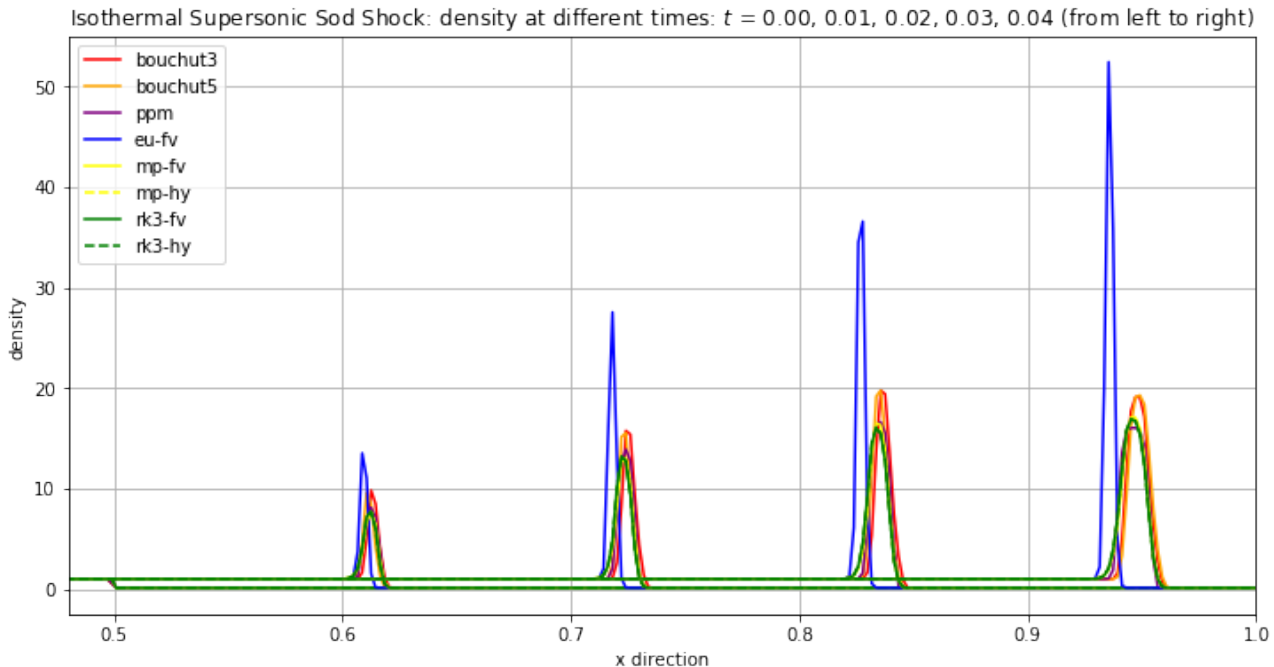


Figure 19: Isothermal density snapshots depicting the movement of a strong shock wave from left to right. Note: Only the right half of the domain is shown.

4.1.3 Summary

We conducted four different Sod shock tube tests in order to validate the correct treatment of shocks by the FLEXI code. The Euler Hybrid scheme rendered invalid since it showed spurious oscillations. Special attention should be given to the Euler FV since it drifted away somewhat from the other solvers for the supersonic strong shock test (cf. fig. 19).

4.2 Driven Turbulence

We conduct an isothermal driven supersonic turbulence simulation in a three-dimensional periodic box of unit length with a resolution of 512 cells in each direction. This kind of setup is very common in ISM simulations and has been studied extensively in the past. See [39, 22, 27, 32].

Originating from the driver, kinetic energy enters the box on large scales and leaves it as internal energy via polytropic cooling on small scales. This way a stationary flow of momentum gets pumped through the system. In conjunction with *bulk motion correction* supersonic turbulent flow emerges, which presents a stress test for every numerical scheme.

The simulation consists of three phases. At the beginning of the run, turbulent forcing (cf. sec. 3.2) stirs the medium up to a certain root-mean-square velocity, which is equivalent to the sonic Mach number $\mathcal{M}_{\text{forcing}}$ (cf. sec. 2.1/Choice of Parameters). Prior tests have shown that FLEXI becomes unstable for driven turbulences with Mach numbers beyond 3. Consequently, we settled to $\mathcal{M}_{\text{forcing}} = 2.5$, keeping a small safety gap.

One crossing time amounts to $T_d = L/\mathcal{M} = 1/2.5 = 0.4$. When reaching $\mathcal{M} = 2.5$ as fast as possible, but slow enough not to over strain the solver, the stirring module perpetually injects just enough energy to stay in proximity of $\mathcal{M}_{\text{forcing}}$. The turbulence is given four crossing times to fully develop, after which forcing is deactivated. We will call this the *turbulent phase*.

During the *decay phase* it takes another two turning times to let the turbulence drop below the supersonic barrier (cf. [44], [32]).

Based on the considerations in sec. 2.1, we initialize the state as listed in table 3.

Table 3: Outline of initial condition for all driven turbulence simulations

primitive variables			conservative variables		
Name	Symbol	Value	Name	Symbol	Value
density	ρ_0	1.0	density	ρ_0	1.0
x-velocity	$u_{x,0}$	0.0	x-momentum	$\mathcal{P}_{x,0}$	0.0
y-velocity	$u_{y,0}$	0.0	y-momentum	$\mathcal{P}_{y,0}$	0.0
z-velocity	$u_{z,0}$	0.0	z-momentum	$\mathcal{P}_{z,0}$	0.0
pressure	$p_{x,0}$	0.6	total energy	$E_{x,0}$	0.9

Remark Bouchut 3 and Bouchut 5 actually solve the ideal magneto-hydrodynamics (MHD) equations. By setting the initial magnetic density flux $\mathbf{B}_0 = 0$, the MHD equations reduce to the compressible Euler equations.

Apart from the Mach number, the course of energy and energy dissipation are measured. Additionally, we look at selected density distributions and powerspectra during the turbulent and decay phase. Checkpoints for analysis and plotting are saved ten times per crossing time. Table 4 gives an overview of the conducted experiments.

Table 4: Outline of Driven Turbulence Simulations

Solver	B3	B5	PPM	EU-FV	MP-FV	MP-HY	RK3-FV	RK3-HY
Resol. per Dim.	512	512	512	512	512	512	512	512
CFL	0.8	0.8	0.8	0.4	0.8	0.6	0.9	1.2
$\mathcal{M}_{\text{forcing}}$	2.5	2.5	2.5	2.5	2.5	2.5	2.5	2.5
$t_{\text{forcing,stop}}$	4.0	4.0	4.0	4.0	4.0	4.0	4.0	4.0
$t_{\text{sim. end}}$	6.0	6.0	6.0	6.0	6.0	6.0	6.0	6.0
$N_{\text{checkpoints}}$	60	60	60	60	60	60	60	60

4.2.1 Mach Number Evolution

Fig. 20 clearly depicts the stir-up, turbulent and decay phases. After a steep stirring phase of roughly 0.1 turning times the forcing routine keeps the solvers from decaying below $\mathcal{M} = 2.5$. The differences in rising times and saw-tooth shapes in the zoomed picture (fig. 20) are a result of different timesteps.

The decay rates from $t_d = 4$ to 6 (decay phase) diverge considerably. The best results with regards to retaining most kinetic energy, see also fig. 28, is the Euler FV followed by both RK3 solvers. PPM and Bouchut 3 and Bouchut 5 are in the middle. Both Midpoint solvers seem to be most dissipative and end up at roughly $\mathcal{M} = 0.75$ at $t_d = 6$.

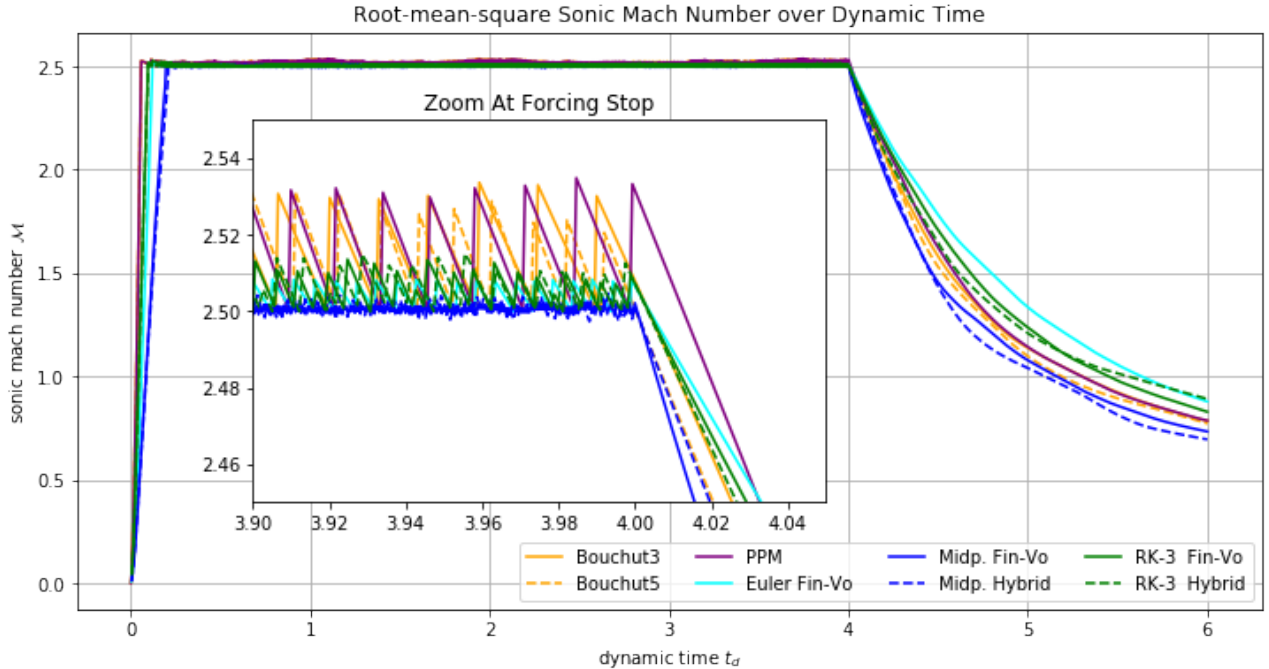


Figure 20: Time evolution of the root-mean-square Mach number \mathcal{M} . After a steep elevation to $\mathcal{M} = 2.5$ the forcing routines keep the solvers from decaying by perpetually injecting small amounts of kinetic energy. Taking a closer look (zoomed picture) a distinct saw-tooth profile appears.

4.2.2 Column Density & Velocity

Fig. 21 to fig. 23 show the column Mach number and the column density of all eight conducted runs after four crossing times when the forcing is stopped and the phase of turbulent decay begins. At this point in time all simulations are expected to show a fully developed isotropic supersonic turbulence with a variety of large and small scale features as well an established energy cascade.

In fig. 21 the three solvers from FLASH are grouped together in one page. Obviously, they fulfill the expectations and serve as reference for the solutions brought up by FLEXI.

First of all, the solutions from Euler FV and the RK3 schemes resemble an isotropic supersonic turbulence as well, while the Midpoints seem to differ considerably. A cascade from large scale structures down to smaller scales is visible. However, there are some problems resolving structures on smallest scales. The solutions appear smoother than in fig. 21. In contrast to the rest, Midpoint FV (fig. 22) has a very distinct feature with a large blob of high mass concentration and contiguous regions of void swept empty by a strong velocity field. Apparently, the large scale modes of the driving force field (cf. sec. 3.2) at that time drags the majority of the medium into one big lump.

The solutions during the decay phase at $t_d = 5$ (fig. 24, fig. 25 and fig. 26) look much more alike. Most strikingly, Euler FV and both RK3 schemes have the most energy left in the system proofed by the color intensity of the Mach number plots. All density plots reveal an isotropic turbulence with large and small scale features. As mentioned before, FLEXI's solvers again show fewer features at smallest scales compared to FLASH.

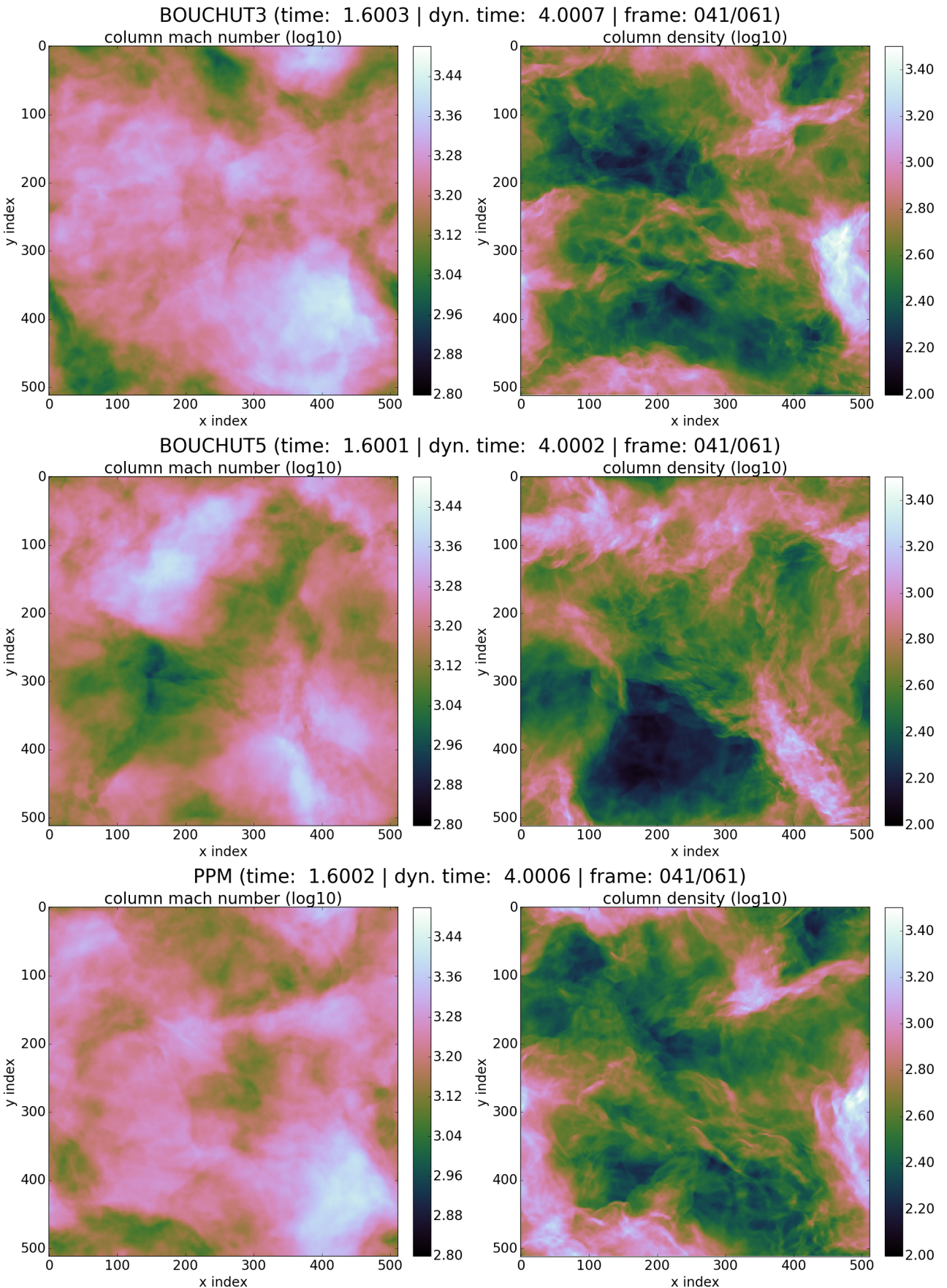


Figure 21: Turbulent phase: Column Sonic Mach Number and column density along z-axis at the time when forcing is stopped: $t_d = 4.0$.

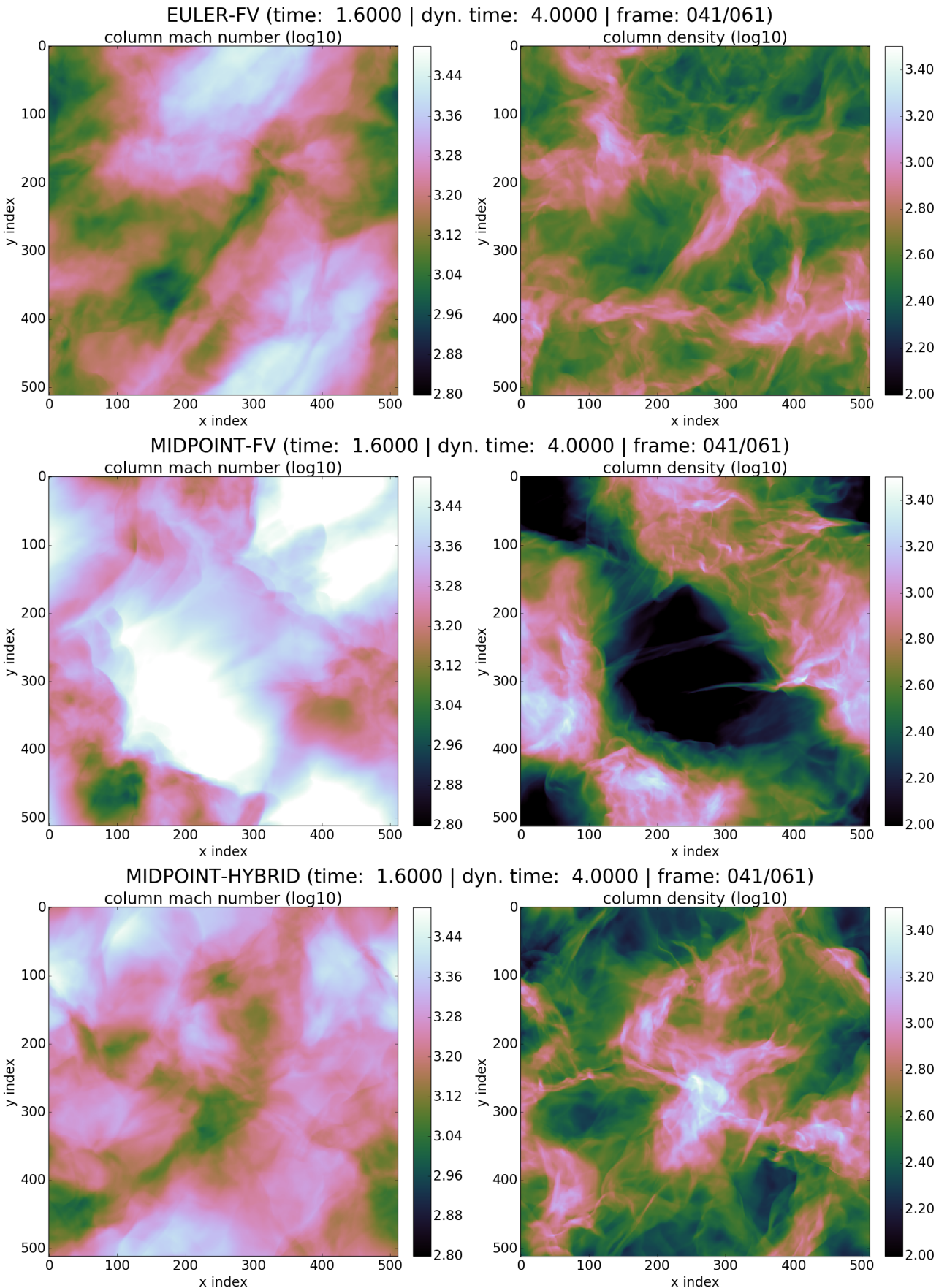


Figure 22: Turbulent Phase: Column Sonic Mach Number and column density along z-axis at the time when forcing is stopped: $t_d = 4.0$.

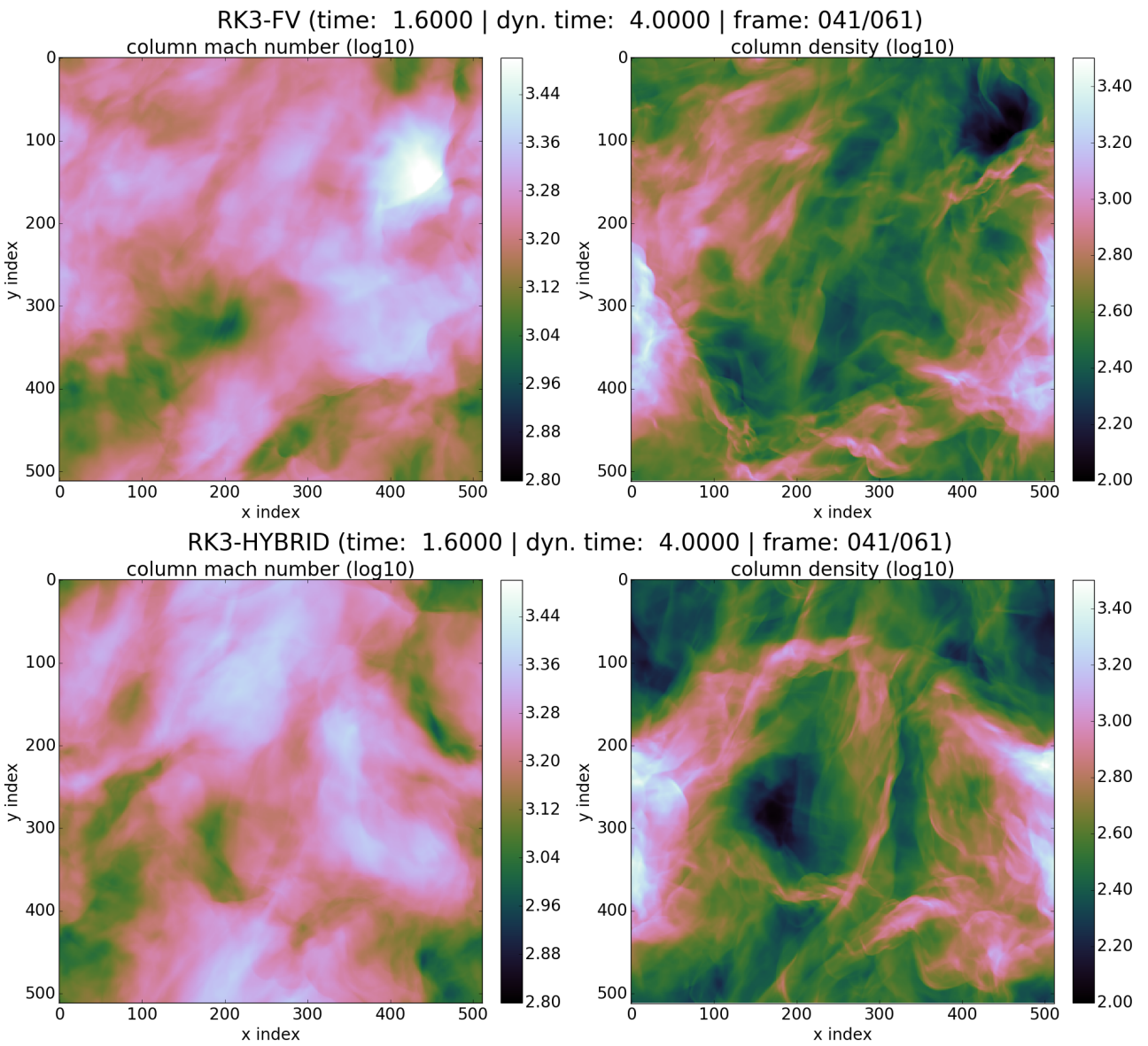


Figure 23: Turbulent Phase: Column Sonic Mach Number and column density along z-axis at the time when forcing is stopped: $t_d = 4.0$.

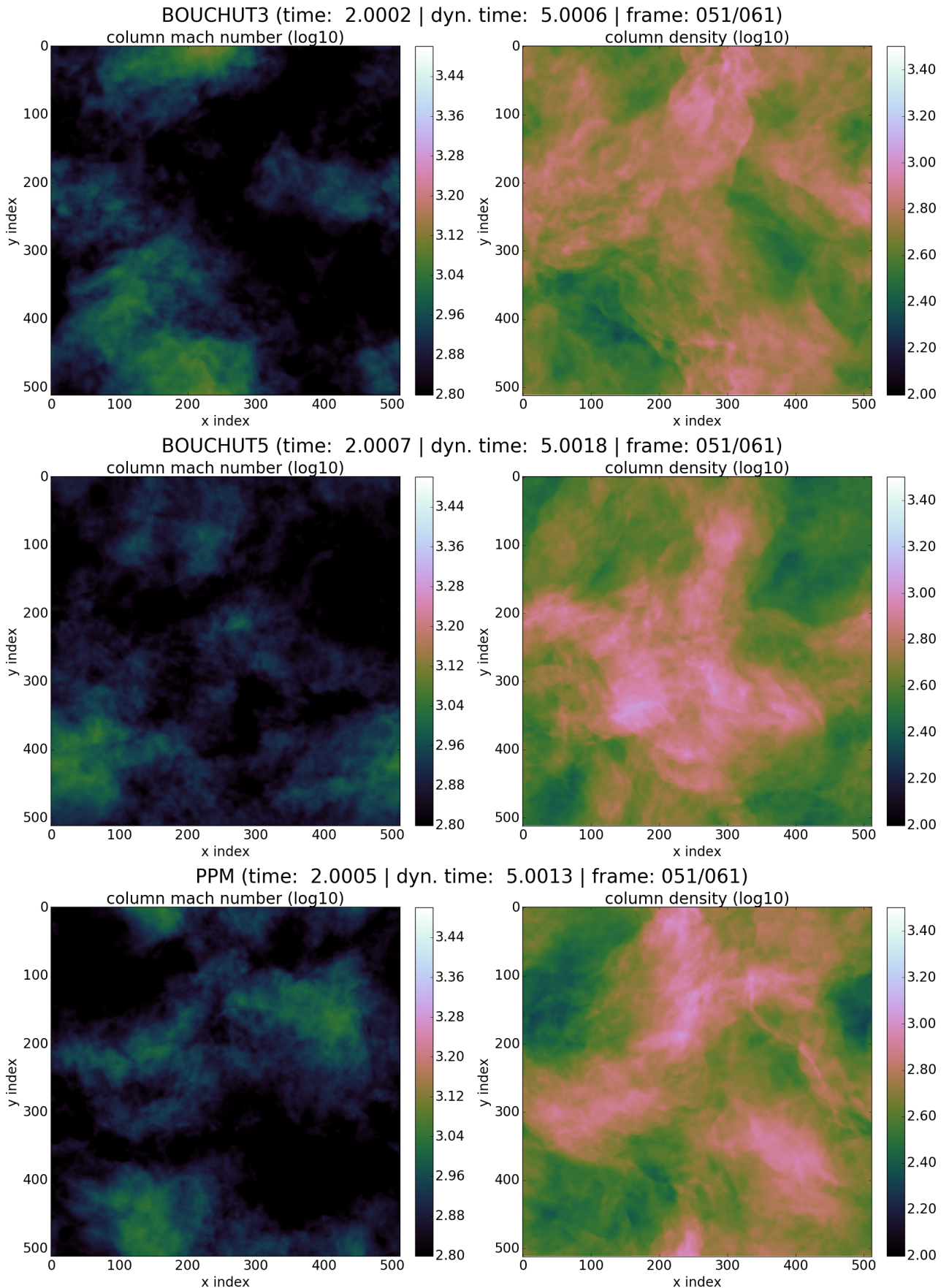


Figure 24: Decay phase: Column Sonic Mach Number and column density along z-axis during decay phase: $t_d = 5.0$.

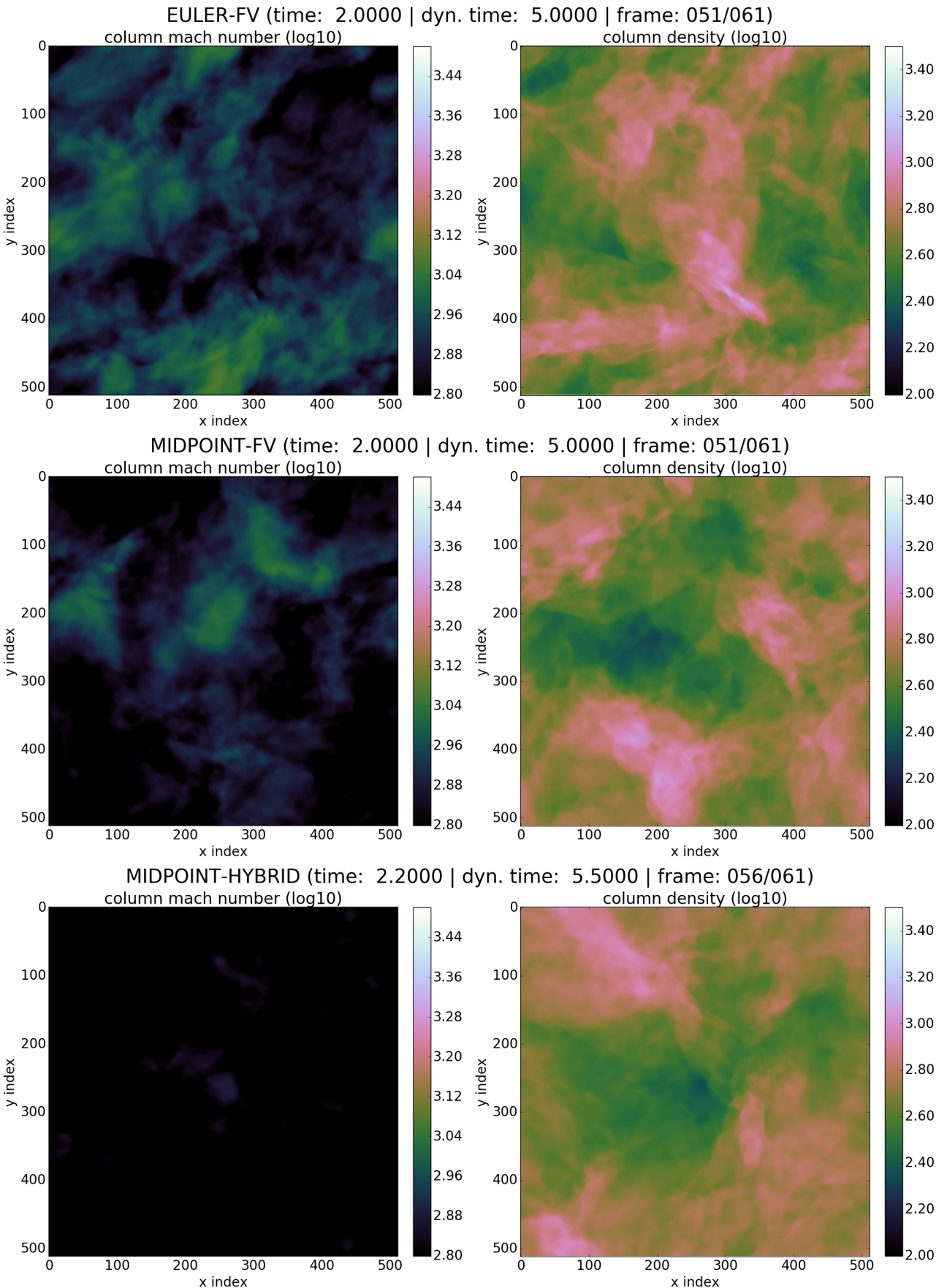


Figure 25: Decay phase: Column Sonic Mach Number and column density along z-axis during decay phase: $t_d = 5.0$.

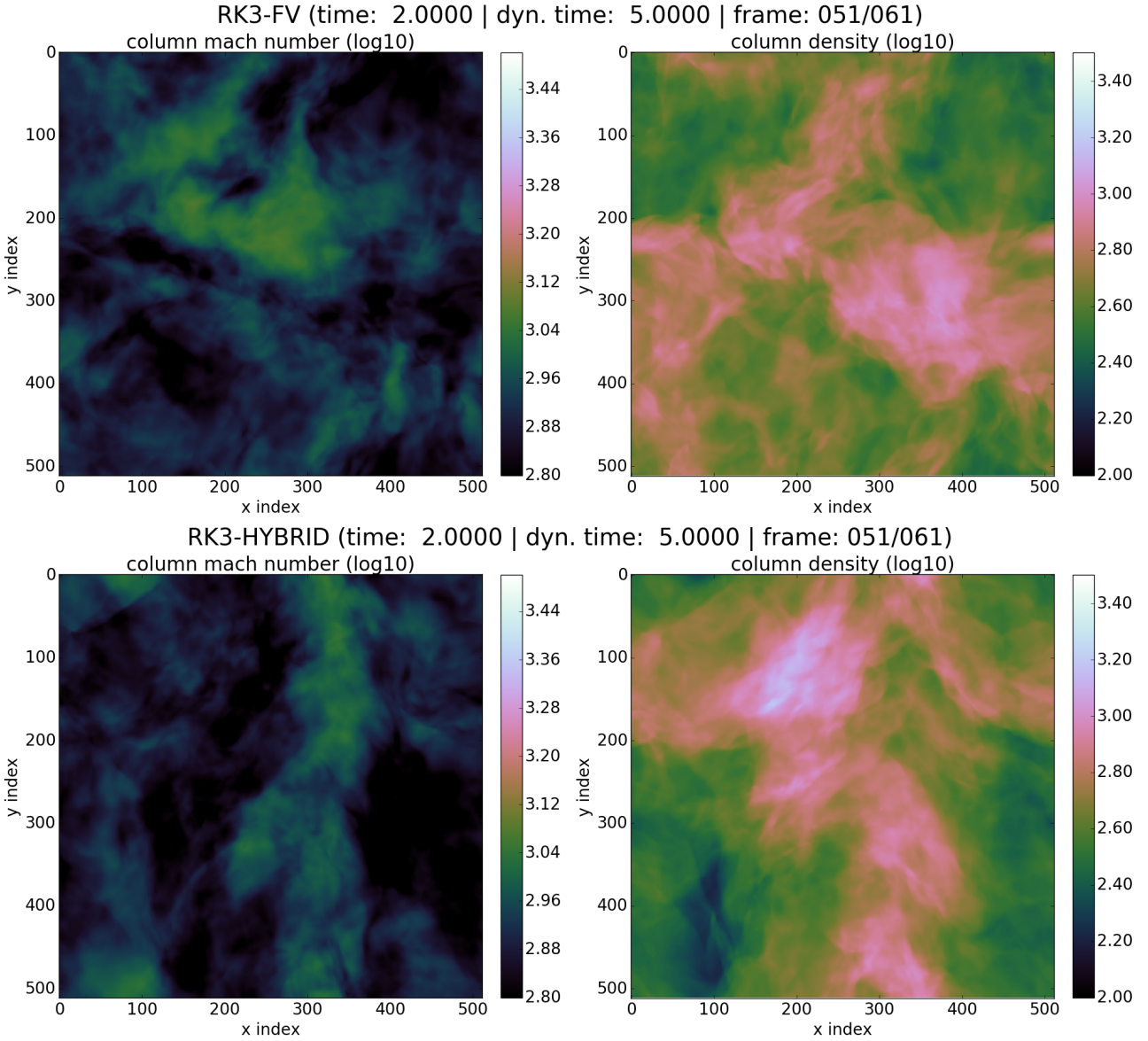


Figure 26: Decay phase: Column Sonic Mach Number and column density along z-axis during decay phase: $t_d = 5.0$.

4.2.3 FV-DG Mode Switching

Two of the conducted runs are hybrid schemes, where shock capturing routines decide, when a DG element must switch to FV mode in order to handle a strong shock condition correctly. Sec. 3.3 describes the procedure in detail. Fig. 27 shows the relative amount of FV elements over dynamic time. Similar to the Mach number plot (fig. 20), the three stages of turbulence are reflected in this plot. Initially, all elements are in DG mode. During the stir-up phase the FV elements quickly dominate and settle down on a range between 65% and 75%. After four crossing times, when forcing is stopped, the overall shock situation in the turbulence is relieved and fewer FV elements are needed. It finally reaches a balance of 50-50. If the simulation would go on, the amount of FV elements is expected to eventually fall down to 0%.

The mode switching routines follow the Mach number with some latency. This make sense since the amount of FV elements are kind of an indicator for the intensity of the turbulence, which inherently responds slowly to external changes. Consequently, even after stopping the

driver at $t_d = 4$, it takes at least half the crossing time till the ratio starts to noticeably decline.

Having only around 25% DG elements (most of the time) means their influence on the performance of the hybrid scheme is expected to be rather small. Nevertheless, fig. 27 proofs that the mode switching code operates as expected. Increasing the spatial resolution should yield better ratios in favor of DG elements. The method is a proof-of-concept with lots of room for improvement.

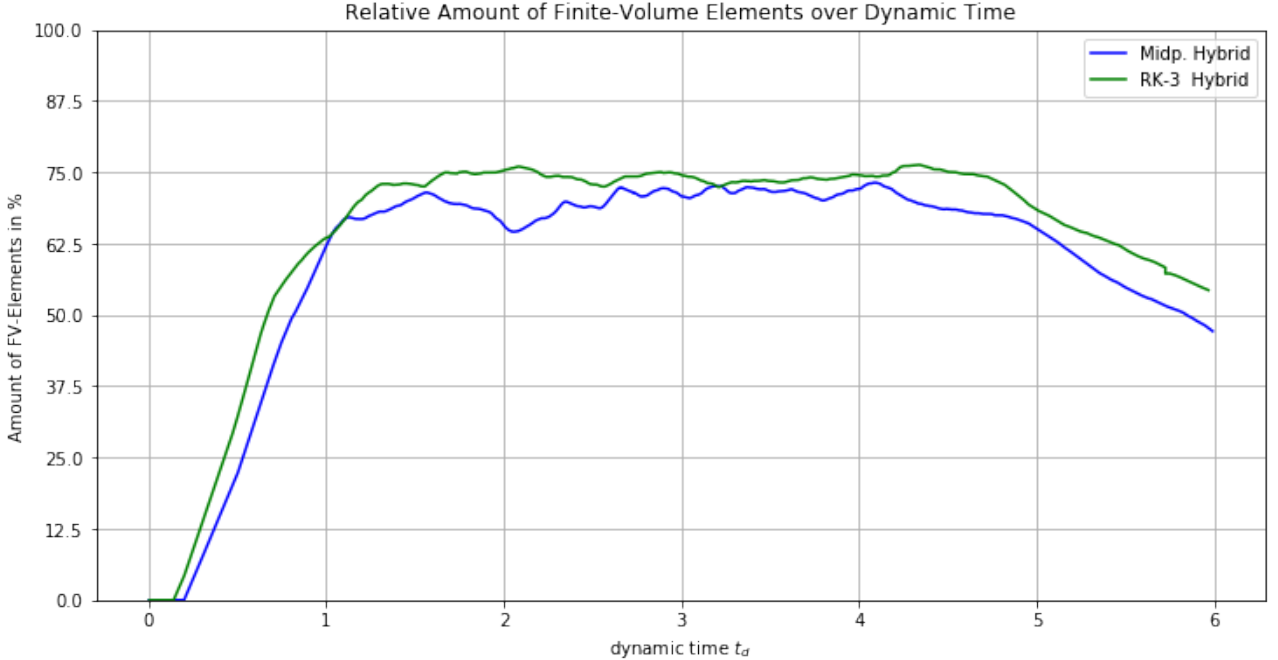


Figure 27: Time evolution of the ratio of Finite-Volume Elements to the total number of elements. The mode switching works both ways, otherwise the plots would reach 100%. At $t_d = 4$ the driving stops and the amount of FV elements declines. *Remark* The other solvers would stay at 100% since they operate with Finite-Volumes only.

4.2.4 Energy Dissipation

In order to keep the temperature constant, polytropic cooling deprives the exact amount energy, which got transferred from kinetic energy to internal energy. The physical mechanics behind this have been explained in sec. 2.2/Energy Cascade.

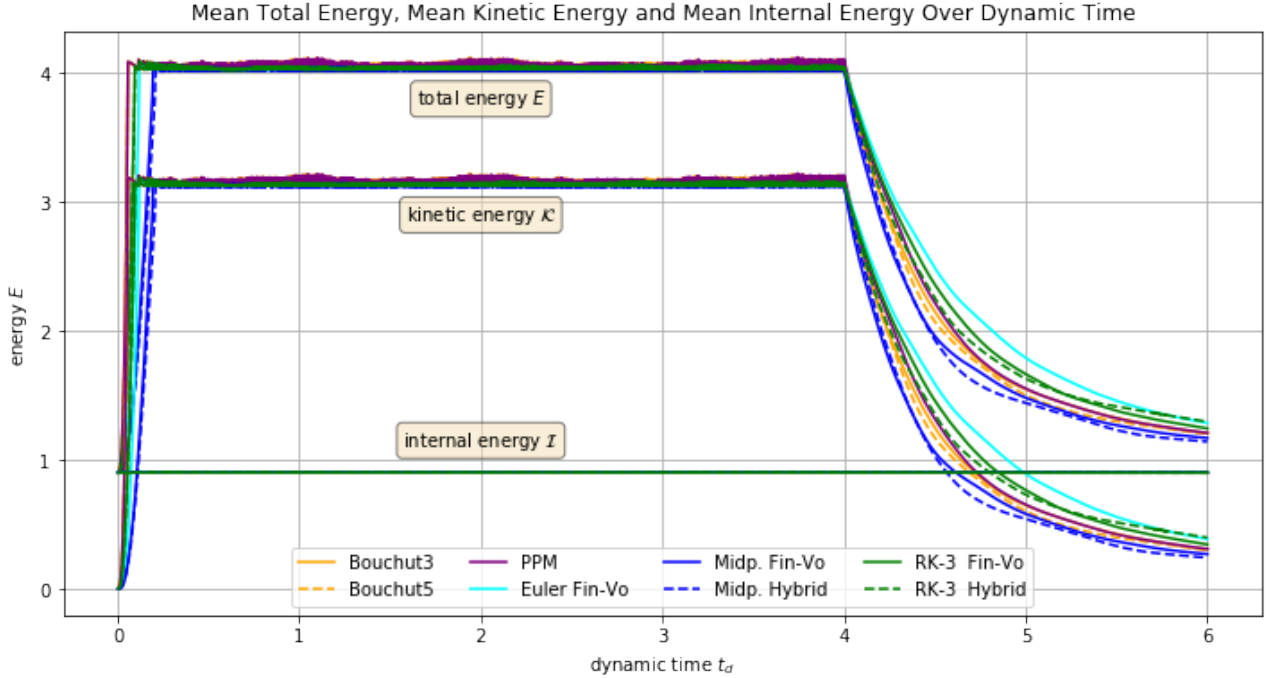


Figure 28: Time evolution of the energy in the system. The total energy E is the sum of the kinetic \mathcal{K} and internal energy \mathcal{I} : $E = \mathcal{I} + \mathcal{K}$. The internal energy is held constant via polytropic cooling (cf. sec. 3.1).

Now we are interested in how much kinetic energy is actually dissipated within a certain amount of time. A naive approach would be to take the numerical time derivative of the evolving kinetic energy (fig. 29). But it would just yield sensible results for the decaying phase. Instead the energy loss right before and after polytropic cooling is recorded and divided by the current timestep. The resulting plot is shown in fig. 29. The rate of internal energy deprivation is equivalent to the rate of kinetic energy dissipation, since their is only one energy source coming from turbulent forcing and one energy sink via cooling. During the transition from the initially constant state to turbulent state ($t_d \approx [0, 0.3]$) the dissipation rate increases rapidly and settles down to a mean rate of around $\langle -\frac{\mathcal{K}}{dt_d} \rangle = 6.5$ energy units per dynamic timestep. While most solvers follow a similar pattern up to 1.5 crossing times, a change of quality seams to appear. This observation becomes even more clear in fig. 32. The conducted runs part into two groups. The first group contains the Euler FV and both RK3 solvers. They show a balanced profile and happen to be the least dissipative ones. The second group, PPM and both Midpoints plus both Bouchuts, jump up and down in a incoherent manner. Especially, the Midpoint solvers give rise to huge excesses, which also reflect in the cumulative energy accounting shown in fig. 30. Furthermore, it seems that the situation would have gotten worse if the solvers would not have started to settle down due to driving stop at $t_d = 4$. During the decay phase the variations in dissipation rates are much smaller than before and even turn upside down at $t_d \approx 4.4$. An explanation of what causes the high pitched energy dissipation rates for the Midpoint methods is further investigated in the next sections.

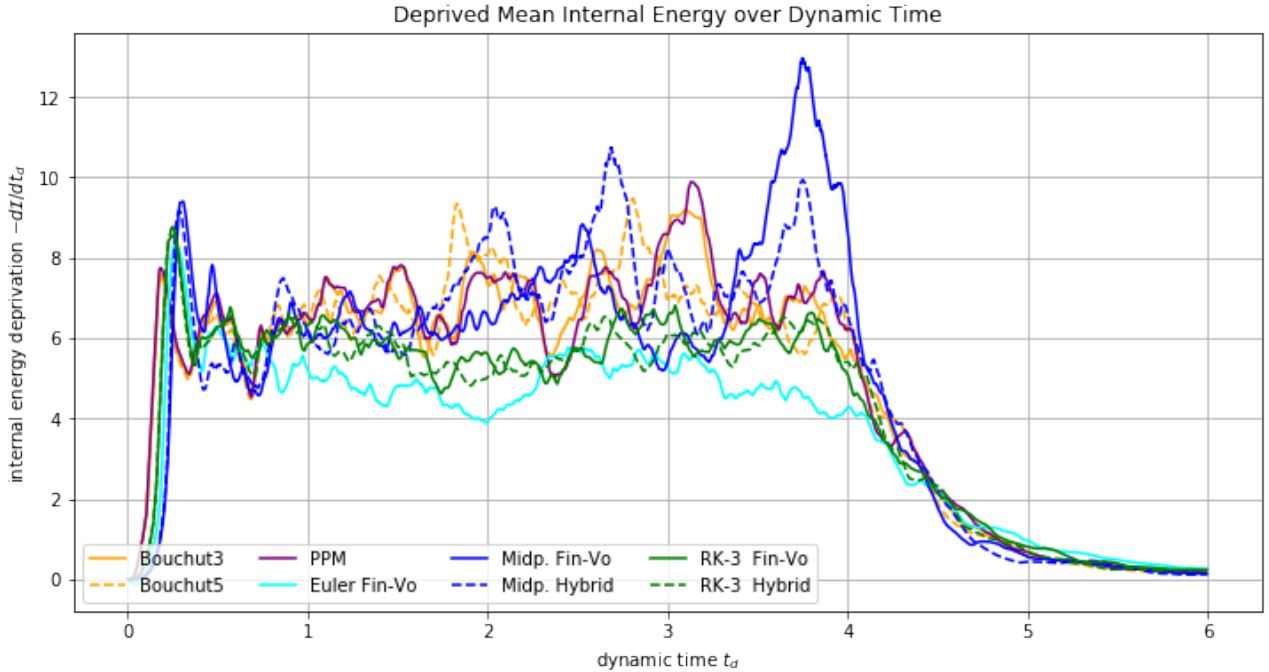


Figure 29: Time evolution of the internal energy deprivation by measuring the energy loss right before and after polytropic cooling and dividing by the current dynamic timestep.

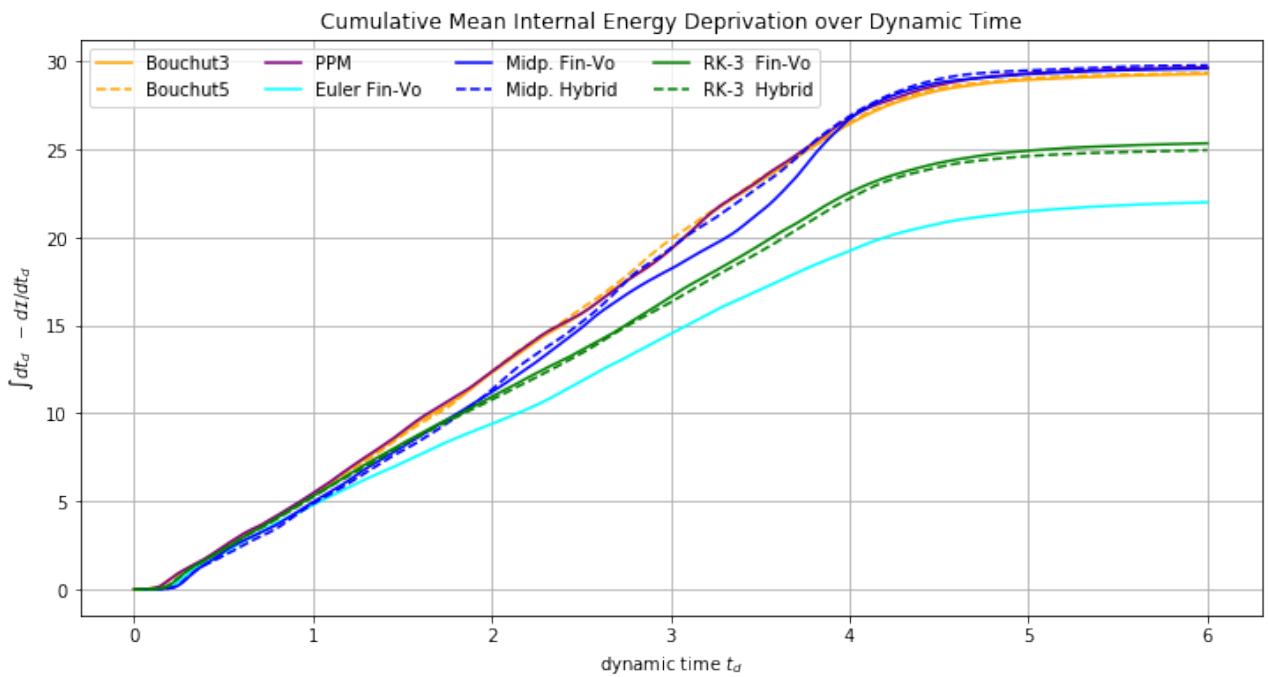


Figure 30: Cumulated energy deprivation collected by the polytropic cooling module. The plots represent the numerical integration (trapezoid rule) of the energy deprivation rates in fig. 29. By the end of the simulation circa 10 times the average energy (cf. fig. 28) was pumped through the system.

4.2.5 Density & Velocity Distributions

Density Distribution Fully developed supersonic turbulences are expected to reveal a normal density distribution (cf. sec. 2.2.2). Additionally, it gives an insight into the distribution of mass from smallest to largest scales. All log-log. scale density PDFs in fig. 31 show good indications for the presence of turbulence. The dotted lines are log-normal fits of eqn. 56 in sec. 2.2.2. The notorious underestimation of the fits on large scales is caused by the under-resolvment of the setup. While during the turbulent phase ($t_d = [2, 4]$) the solvers from FLASH have considerably more mass on small scales, this is not the case anymore during the decay phase; exemplified by $t_d = 4.7$ and $t_d = 6.0$.

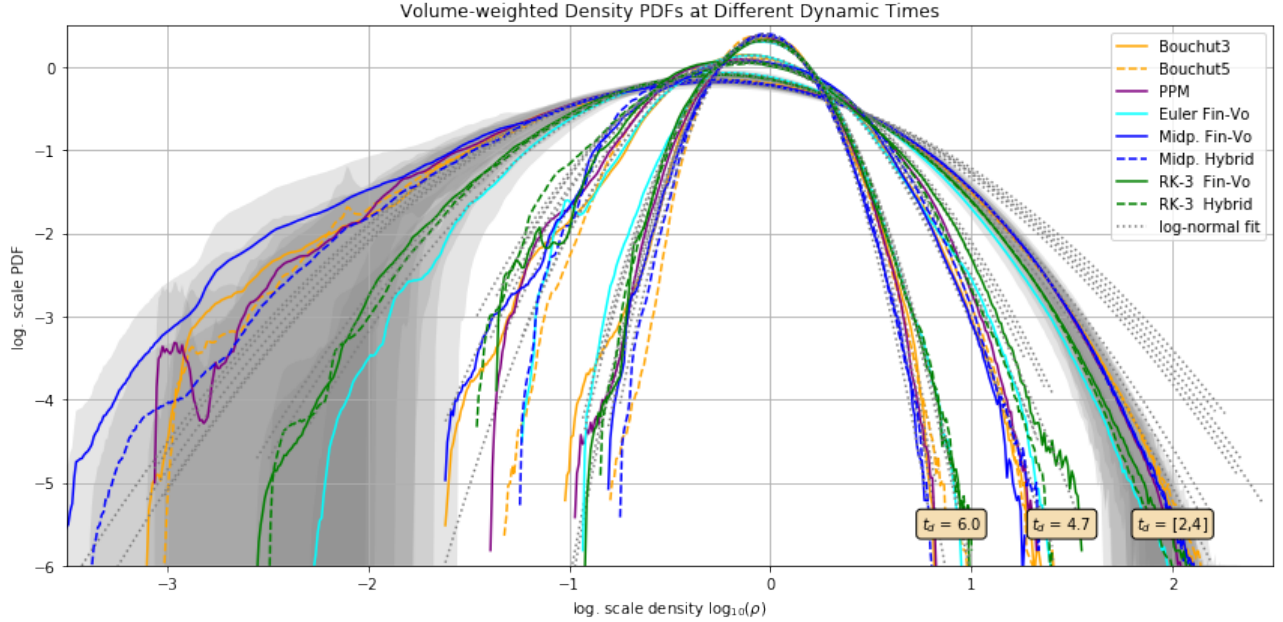


Figure 31: Log-log. scale volume-weighted density PDFs for the turbulent phase $t_d = [2, 4]$ (time-average) and two stages of the decaying phase: $t_d = 4.7$ and $t_d = 6.0$. The faint grey area marks the margin of error of the time-averaging. As the decay progresses, the width of the distributions decrease and the mean values return to the initial density: $\log_{10}(\rho_0) = \log_{10}(1) = 0$. The log-normal fit (dotted lines) were done with eqn. 58.

The width σ_s of the density distribution in fig. 31 are related to the sonic Mach number of the system (cf. sec. 2.2.2). Applying eqn. 58 and eqn. 59, where

$$b = 1 + (D^{-1} - 1) \zeta = 1 + (3^{-1} - 1) 0.5 = 2/3, \quad (98)$$

we can recover the Mach number of the turbulence. The result is shown in fig. 32. The plot is similar in shape to the energy dissipation in fig. 29. After two crossing times a change of quality seems to happen for some of the solvers, accompanied by a lot of noise over time but better reconstruction of the reference sonic Mach number of $\mathcal{M} = 2.5$. Again the Midpoint FV has a huge spike near the end of the turbulent phase ($t_d = 4$), which we will take a closer look at further down. Euler FV and both RK3 schemes severely underestimate the Mach number by 20%. During the decay phase all fits yield smaller values. It might be the case that in this phase the relation in eqn. 58 breaks down. Table 5 lists the fitting results of the time-averaged turbulent phase from 2 to 4 crossing times, where the results seem most promising.

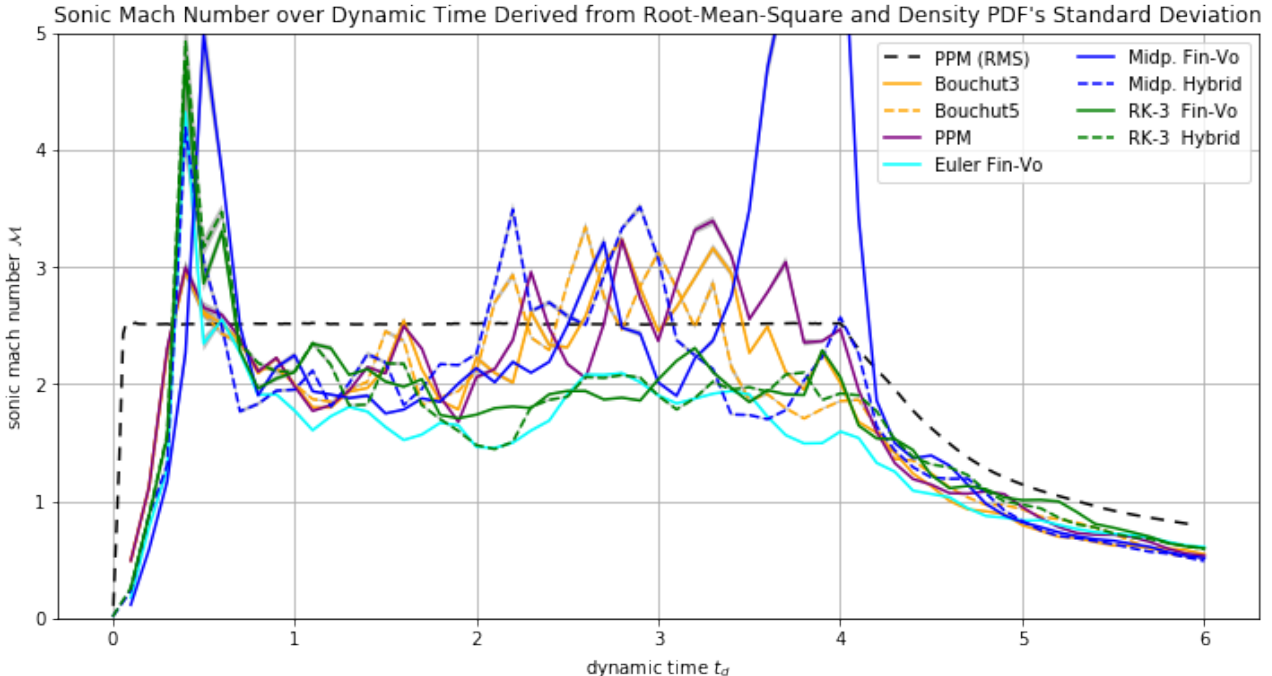


Figure 32: Time evolution of the sonic mach number over time derived from the width of the volume-weighted density PDFs via relation eqn. 58 ($b = 2/3$). The dashed line represents the root-mean-square velocity of the PPM solver and serves as a reference. Due to the log-normal relationship, each individual fit yields very low error margins. Hence, the error bars are to small to see.

Table 5: Comparison of Gaussian Fitting Results of the Log-normal Density PDF averaged over the turbulent phase: $t_d = [2, 4]$. See relation eqn. 58. $b = 2/3$. The PDF Mach number \mathcal{M}_{PDF} of the Midpoint FV overshoots due to the influence of the runaway. Compare fig. 32.

Solver	Mean s_0	Std. Deviation σ_s	RMS Mach \mathcal{M}_{RMS}	PDF Mach \mathcal{M}_{PDF}
Bouchut3	-0.31 ± 0.05	0.58 ± 0.06	2.63 ± 0.13	2.5 ± 0.4
Bouchut5	-0.29 ± 0.06	0.57 ± 0.08	2.59 ± 0.09	2.4 ± 0.6
PPM	-0.32 ± 0.05	0.59 ± 0.06	2.62 ± 0.12	2.6 ± 0.5
Euler Fin-Vo.	-0.24 ± 0.03	0.47 ± 0.04	2.56 ± 0.04	1.8 ± 0.2
Midp. Fin-Vo.	-0.31 ± 0.04	0.60 ± 0.09	2.80 ± 0.40	2.7 ± 0.8
Midp. Hybrid	-0.32 ± 0.05	0.56 ± 0.07	2.81 ± 0.18	2.4 ± 0.5
RK-3 Fin-Vo.	-0.26 ± 0.02	0.50 ± 0.03	2.61 ± 0.06	2.0 ± 0.2
RK-3 Hybrid	-0.26 ± 0.03	0.48 ± 0.04	2.55 ± 0.04	1.9 ± 0.3

Velocity Distribution An exceeding dispersion of velocity PDFs indicates strong bulk motions within the medium. Bulk motion (cf. sec. 2.2) distorts the turbulence by drawing off kinetic energy from the turbulence, while at the same time the root-mean-square velocity of the system remains constant. In the worst case the energy cascade breaks down or does not even develop in the first place. Fig. 33 lacks any considerable dispersion, which means the bulk motion correction (cf. sec. 3.1) is working correctly. More distinctive is the bulge of high velocities, brought out by the Midpoint schemes, accompanied by huge error margins. This means that during the turbulent phase there must be extreme velocity fluctuations up to Mach 30 and beyond. Fig. 34 affirms this observation. Comparing this plot with the energy dissipation rates in fig. 29, there is a correlation between maximum velocity bursts and high pitched dissipation. Obviously, this applies only to the Midpoint schemes. The maximum velocity plot indicates only a singular value, which does not necessarily represents a prevalent phenomenon in the

system. In conjunction with the velocity PDF however, this can be considered true for the Midpoint schemes.

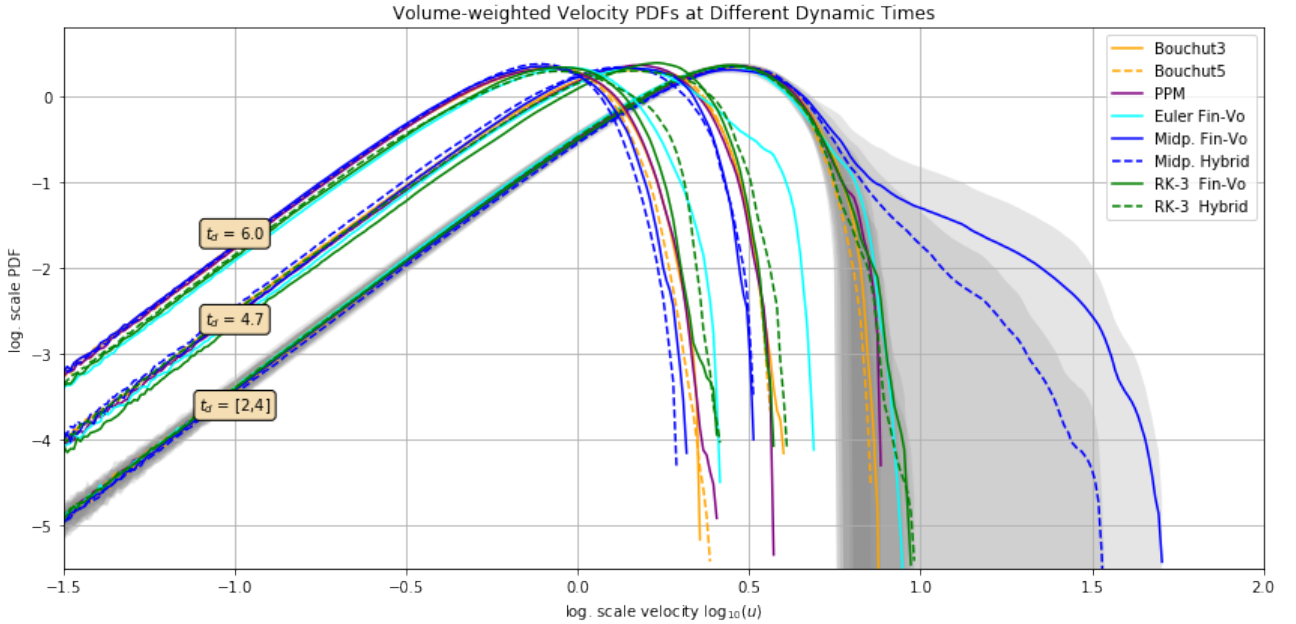


Figure 33: Volume-weighted velocity PDFs computed from the checkpoint files for the turbulent phase $t_d = [2, 4]$ (time-average) and two stages of the decaying phase: $t_d = 4.7$ and $t_d = 6.0$. The faint grey area marks the margin of error of the time-averaging. The Midpoint schemes yield strong fluctuation of high velocities during the turbulent phase (cf. fig. 34).

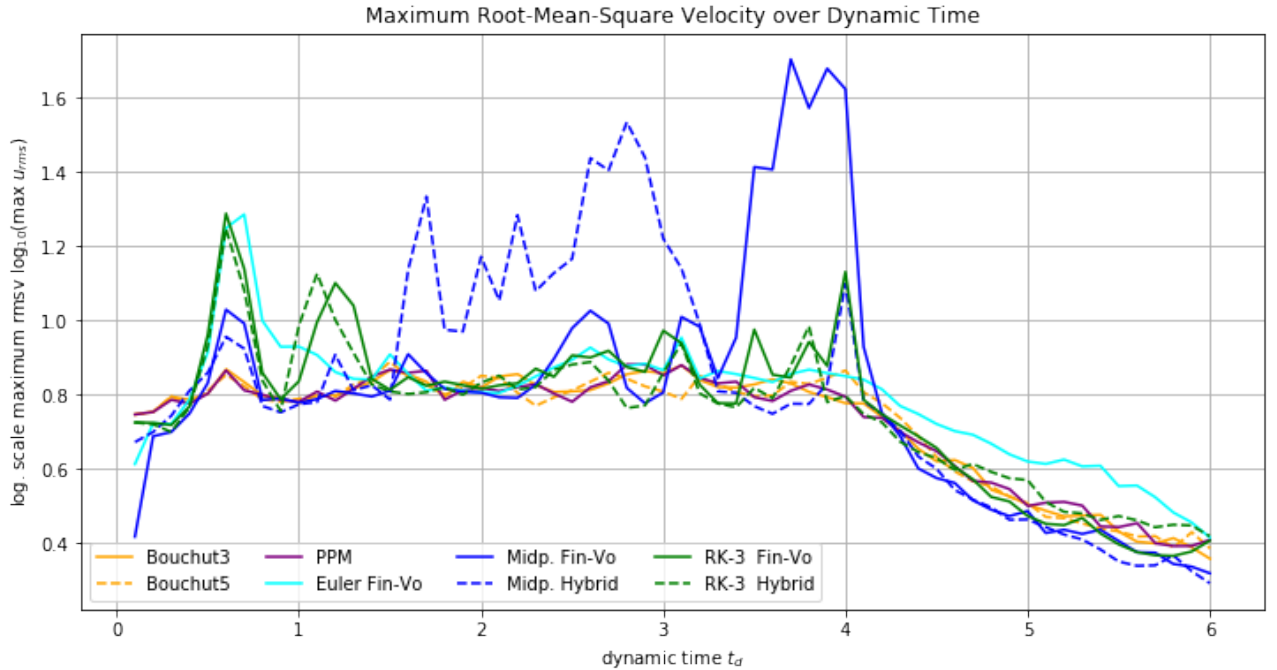


Figure 34: Maximum root-mean-square velocity over time retrieved from the checkpoint files. The Midpoint schemes show very strong maximum velocity bursts up to Mach 30 and beyond during the turbulent phase.

As already discussed under sec. 4.2.2, the Midpoint FV method shows a unique pattern of slow-moving mass lumps and regions of highly accelerated but very thin gas. When mass-weighting

the velocity distribution, see fig. 35, we get another picture. The bulge on the right side of fig. 33 completely disappears, which supports the observation of highly accelerated thin gas in the Midpoint FV run. By contrast, Bouchut 3, Bouchut 5 and PPM show a richer structure in the slow moving range.

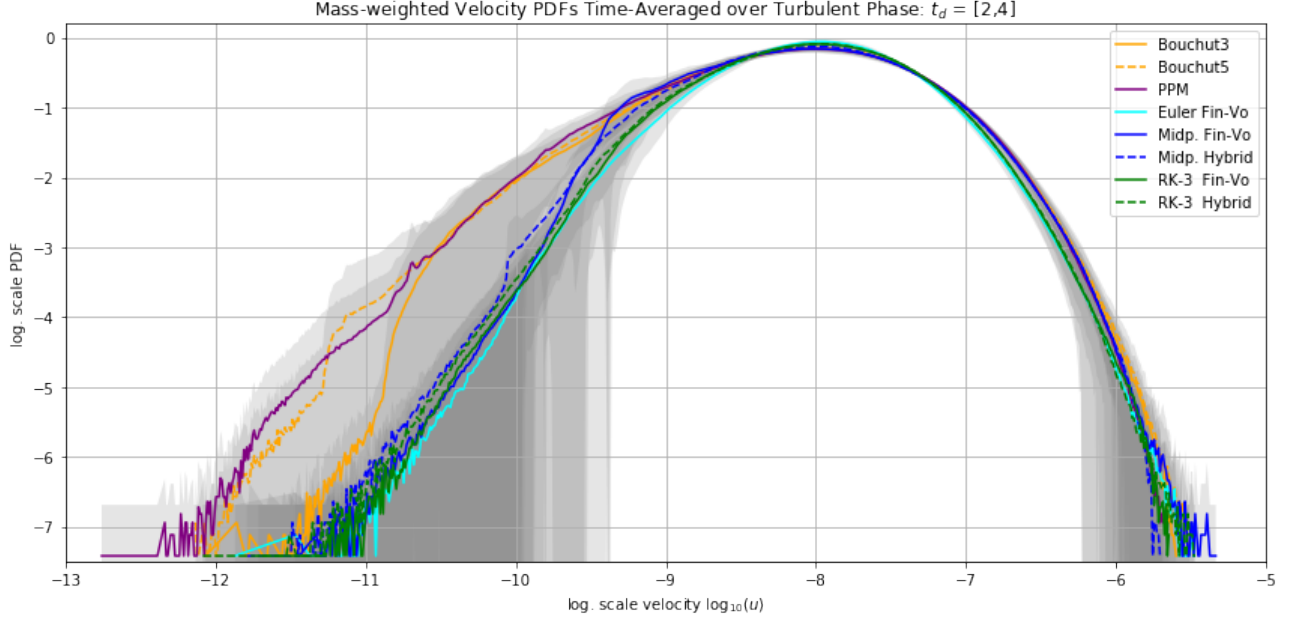


Figure 35: Log-log. scale mass-weighted velocity PDF time-averaged over the turbulent phase ($t_d = [2, 4]$). The gray areas mark the margin of error. The solvers from FLASH have a greater amount of slowly moving mass than the others. The bulge on the right side in fig. 33 is gone due to fewer mass in the high-velocity range.

4.2.6 Energy & Velocity Powerspectra

Powerspectra give an insight into the distribution of a physical quantity from large to small length scales. In this section we discuss the energy and velocity powerspectra, which were introduced in sec. 2.2.1. The powerspectrum is divided into three ranges. In the driving or large scale range the energy injection from the turbulent driver takes place. It spans over the first three to four modes. From there the energy trickles down to smaller and smaller scales, called energy cascade, which takes place in the inertial range. Finally it reaches the dissipative range which begins in our case at roughly $k_{diss} \approx 25$. This is where the kinetic energy dissipates and gets transformed into internal energy. In the powerspectrum of the kinetic energy, fig. 36, the boundaries of the mentioned ranges are drawn in. According to Parseval's theorem the normed area under the kinetic energy powerspectrum is equal to the total squared real-valued kinetic energy in the box. (cf. sec. 2.2.1). Table 6 proofs via numerical integration that this is indeed true within the margins of error. In agreement with the discussion of column densities and the density distributions in the previous sections, the solutions provided by FLASH's solvers contain more energy on small scales than those with FLEXI. To quantify this observation the area under the dissipative range was estimated and compared to the total squared kinetic energy. Consulting the right-most column in table 6 the relative amount of energy on small scales ranges from 2.4% (RK3 FV) to 5.7% (Bouchut 5).

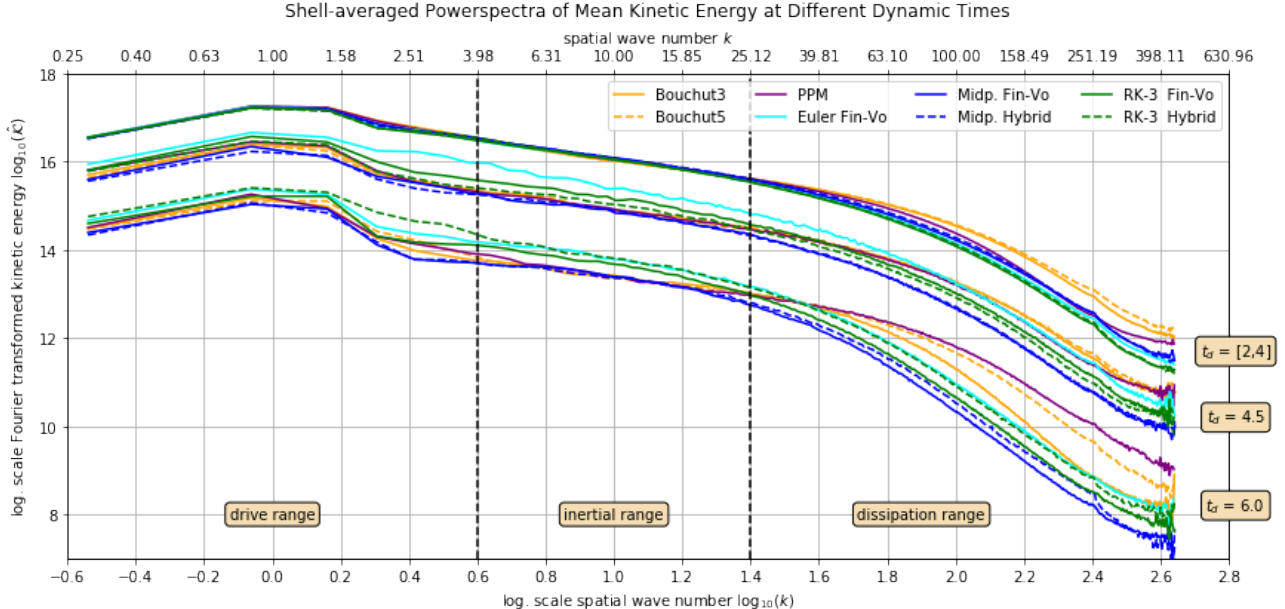


Figure 36: Powerspectra of the volume-weighted mean kinetic energy field shown for the turbulent phase $t_d = [2, 4]$ (time-average) and two stages of the decay phase: $t_d = 4.5$ and $t_d = 6.0$. When the total kinetic energy declines, the powerspectrum shifts downwards. The inertial range starts at $k = 4$ since forcing is applied on $k_{drive} = 1, 2, 3$. The beginning of the dissipative range is estimated to $k_{diss} \approx 25$ when the spectra start the bend down. The study in [22] came to the same conclusion for equal grid resolution of 512^3 .

Besides the log-normality of the density PDF (sec. 4.2.5) the slopes of the inertial range of velocity powerspectra are well-established indicators for the correct modelling of turbulences. According to the theory (cf. sec. 2.2.1) we expect slopes of $m_{vw} = -2.1$ and $m_{mw} = -1.6667$ for the volume-weighted and mass-weighted powerspectra of the velocity field, respectively. Fig. 37 and fig. 38 indeed reproduce given slopes for the time-averaged powerspectrum of the turbulent phase. The spectra at the end of the simulation, when the turbulent decay progressed considerably, are plotted as well. Obviously, the inertial range has leveled down. This makes sense, considering the fact that the supply of kinetic energy was cut off. Hence, the large scale structures gradually dissolve and push their energy down the cascade. The change of slope can be seen in fig. 39 very clearly. In the beginning the inertial range is very steep. The turbulent driver is pumping energy into the system on first three modes. As the simulation continues the energy cascade builds up and is fully established after two crossing times. When entering the decay phase ($t_d = 4$), the slope flattens out. Table 6 lists the results of the linear fits of the inertial range as well as the numerically integrated areas under the time-averaged powerspectra of the turbulent phase.

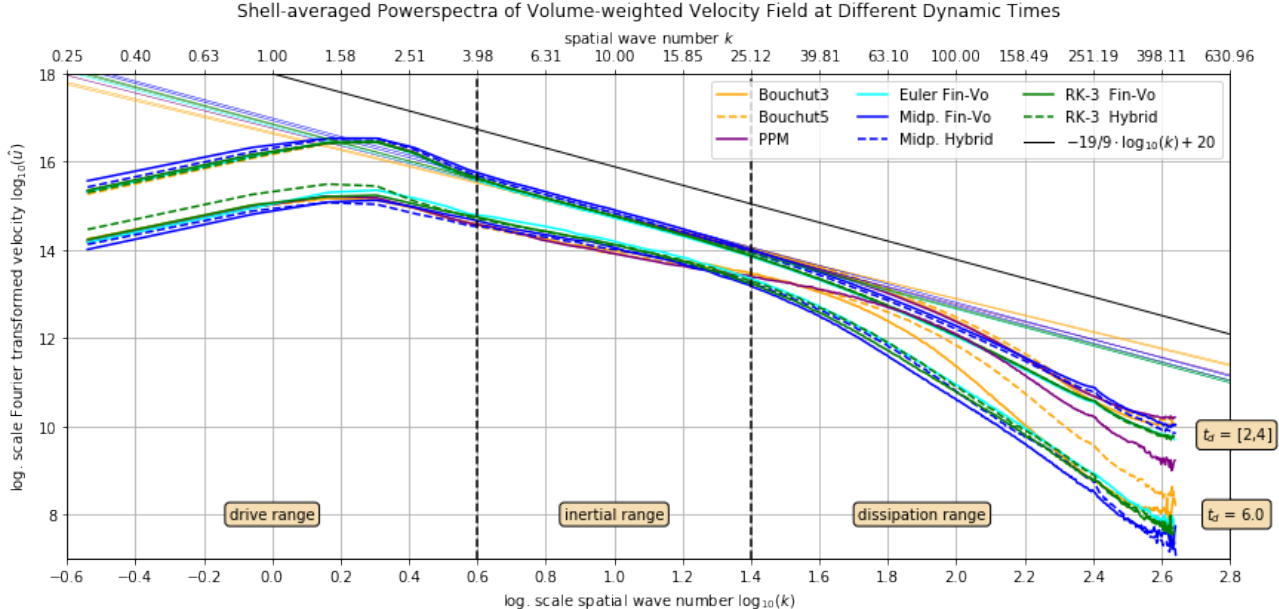


Figure 37: Powerspectra of the volume-weighted velocity field for the turbulent phase $t_d = [2, 4]$ (time-average) and at the end of the decaying phase $t_d = 6.0$. The inertial range starts at $k = 4$ since forcing is applied on $k_{drive} = 1, 2, 3$. The black solid line marks the expected slope $m_{vw} = -19/9$ (cf. sec. 2.2.1). In agreement with [22] (resolution: 512^3), the beginning of the dissipative range is estimated to $k_{diss} \approx 25$, where the spectra start the bend down.

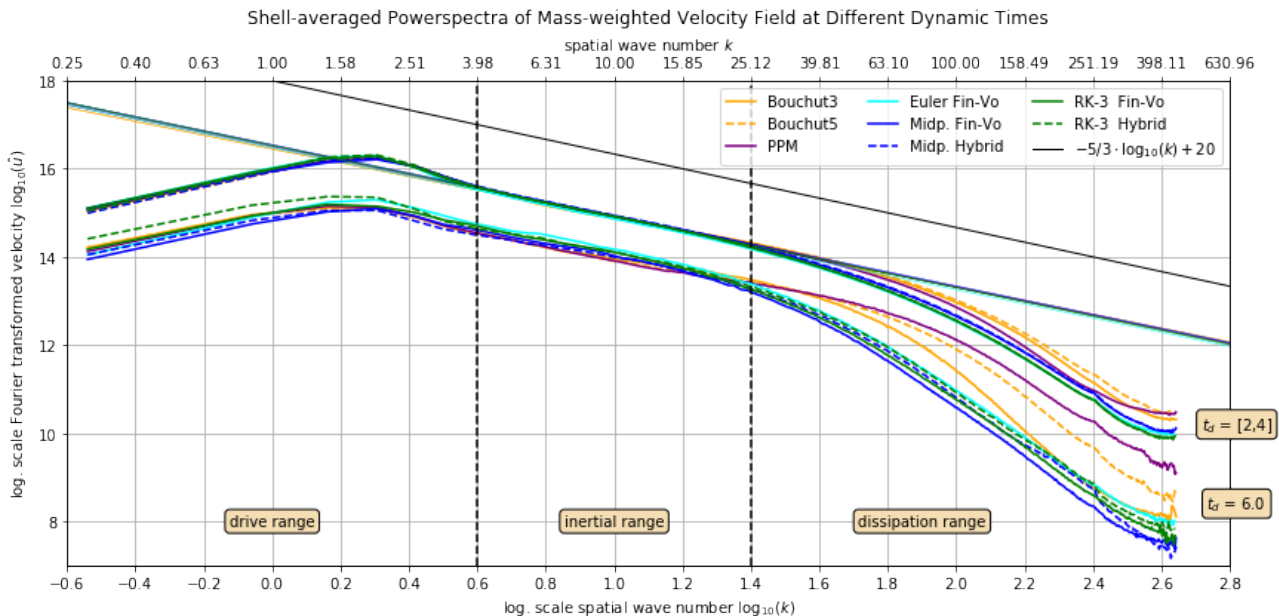


Figure 38: Powerspectra of the mass-weighted velocity field for the turbulent phase $t_d = [2, 4]$ (time-average) and at the end of the decaying phase $t_d = 6.0$. The black solid line marks the expected slope $m_{vw} = -5/3$ (cf. sec. 2.2.1). In agreement with [22] (resolution: 512^3), the beginning of the dissipative range is estimated to $k_{diss} \approx 25$, where the spectra start the bend down.

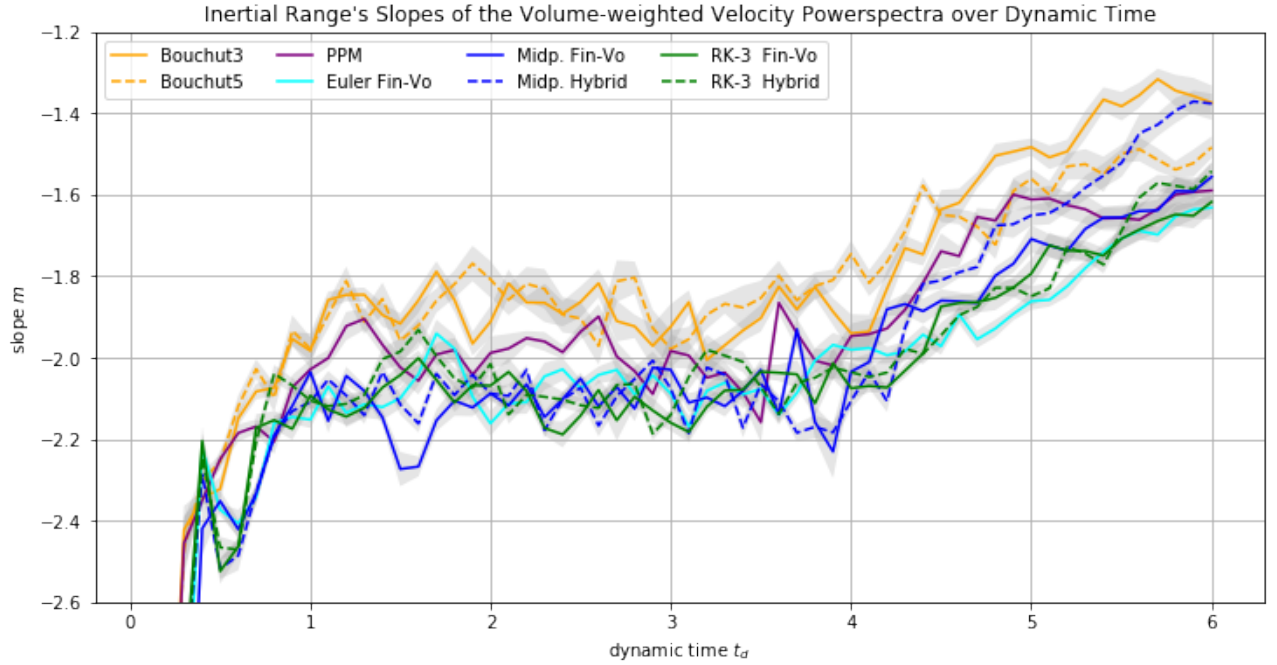


Figure 39: Time evolution of the inertial range's slope of the volume-weighted velocity powerspectra. See fig. 37.

Table 6: Comparison of the three types of powerspectra averaged over the turbulent phase: $t_d = [2, 4]$

Solver	Slope m	Offset n	Mean Squ. $\langle \cdot^2 \rangle$	Area A	Diss. Area A_{diss}	$A_{diss}/A [\%]$
Volume-weighted Mean Kinetic Energy						
Bouchut3	-1.16 ± 0.05	17.19 ± 0.24	39 ± 4	37 ± 8	2.00 ± 0.60	5.4 ± 1.7
Bouchut5	-1.19 ± 0.10	17.22 ± 0.30	40 ± 5	37 ± 8	2.10 ± 0.70	5.7 ± 1.8
PPM	-1.14 ± 0.07	17.19 ± 0.24	38 ± 4	36 ± 8	1.37 ± 0.33	3.8 ± 0.9
Euler Fin-Vo.	-1.06 ± 0.04	17.11 ± 0.30	35 ± 5	34 ± 9	0.88 ± 0.35	2.6 ± 1.0
Midp. Fin-Vo.	-1.10 ± 0.05	17.18 ± 0.27	37 ± 6	35 ± 9	1.00 ± 0.50	3.0 ± 1.3
Midp. Hybrid	-1.06 ± 0.02	17.15 ± 0.17	36 ± 4	34 ± 7	1.12 ± 0.33	3.3 ± 1.0
RK-3 Fin-Vo.	-1.07 ± 0.08	17.12 ± 0.31	33 ± 4	32 ± 8	0.75 ± 0.28	2.4 ± 0.9
RK-3 Hybrid	-1.17 ± 0.17	17.23 ± 0.34	33 ± 3	32 ± 6	0.81 ± 0.25	2.5 ± 0.8
Volume-weighted Velocity						
Bouchut3	-1.89 ± 0.13	16.67 ± 0.28	4.00 ± 0.40	4.0 ± 0.9	0.0152 ± 0.0034	0.38 ± 0.09
Bouchut5	-1.87 ± 0.11	16.63 ± 0.23	3.86 ± 0.26	3.8 ± 0.7	0.0179 ± 0.0035	0.47 ± 0.09
PPM	-2.00 ± 0.15	16.76 ± 0.31	4.00 ± 0.40	4.0 ± 0.9	0.0143 ± 0.0029	0.36 ± 0.07
Euler Fin-Vo.	-2.08 ± 0.10	16.80 ± 0.15	3.86 ± 0.16	3.8 ± 0.6	0.0068 ± 0.0012	0.18 ± 0.03
Midp. Fin-Vo.	-2.09 ± 0.05	17.00 ± 0.70	6.00 ± 4.00	6.0 ± 0.5	0.0150 ± 0.0130	0.24 ± 0.22
Midp. Hybrid	-2.11 ± 0.03	16.94 ± 0.21	4.80 ± 0.90	4.8 ± 1.4	0.0102 ± 0.0030	0.21 ± 0.06
RK-3 Fin-Vo.	-2.10 ± 0.08	16.87 ± 0.16	3.96 ± 0.17	3.9 ± 0.6	0.0074 ± 0.0015	0.19 ± 0.04
RK-3 Hybrid	-2.08 ± 0.04	16.85 ± 0.12	3.79 ± 0.14	3.9 ± 0.6	0.0073 ± 0.0015	0.19 ± 0.04
Mass-weighted Velocity						
Bouchut3	-1.56 ± 0.10	16.45 ± 0.19	3.158 ± 0.021	3.1 ± 0.4	0.054 ± 0.010	1.72 ± 0.33
Bouchut5	-1.57 ± 0.13	16.45 ± 0.22	3.158 ± 0.024	3.1 ± 0.4	0.060 ± 0.011	1.90 ± 0.40
PPM	-1.59 ± 0.07	16.49 ± 0.17	3.166 ± 0.020	3.1 ± 0.5	0.043 ± 0.007	1.38 ± 0.24
Euler Fin-Vo.	-1.61 ± 0.07	16.48 ± 0.15	3.134 ± 0.004	3.1 ± 0.4	0.021 ± 0.004	0.69 ± 0.13
Midp. Fin-Vo.	-1.60 ± 0.04	16.52 ± 0.15	3.128 ± 0.006	3.0 ± 0.4	0.028 ± 0.009	0.93 ± 0.29
Midp. Hybrid	-1.60 ± 0.03	16.55 ± 0.11	3.133 ± 0.006	3.2 ± 0.5	0.029 ± 0.005	0.92 ± 0.17
RK-3 Fin-Vo.	-1.61 ± 0.05	16.52 ± 0.12	3.137 ± 0.011	3.2 ± 0.4	0.022 ± 0.004	0.70 ± 0.13
RK-3 Hybrid	-1.62 ± 0.12	16.54 ± 0.19	3.138 ± 0.008	3.3 ± 0.5	0.022 ± 0.004	0.68 ± 0.13

4.2.7 Summary

In the driven supersonic turbulence setup we analyzed the various solutions of FLASH's and FLEXI's solver over the course of 6 crossing times. All runs consisted of three phases or stages. In the first phase the initially restful medium was stirred up by turbulent forcing to the root-mean-square velocity of $\mathcal{M} = 2.5$. After reaching this limit, the driver kept the kinetic energy stable for 4 crossing times so that a turbulent energy cascade develops. After the turbulent phase, forcing was deactivated and the turbulence decayed for another 2 crossing times.

By analyzing density/velocity distributions and powerspectra it was confirmed that all solvers modeled a supersonic turbulence correctly. They confirmed a log-normal density profile and their inertial ranges descended with the correct slopes. However, there are differences regarding energy dissipation rates and resolution of smallest scales revealing an inverse relationship. Suggested by the cumulative energy budget in fig. 30, Euler FV burnt the least amount of kinetic energy contrasting PPM, Bouchut 3 and Bouchut 5, who consumed roughly 15 to 20% more. On the other hand the latter yield more details on small scales, which becomes clearly evident in the mass-weighted velocity distribution in fig. 35. Estimating the energy in the dissipative range, see table 6, does not contradict this observation. We will put this into perspective later on.

The behaviour of the Midpoint schemes falls out of place and should discussed separately. It seems that the turbulent driver creates a force field in such a unique way and over a longer period of time so that the majority of the mass is dragged into a lump surrounded by highly accelerated regions of very thin medium. See fig. 22 for a snapshot. The dissolution of those extremely high Mach regions drives up the energy dissipation substantially. See fig. 29. This remarkable example reveals the imprinting influence of the driver on the turbulence, which is a problem in its own right.

In order to gain insights on how strong the influence of the turbulent driver might be, we also conducted a decaying turbulence simulation with exact equal initial conditions. The results are described in the next section.

4.3 Decaying Turbulence

In the previous section we conducted a driven turbulence simulation, where we identified a significant influence of the turbulent driver on the modeled turbulence. Consequently, we test each solver with a decaying turbulence setup of identical initial conditions. A snapshot of a fully developed Mach-10 turbulence, generated with the Bouchut 5 solver, provides the basis for the simulations. The initial turbulence setup is left to decay six turning times relative to $\mathcal{M} = 10 \Rightarrow T_{turn} = 1/10 = 0.1$. In order to avoid interpolation errors and unsolicited oscillations during the transfer from FLASH to FLEXI (cf. sec. 3.4), the initial state was slightly smoothed beforehand via application of a Gaussian blur (cf. fig. 14). Apart from that, the setup is equivalent to the driven turbulence setup, detailed at the beginning of sec. 4.2. Table 7 gives an overview of the conducted experiments.

Table 7: Outline of the Decaying Turbulence Setup. Note the small CFL number for PPM, which turned out to be necessary in order not to crash. There is a slight variance among the initial Mach numbers/kinetic energies. They stem from the fact that these values were measured at simulation runtime, when subjected to minor numerical errors.

Solver	B3	B5	PPM	EU-FV	MP-FV	MP-HY	RK3-FV	RK3-HY
Resol. per Dim.	512	512	512	512	512	512	512	512
CFL number	0.8	0.8	0.1	0.4	0.8	0.9	0.9	1.2
initial mach number \mathcal{M}_0	9.877	9.877	9.877	9.875	9.872	9.873	9.871	9.871
initial kin. energy \mathcal{K}_0	48.78	48.78	48.78	48.76	48.72	48.73	48.72	48.72
sim. end $t_{\text{sim. end}}$	6.0	6.0	6.0	6.0	6.0	6.0	6.0	6.0
nr. checkpoints $N_{\text{checkpoints}}$	30	30	30	30	30	30	30	30

4.3.1 Mach Number Evolution

In contrast to the different decay rates in fig. 20, the declines of the Mach number over time (fig. 40) are unexpectedly alike. The decaying turbulences start at $\mathcal{M} = 10$ and take six crossing times to drop below the supersonic regime ($\mathcal{M} = 1$).

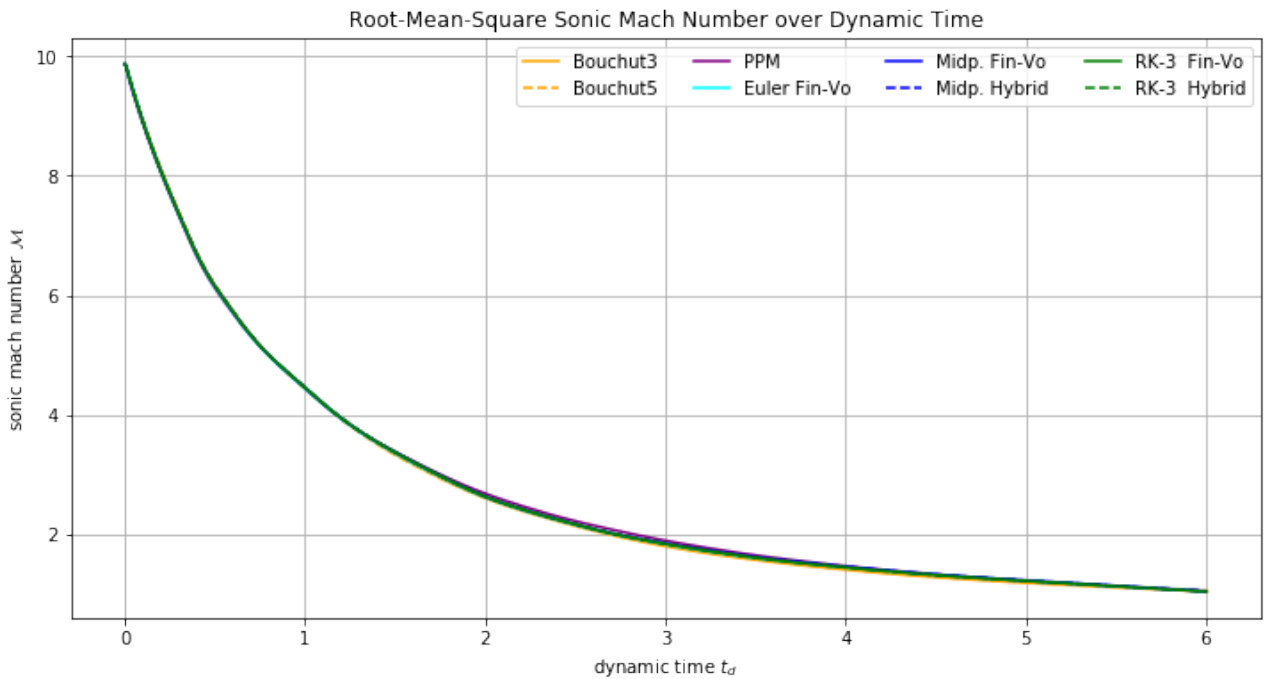


Figure 40: Time evolution of the root-mean-square mach number.

4.3.2 Column Density & Velocity

Here we present a series of column density and velocity snapshots of all conducted simulations at three successive stages of turbulent decay: $t_d = [1, 2, 3]$ with $\mathcal{M} = [4.2, 2.4, 1.9]$, respectively. See fig. 41 to fig. 49. The exact point of time, the solver and the Mach number are attached to each snapshot in the title and the figure caption.

First of all, the large scale structures are congruent among all solvers, when comparing the snapshots at equal points in time. As already discussed in sec. 2.2.1, dissipation happens only at small scales. And since the velocity field is not influenced by external forces, the large scale movements are conserved.

The originally smoothed initial state (cf. fig. 14) reestablished the shocks, which can be clearly seen by the sharp edges of the filamentary structures in fig. 41 to fig. 43. As expected, those structures gradually dissolve with increasing time, which leads to a transformation of kinetic energy into internal energy. It then escapes the system via polytropic cooling. This process is indicated by the increased darkening of the column Mach number plots as time progresses.

It is impossible to tell from the snapshots if there are differences in the resolution of small scales. In analogy to the driven turbulence setup, density PDFs and powerspectra will give a better insight into this matter.

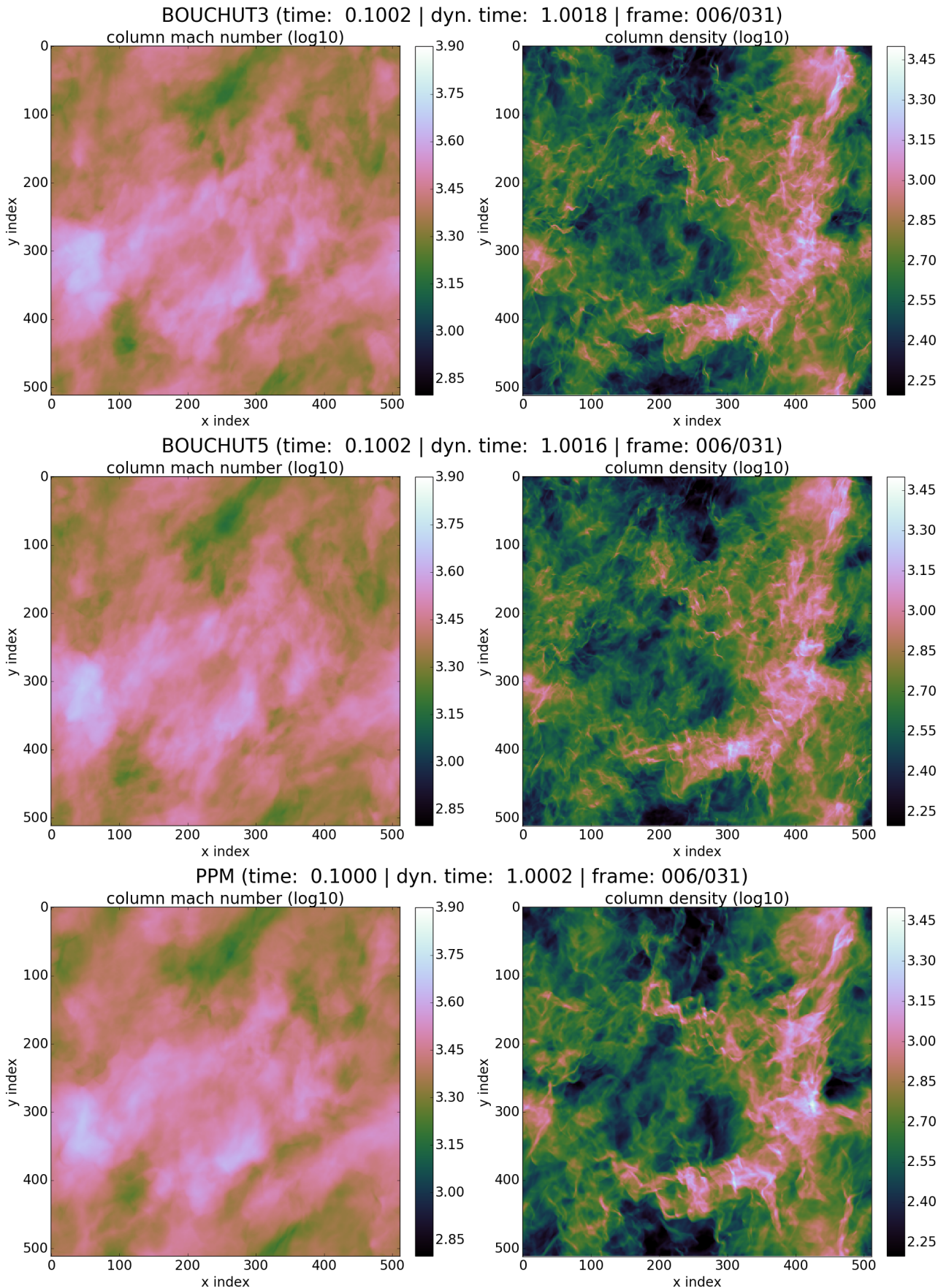


Figure 41: Decaying Turbulence from Mach 10: Column Sonic Mach Number and column density along z-axis at $t_d = 1.0$ when the root-mean-square mach number has fallen to $\mathcal{M} = 4.2$

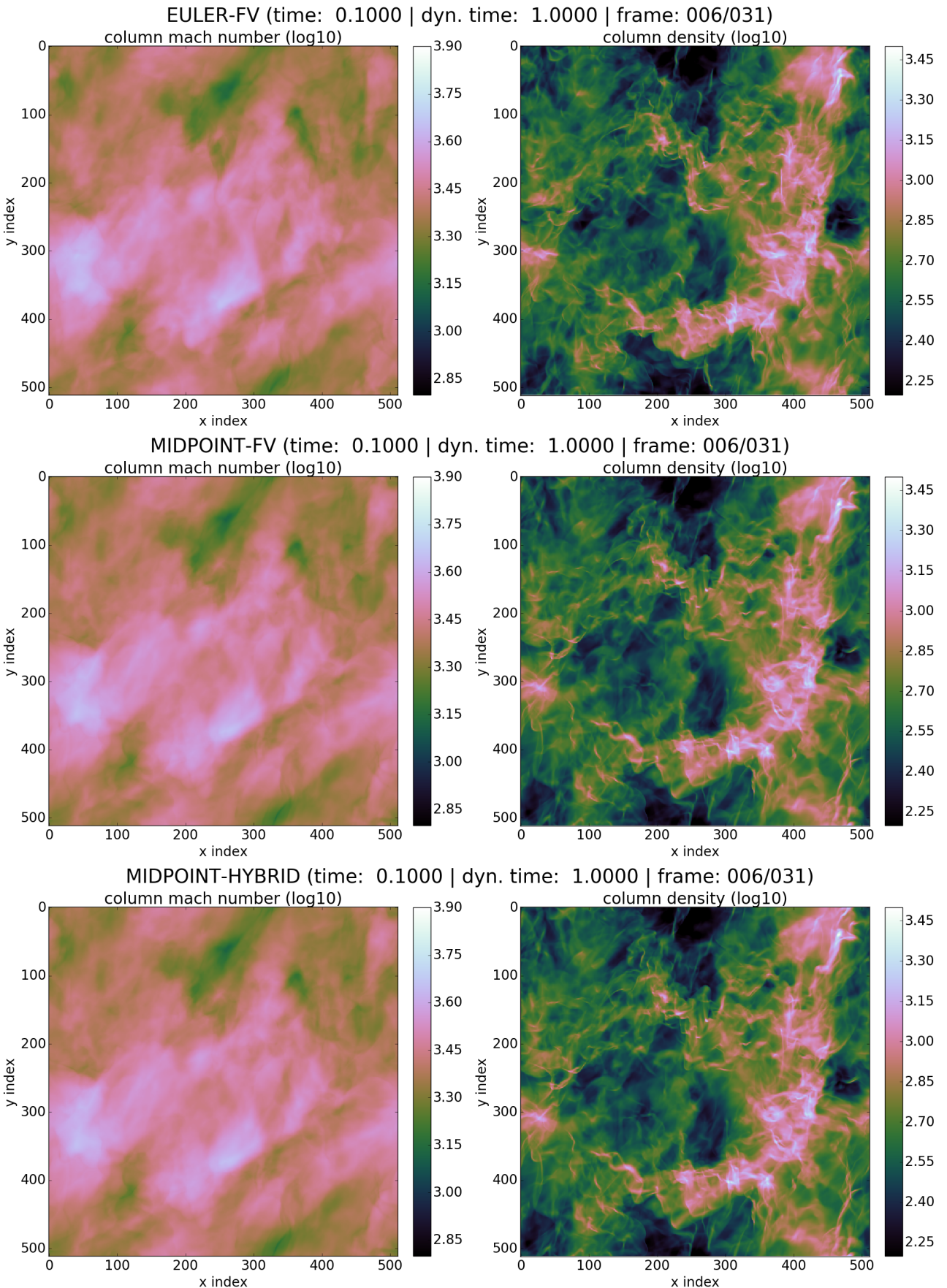


Figure 42: Decaying Turbulence from Mach 10: Column Sonic Mach Number and column density along z-axis at $t_d = 1.0$ when the root-mean-square mach number has fallen to $\mathcal{M} = 4.2$

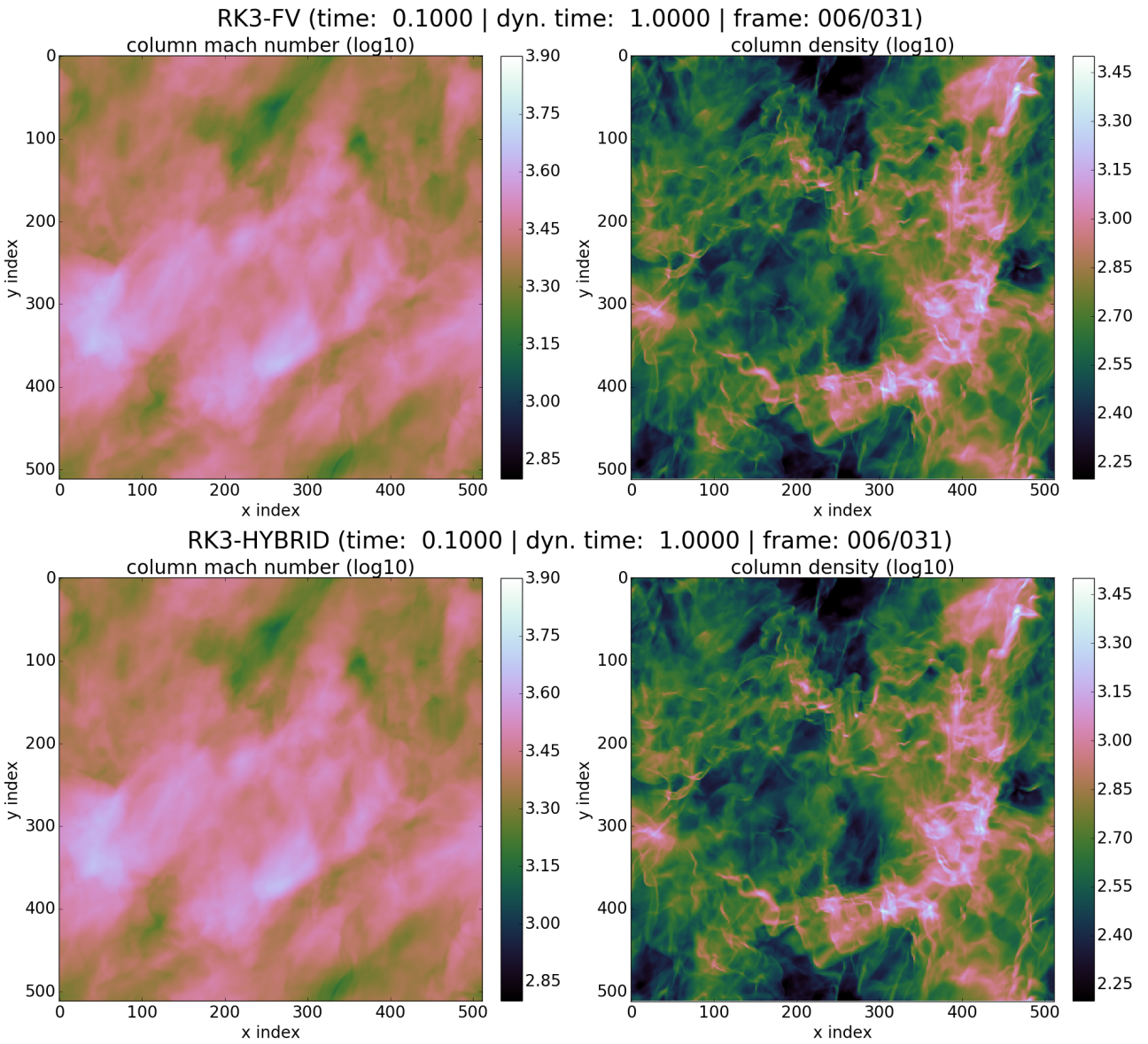


Figure 43: Decaying Turbulence from Mach 10: Column Sonic Mach Number and column density along z-axis at $t_d = 1.0$ when the root-mean-square mach number has fallen to $\mathcal{M} = 4.2$

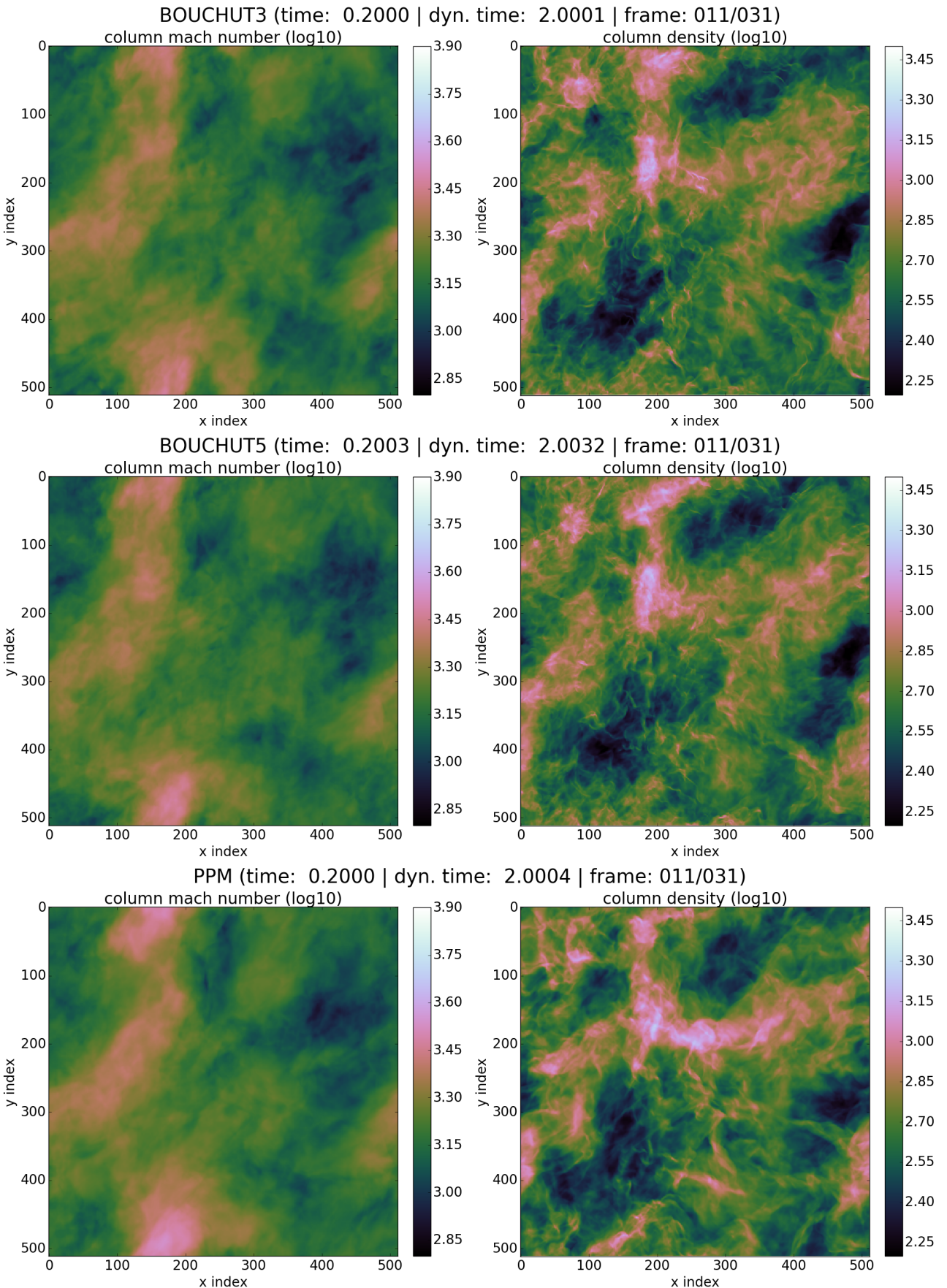


Figure 44: Decaying Turbulence from Mach 10: Column Sonic Mach Number and column density along z-axis at $t_d = 2.0$ when the root-mean-square mach number has fallen to $\mathcal{M} = 2.4$

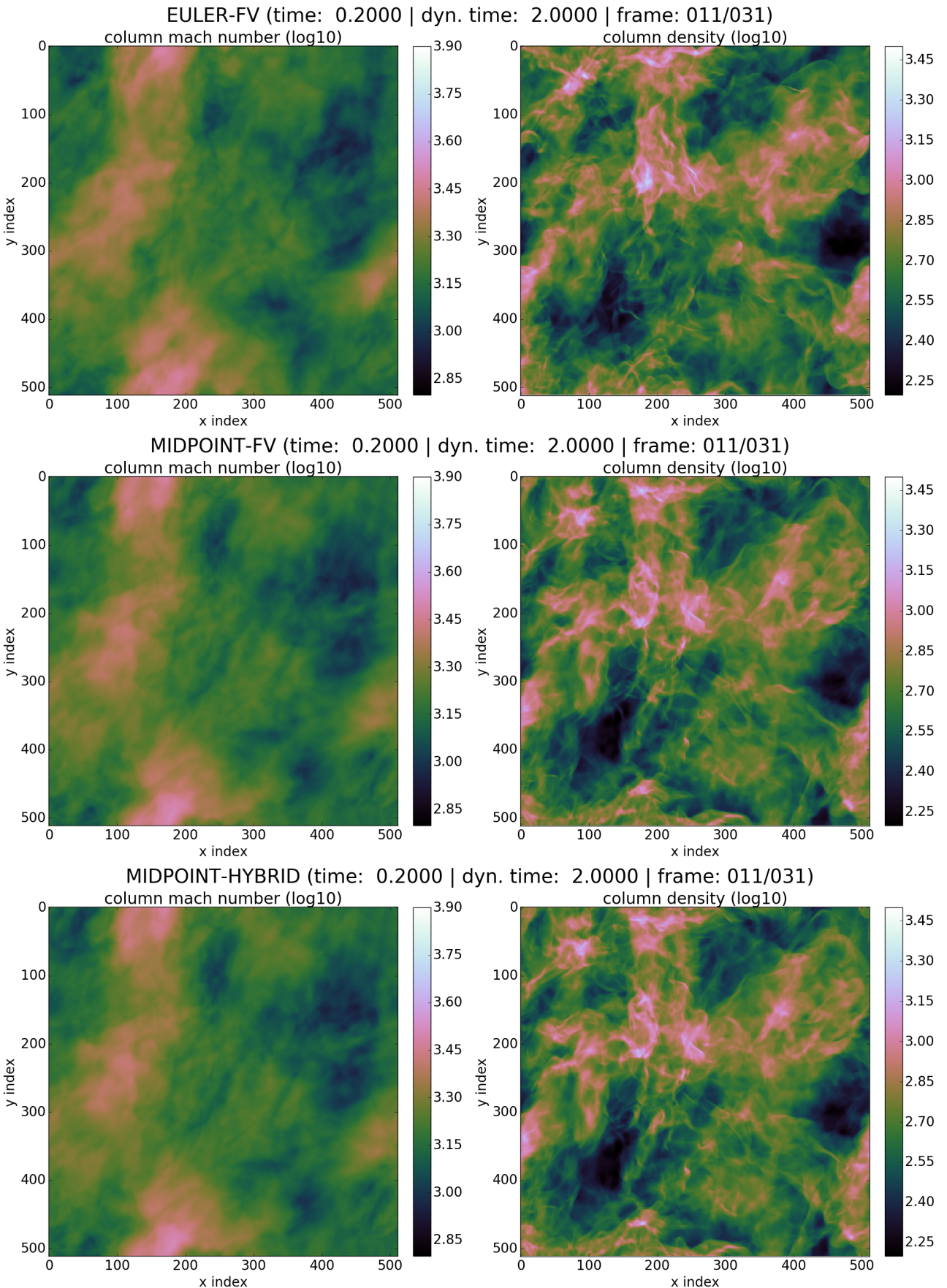


Figure 45: Decaying Turbulence from Mach 10: Column Sonic Mach Number and column density along z-axis at $t_d = 2.0$ when the root-mean-square mach number has fallen to $\mathcal{M} = 2.4$

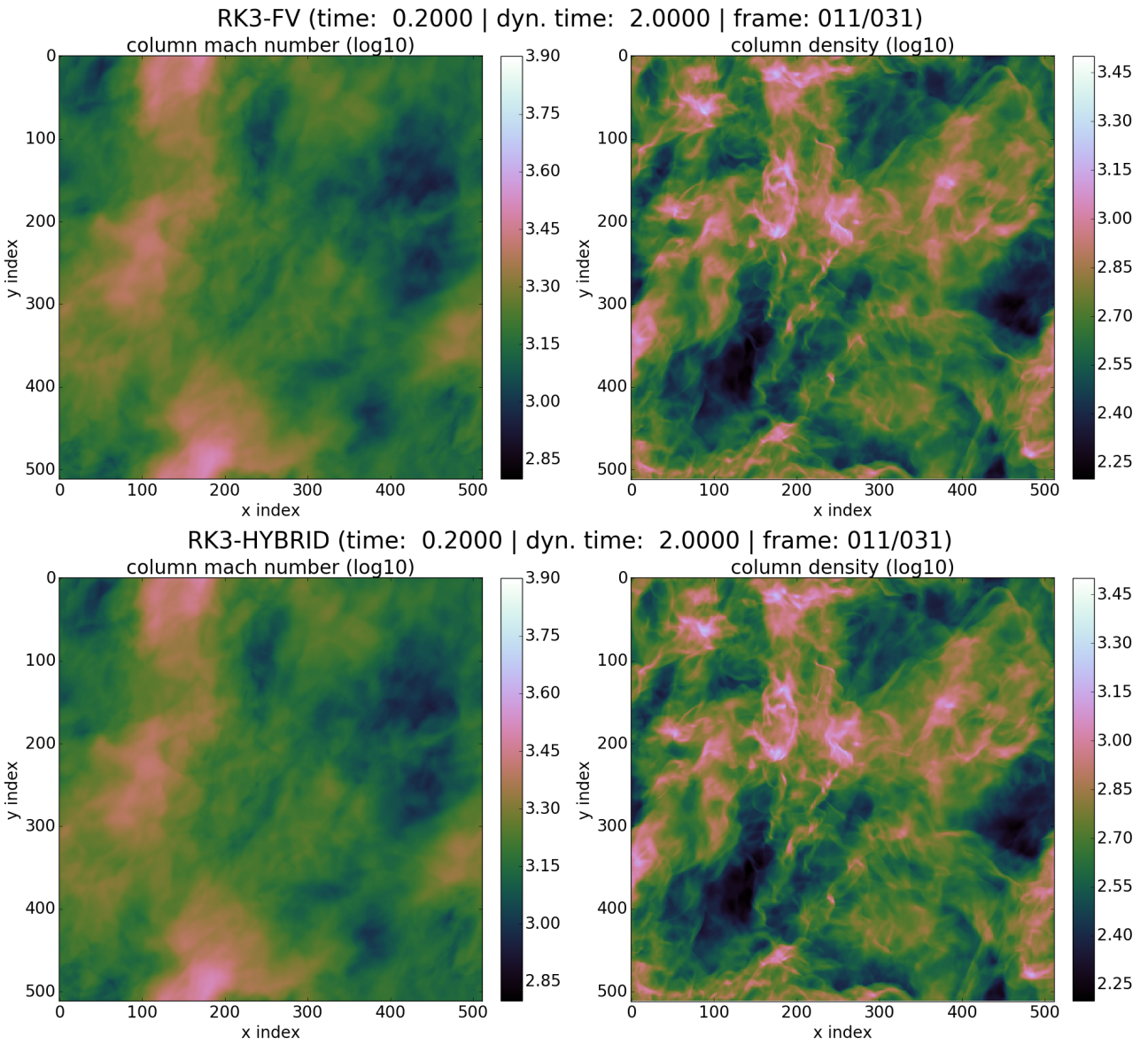


Figure 46: Decaying Turbulence from Mach 10: Column Sonic Mach Number and column density along z-axis at $t_d = 2.0$ when the root-mean-square mach number has fallen to $\mathcal{M} = 2.4$

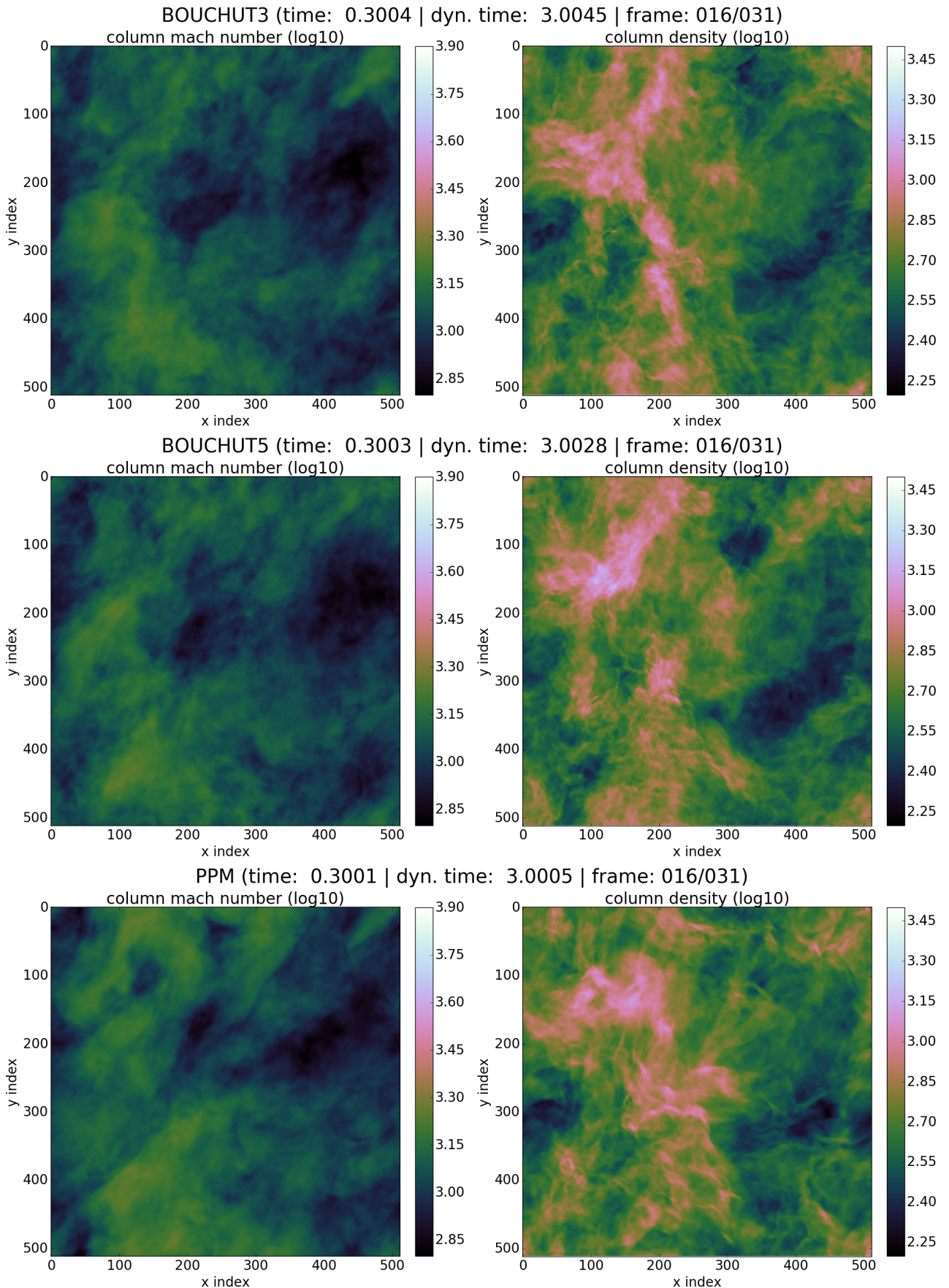


Figure 47: Decaying Turbulence from Mach 10: Column Sonic Mach Number and column density along z-axis at $t_d = 3.0$ when the root-mean-square mach number has fallen to $\mathcal{M} = 1.9$

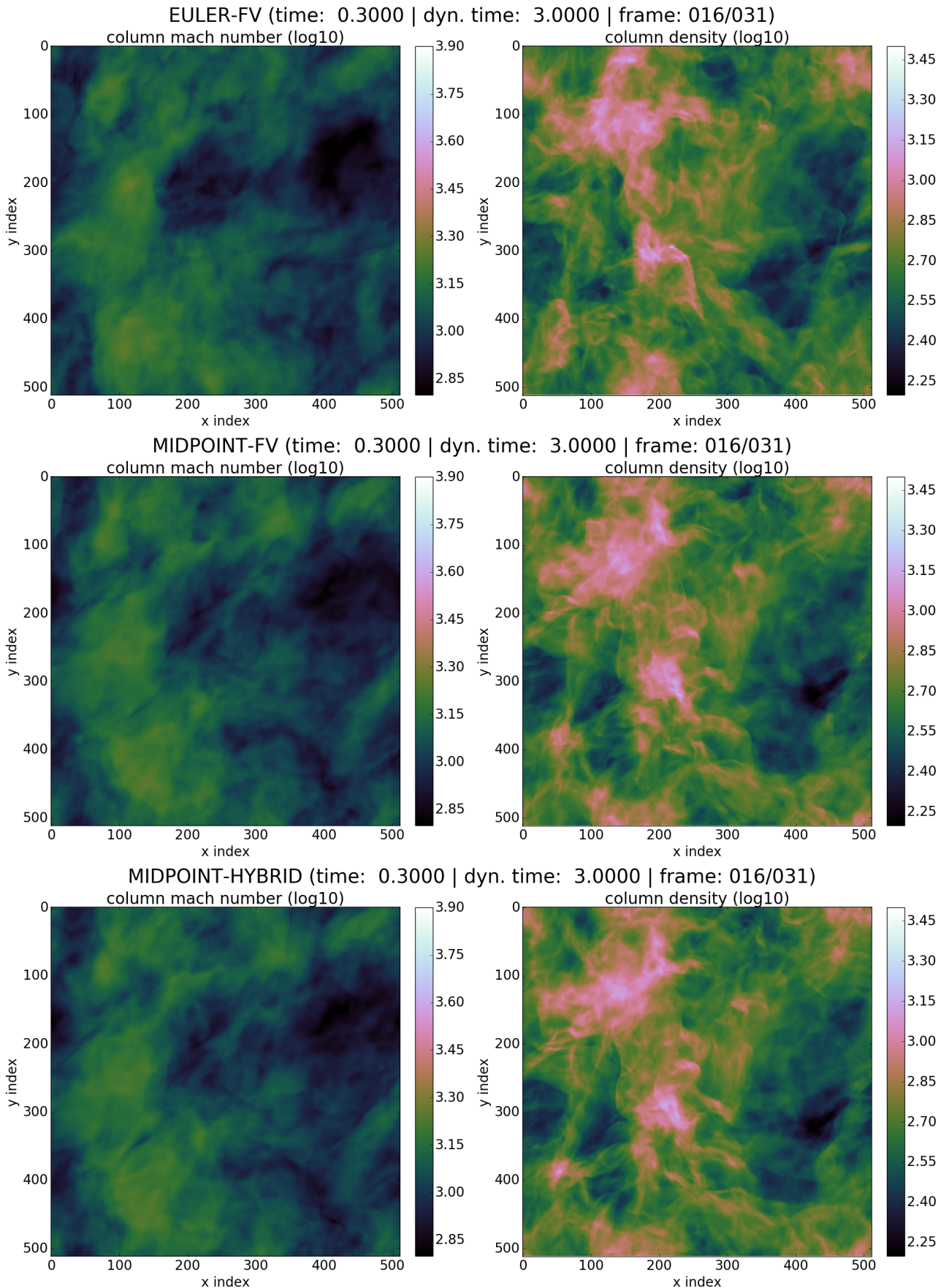


Figure 48: Decaying Turbulence from Mach 10: Column Sonic Mach Number and column density along z-axis at $t_d = 3.0$ when the root-mean-square mach number has fallen to $\mathcal{M} = 1.9$

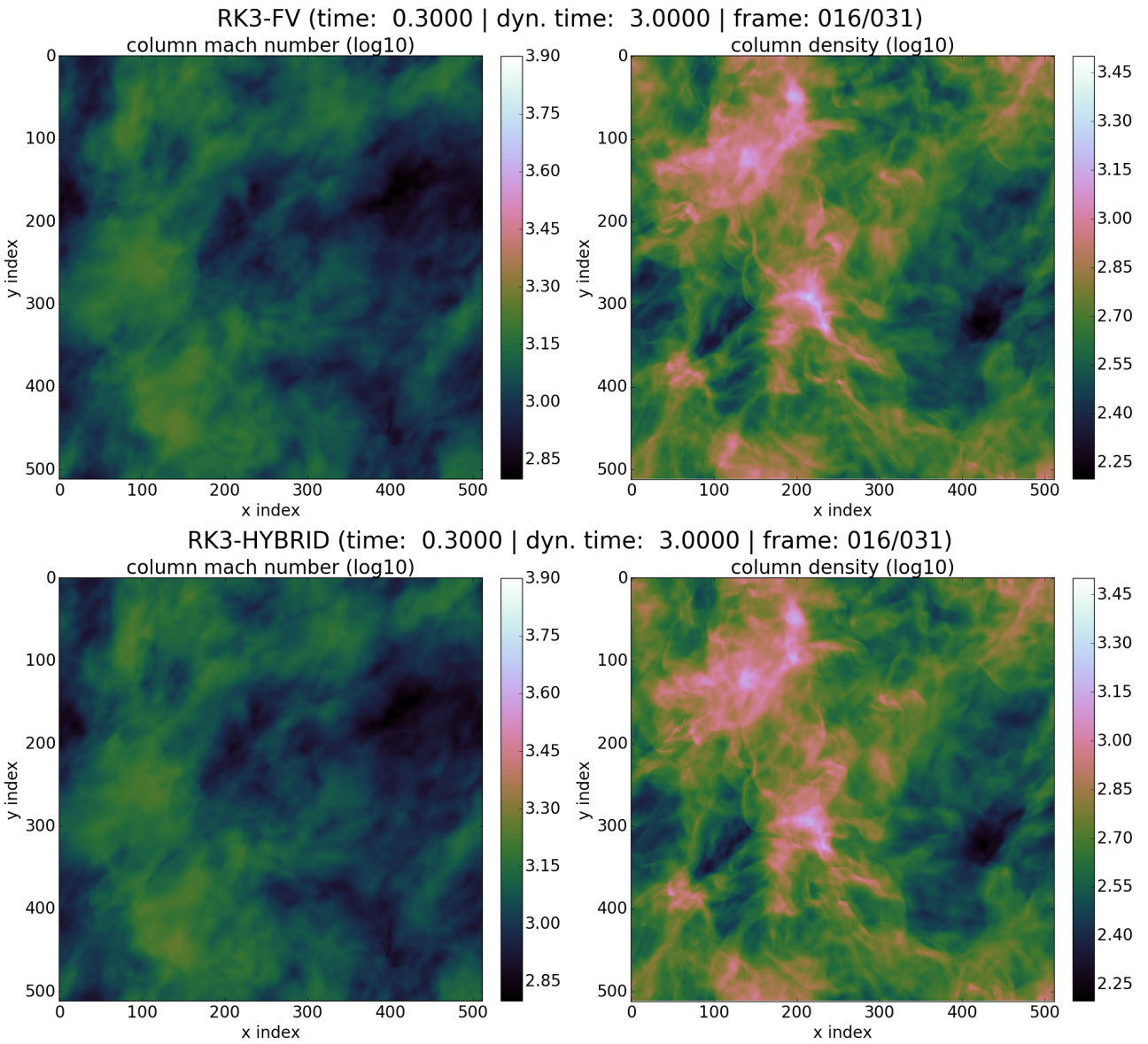


Figure 49: Decaying Turbulence from Mach 10: Column Sonic Mach Number and column density along z-axis at $t_d = 3.0$ when the root-mean-square mach number has fallen to $\mathcal{M} = 1.9$

4.3.3 FV-DG Mode Switching

In fig. 50 the initially smoothed turbulence immediately shapes strong shocks everywhere, hence the sudden jump to over 95% FV elements. After that the situation alleviates a bit and more DG elements can be reintroduced. For not too long the second culmination of shocks appears and the amount of FV elements rises again. From $t_d = 1$ onward the ratio declines in the same fashion as in fig. 27.

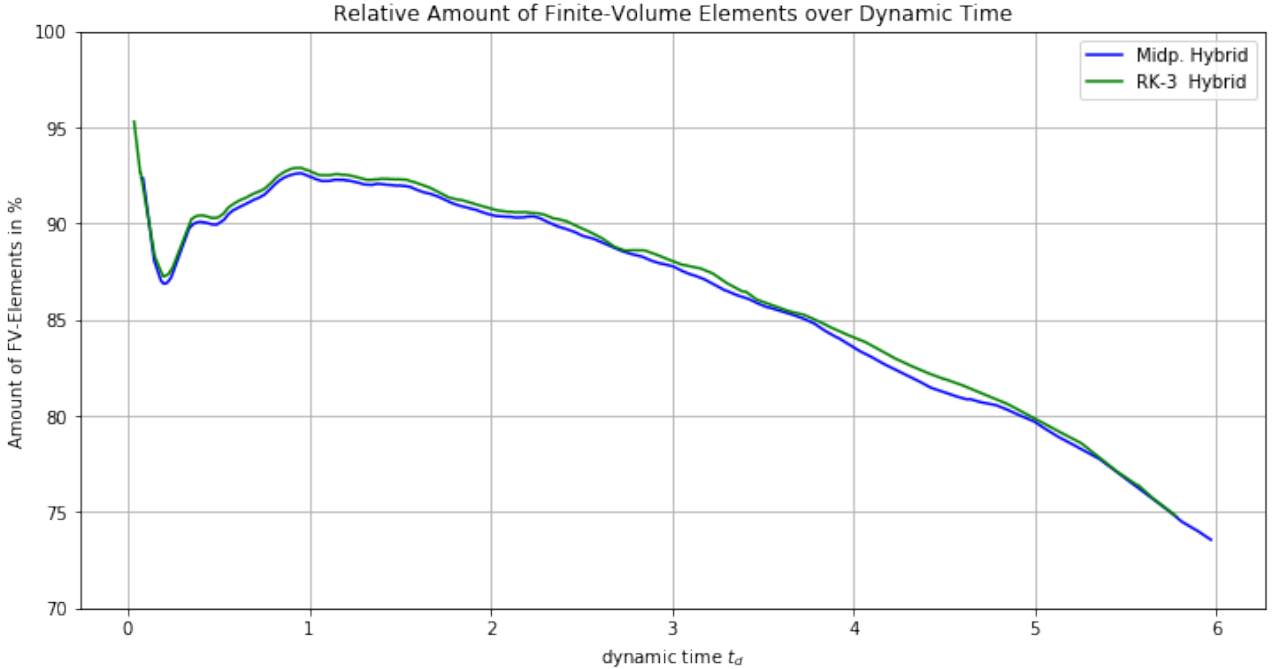


Figure 50: Time evolution of the fraction of finite volume elements to the total number of elements.

Remark The other solvers would stay at 100% since they operate solely with finite volumes.

4.3.4 Energy Dissipation

The course of the total energy in fig. 51 is plotted in logarithmic scale so that the kinetic energy can be visually distinguished from the total energy. Polytropic cooling keeps the system at constant temperature, hence the internal energy stays steady over time. There is no obvious difference among the solvers. The deprived internal energy is equivalent to the dissipated kinetic energy (fig. 52). See discussion under sec. 4.2.4. Right after the simulation has started, strong shocks emerge and the dissipation rate shoots up to its highest peak. By applying numerical integration $\int dt_d - \frac{d\mathcal{K}}{dt_d} = 48.251 \pm 0.007$, the initial kinetic energy is recovered $\mathcal{K}_0 = 48.75 \pm 0.03$, besides a tiny fraction of $\Delta\mathcal{K} = 0.5 \pm 0.03$ still left in the system. This simple calculation reveals two insights. First, there are no noticeable energy sources or sinks apart from polytropic cooling. Thus, the energy accounting is balanced. Second, the variation in dissipated energy among the solvers is negligible. Conclusively, there is no difference in dissipation with this setup, which contradicts the results of the driven turbulence.

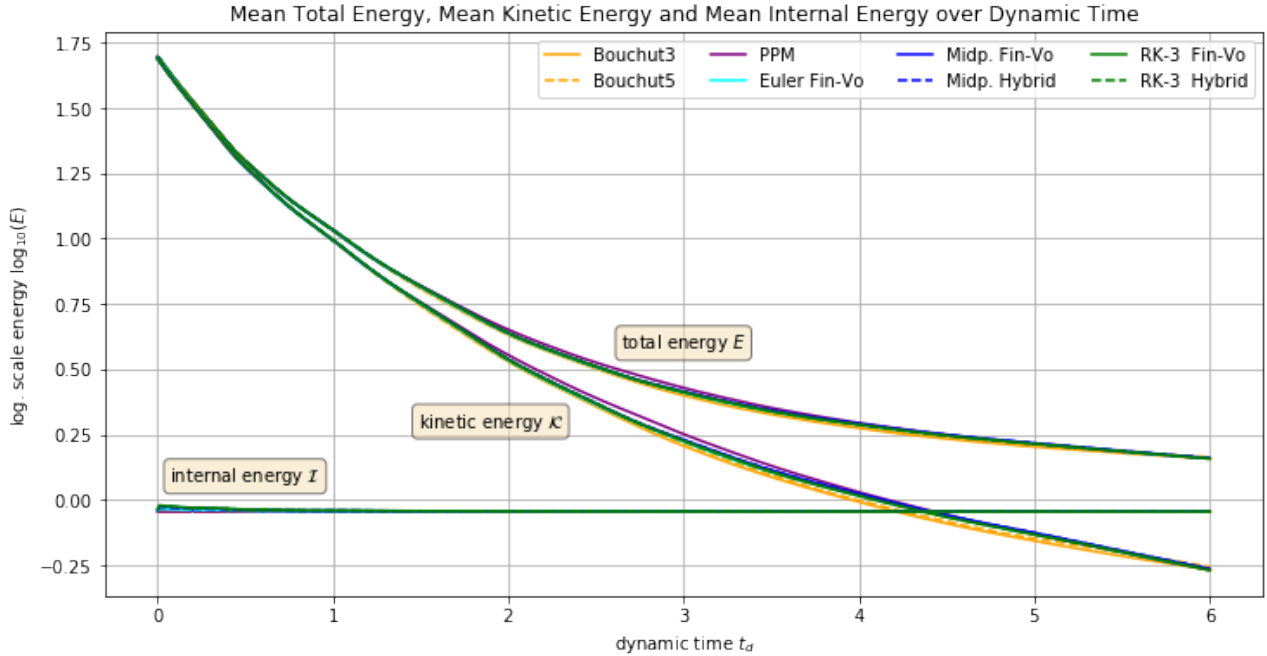


Figure 51: Time evolution of the energy. The logarithmic scaling helps to visually distinguish the course of total and kinetic energy. The total energy E is the sum of the kinetic \mathcal{K} and internal energy \mathcal{I} : $\log_{10}(E) = \log_{10}(\mathcal{I} + \mathcal{K})$.

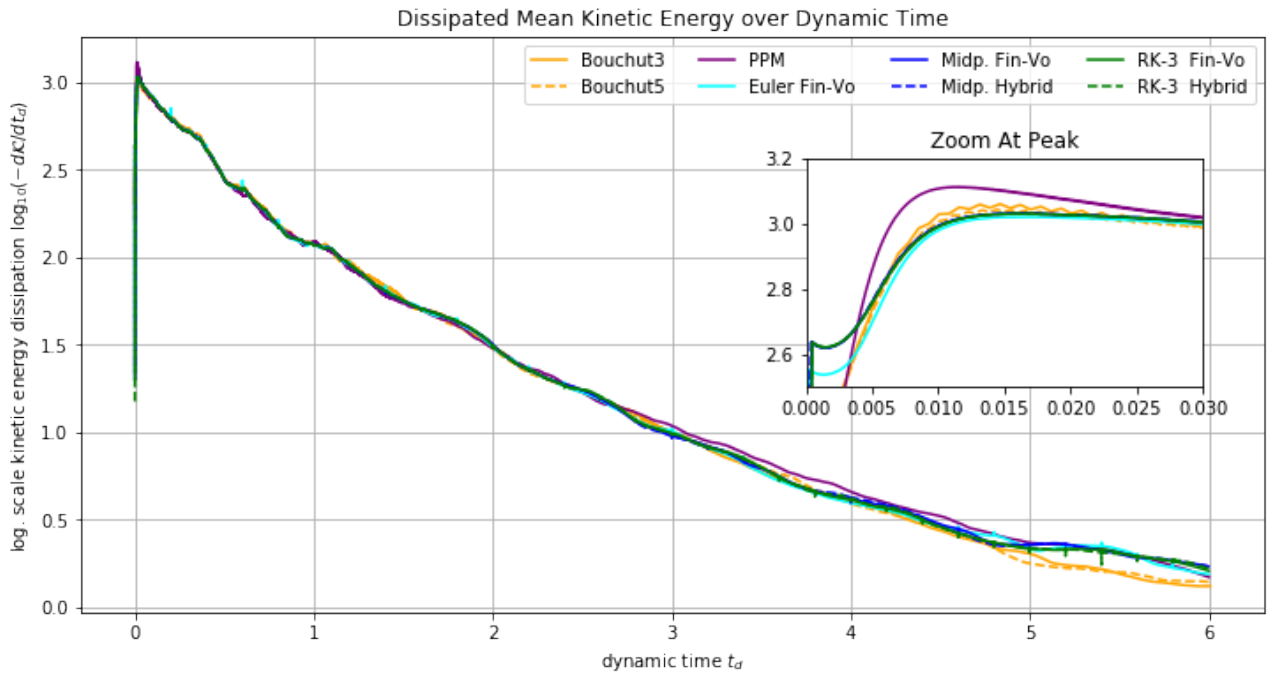


Figure 52: Time evolution of the kinetic energy dissipation in logarithmic scale $\log_{10}(-\frac{d\mathcal{K}}{dt_d})$. The averaged area (numerical integration) under the plots amounts to $\int dt_d - \frac{d\mathcal{K}}{dt_d} = 48.251 \pm 0.007$ which is almost all of the initial kinetic energy: $\mathcal{K}_0 = 48.75 \pm 0.03$.

4.3.5 Density & Velocity Distributions

In agreement with fig. 31, FLEXI's solvers retain more mass on the outer scales than FLASH's. Fitting was done with eqn. 58 in the same manner as in the driven turbulence (cf. sec. 4.2.5). From the width of the log-normal fits we try to reconstruct the sonic Mach number at that time. The result is shown in fig. 54.

The volume-weighted velocity PDFs in fig. 55 do not show anything surprising besides the fact that there is no significant bulk motion (cf. sec. 4.2.5).

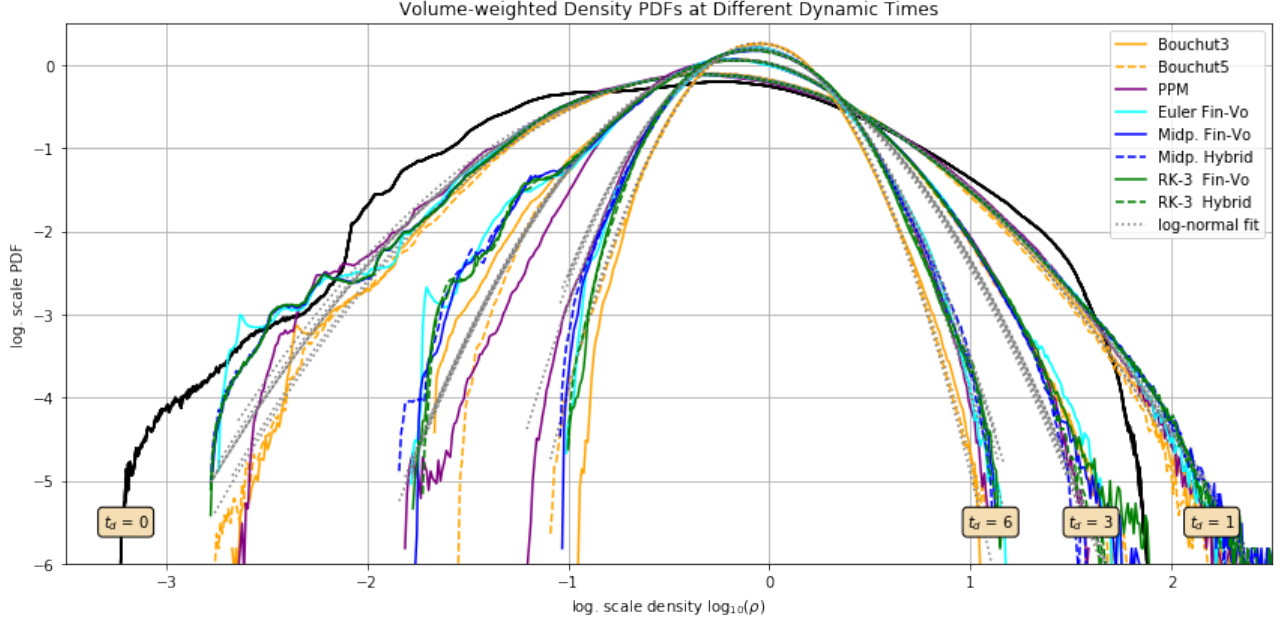


Figure 53: Log-log scale volume-weighted density PDFs. As the decay progresses, the widths of the distributions decrease and the mean values return to the initial density: $\log_{10}(\rho_0) = \log_{10}(1) = 0$. The solid black curve depicts the density distribution of the smoothed initial state (cf. fig. 14). The applied Gaussian blur truncated the high density range. The log-normal fit (dotted lines) were done with eqn. 58.

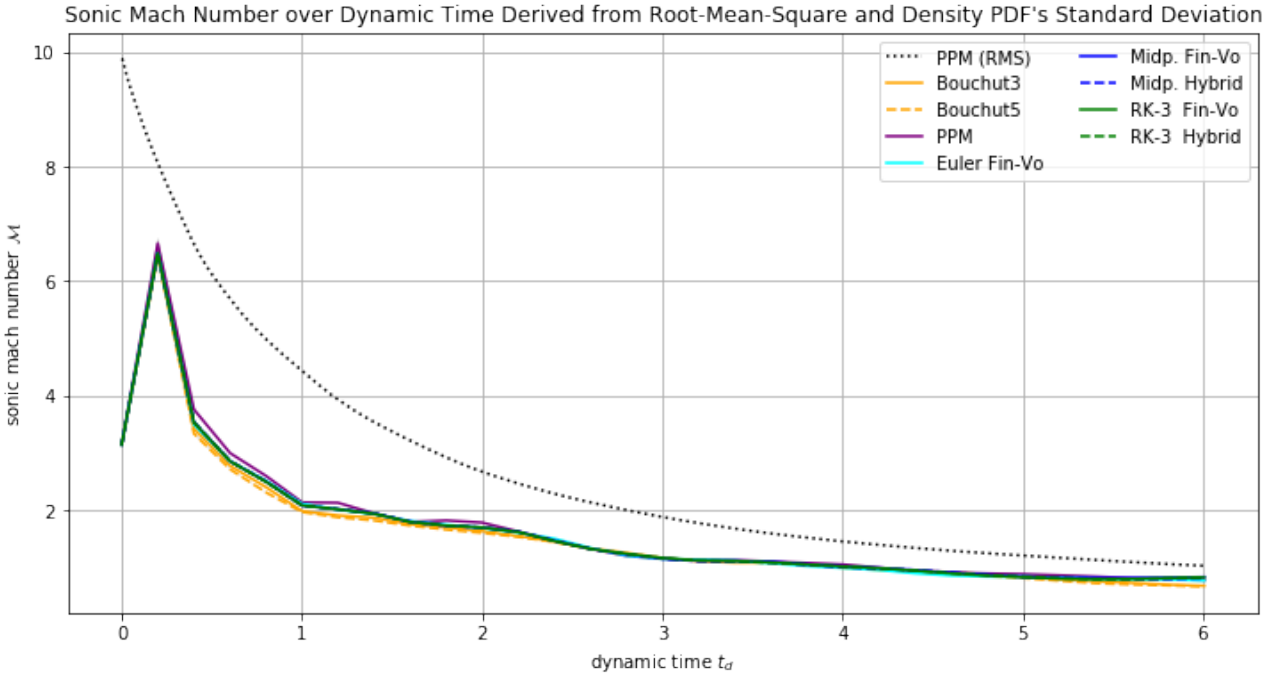


Figure 54: Time evolution of the sonic mach number over time derived from the width of the volume-weighted density PDFs of the decaying turbulence. The dashed line represents the root-mean-square velocity of the PPM solver and serves as a reference. Due to the lognormal relationship, the fit yields very low error margins. Hence, the error bars are too small to see. The spike on the left is caused by the originally smoothed initial state. The turbulence has to redevelop in order to yield sensible results. However, the Mach number estimation via relation eqn. 58 ($b = 2/3$) is systematically below the reference. This agrees with the results in the decay phase of the driven turbulence (cf. sec. 4.2.5).

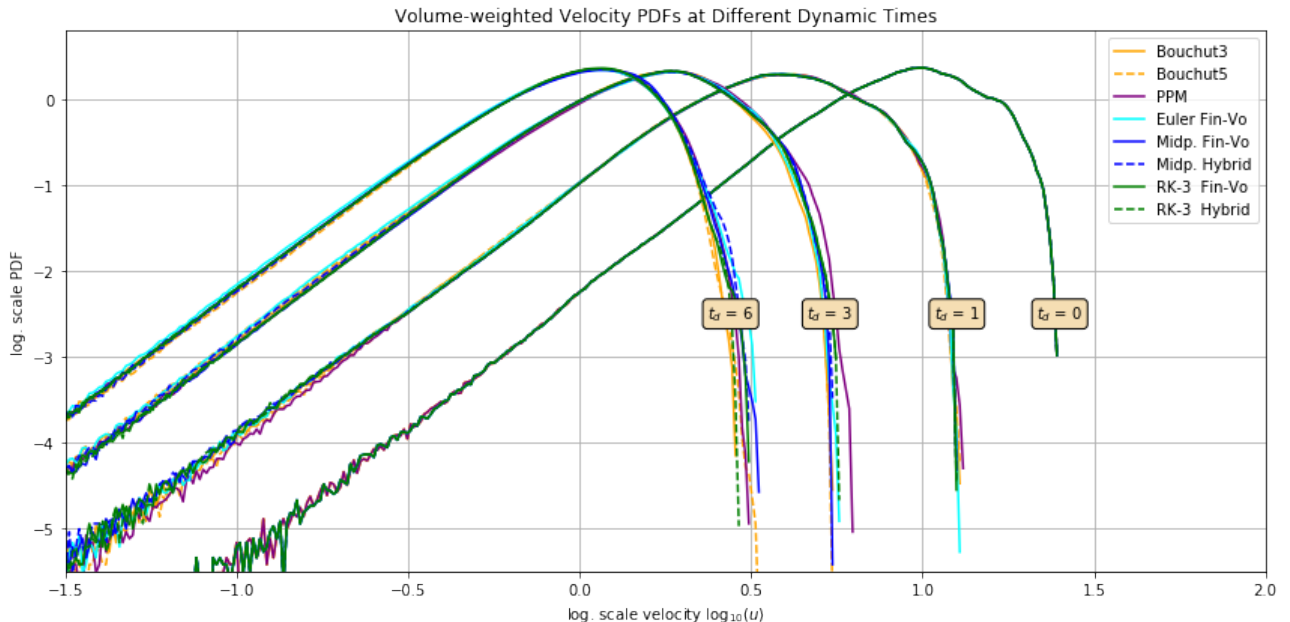


Figure 55: Log-log. scale volume-weighted velocity PDFs moving from right to left with increasing time due to kinetic energy decline of the decaying turbulence. The median point of the initial PDF at $t_d = 0$ is precisely over Mach 10: $\mu_0 = \log_{10}(1) = 10$. A non-existent dispersion of the PDFs over time indicates no bulk motion which is a good sign (cf. sec. 4.2.5).

4.3.6 Energy & Velocity Powerspectra

In analogy with sec. 4.2.6, we will take a look at the kinetic energy and the velocity powerspectra. In addition to the density PDF, discussed in the previous section, they allow us to gain an insight into the resolution of movement on small spatial scales. Since the kinetic energy declines over time, the powerspectra in fig. 56 shift downwards. At the end of the simulation, $t_d = 6$, PPM retained the most energy in the dissipation range. It is interesting to see that there still is an imprint left from the turbulent driver, who produced the original turbulence. The buckling of the spectra within the large scale range is typical for driven turbulences. During the evaluation of the column density/velocity snapshots under sec. 4.3.2 we discussed the preservation of large scale structures over long periods of time. This observation resurfaces here again.

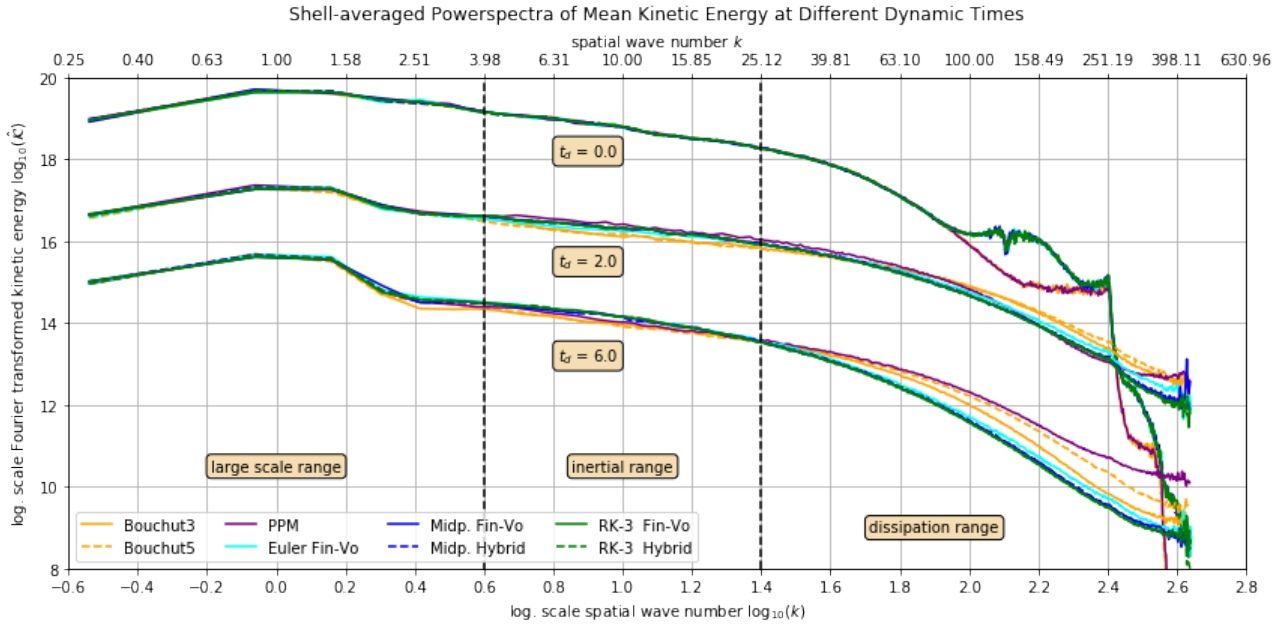


Figure 56: Powerspectra of the volume-weighted mean kinetic energy field shown for three stages of decay: $t_d = 0$, $t_d = 3.0$ and $t_d = 6.0$. Since the total kinetic energy declines over time the powerspectra shift downwards. The strange looking spectrum from $t_d = 0$ is the result of the applied Gaussian blur on the initial state. In agreement with [22] (resolution: 512^3), the beginning of the dissipative range is estimated to $k_{diss} \approx 25$, where the spectra start the bend down.

Fig. 57 and fig. 58 show that all simulations maintain the energy cascade already present in the initial state. The related powerspectra $t_d = 0$ are a bit distorted from the Gaussian blur, but the initial slope of the inertial range is very near the expectation marked by the solid black line on top of the plot. As described in detail in sec. 4.2.6, the slopes flatten with increasing time, since the energy cascade slowly breaks down with progressing decay.

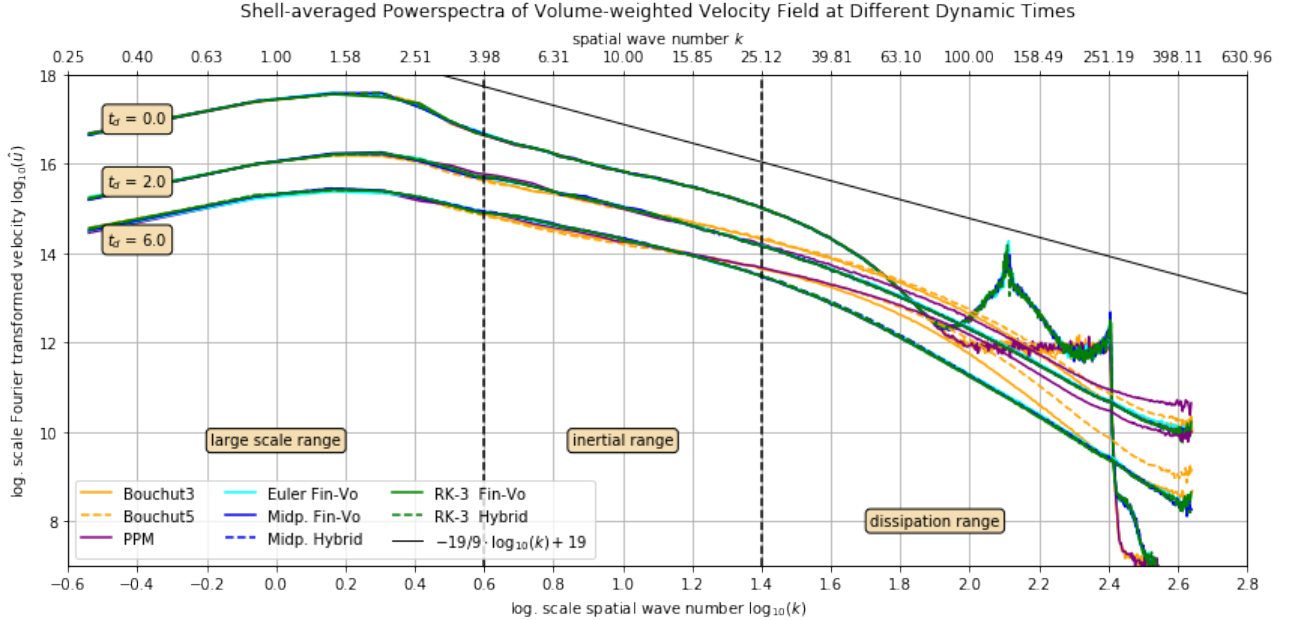


Figure 57: Powerspectra of the volume-weighted velocity field for three stages of decay: $t_d = 0$, $t_d = 3.0$ and $t_d = 6.0$. Since the total kinetic energy declines over time, the powerspectra shift downwards. The strange looking spectrum from $t_d = 0$ is the result of the applied Gaussian blur on the initial state. In agreement with [22] (resolution: 512^3), the beginning of the dissipative range is estimated to $k_{diss} \approx 25$, where the spectra start the bend down.

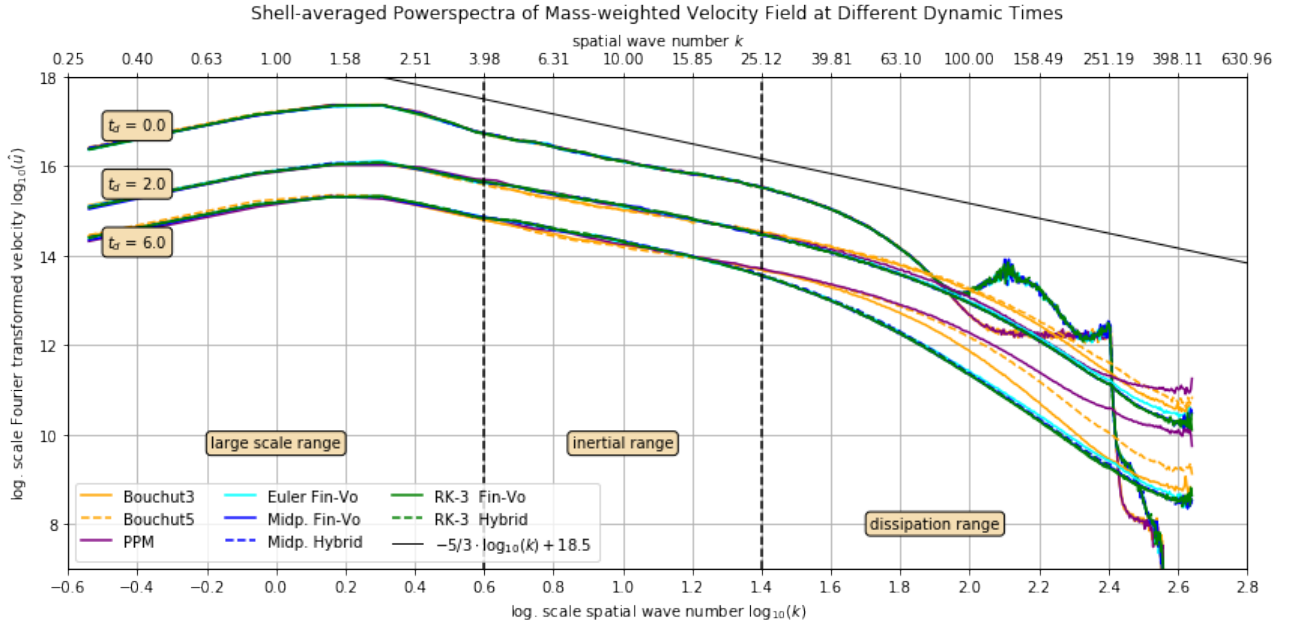


Figure 58: Powerspectra of the mass-weighted velocity field for three stages of decay: $t_d = 0$, $t_d = 3.0$ and $t_d = 6.0$. Since the total kinetic energy declines over time, the powerspectra shift downwards. The strange looking spectrum from $t_d = 0$ is the result of the applied Gaussian blur on the initial state. In agreement with [22] (resolution: 512^3), the beginning of the dissipative range is estimated to $k_{diss} \approx 25$, where the spectra start the bend down.

4.3.7 Summary

The decaying turbulence setup was conducted in analogy with the driven setup under sec. 4.2. A fully developed Mach 10 turbulence was let to decay by FLASH's and FLEXI's solvers. In a comparative study we evaluated column density/velocity snapshots at three different stages of decay and underpinned the observations with density distributions and powerspectra.

All schemes provided very similar solutions with minor differences on small scales. See fig. 41 to fig. 49. A variance in energy dissipation rates (cf. fig. 52) was not quantifiable. In accordance with the results of the decay phase of the driven turbulence (cf. sec. 4.2.5) the relation between density PDF and sonic Mach number (cf. sec. 2.2.2) systematically underestimates the correct root-mean-square Mach number (cf. fig. 54). Apparently, the relation does not hold for decaying turbulences. The accurate modelling of the energy cascade was confirmed by the velocity powerspectra in fig. 57 and fig. 58.

There is no clear winner, who resolves small scale structures best. On the one hand, FLASH's solvers contain more energy in the dissipative range of the kinetic energy powerspectra (cf. fig. 56) throughout the simulation. But on the other hand, the solver from FLEXI show more amount of mass on both ends of the density spectrum (cf. fig. 53). However, one should not forget that all plots are in log-log scale which means that subtle differences are enhanced.

Subsequent decay simulations with lower and higher Mach numbers show the same results. FLEXI is expected to be less dissipative. But even PPM, which is considered more accurate than Bouchut5, does not show better results. Apparently, this particular setup, that is isothermal turbulent decay, is not suited to benchmark numerical schemes with regards to dissipation rates. It might be the case that the polytropic cooling has a “grinding” effect on small scales. Shocks get sharpened till the solver cannot resolve them anymore. Any reconstruction attempts are annihilated by the flux limiters, who try to save what can be saved. Consequently, the influence of the Riemann solvers dominates. The positive effect of higher-order methods never get a chance to take effect.

The decaying turbulence setup is also revealing in the sense that the influence of turbulent forcing on the dissipation rates is immense. Despite bulk motion correction, the driver still might tend to induce slightly counter-rotating mass congregations, which throttle the energy cascade. Maybe this explains why FLEXI shows somewhat steeper slopes in the velocity spectra (cf. table 6). It would also explain why FLEXI shows less features in the small scales and why Euler FV and both RK3 solvers appear to be less dissipative.

5 Conclusion & Outlook

The goal of this thesis was to investigate if it is feasible to apply a recent third-order discontinuous Galerkin method (FLEXI) to astrophysical turbulence simulations and how they compare to established first/second order finite volume methods (FLASH). The objective is that DG methods are less dissipative and better resolve small scale structures.

The primary focus was to accurately model isothermal turbulences up to Mach 10 which are, for example, important for simulating star formation rates in molecular clouds.

As a first step FLEXI was augmented in order to support isothermal turbulence setups in the same way as FLASH does. Modules for polytropic cooling, turbulent forcing, bulk motion correction and shock capturing were implemented and integrated into FLEXI (cf. sec. 3.1). These modifications were then tested and verified with the Sod Shock Tube problem (cf. sec. 4.1).

Since pure Galerkin schemes cannot cope with discontinuities, shock capturing routines try to dampen spurious oscillations and, as a last resort, locally switch to second-order finite volumes. In theory, this hybrid scheme should yield a convergence rate somewhere between 2 to 3, depending on the ratio of DG elements to FV elements (cf. sec. 3.3).

The next step was to conduct driven turbulence simulations of Mach 2.5 with three explicit time integration methods of ascending order (first order Euler, second order Midpoint and third-order Runge-Kutta) each in combination with hybrid and FV-only mode. The same simulation was also performed with three solvers from FLASH: PPM, Bouchut3 and Bouchut5. They serve as reference (cf. sec. 4.2).

In order to check the influence of the turbulent forcing, this study was concluded by a decaying turbulence setup with identical initial conditions among all solvers (cf. sec. 4.3).

Side-by-side comparison of column density snapshots at different times and methods from turbulence statistics, namely density PDFs and powerspectra, gained insights into the quality of the resulting turbulences.

We arrive at following conclusions:

- The evaluation of the simulation data is in good agreement with the reference. Supersonic isothermal turbulent decay is modeled equally by all analyzed solvers (cf. sec. 4.3.2 and sec. 4.3.5). No significant difference among dissipation rates (cf. fig. 52) has been measured.
- Isothermal turbulent decay, in the way applied here, is an unsuitable setup to benchmark numerical schemes. Polytropic cooling might have a “grinding” effect which renders higher-order reconstruction and DG schemes useless. The conclusion of sec. 4.3 elaborates on this.
- Turbulent driving for four turning times is too short to reach a stationary state and get reliable statistics. (cf. fig. 20) This is especially true, when comparing two totally different simulation frameworks. In fact, serious driven turbulence studies drive more than 10 turning times (cf. [26]).
- The driven turbulence simulations are substantially influenced by the driver. This is, in particular, obvious for the results by the Midpoint schemes. It renders our dissipation rates inconclusive. Apparently, turbulent driving should be treated with caution as it can

lead to unnatural pseudo-turbulent flows (cf. fig. 22).

- A grid size of 512^3 cells is still rather low in order to have a good approximation of an isothermal turbulent flow. In the powerspectra we identified the beginning of the dissipation range at $k_{diss} \approx 25$. This means a small structure, say a shock, occupies $512/25 \approx 21$ cells³ in one dimension. That is 4% of the box length. Since the Reynolds number is, in theory, infinity (cf. sec. 2.2), the turbulent flow should go beyond k_{diss} . Hence, the simulations are under-resolved.

The improvement in dissipation rates and resolution capacity, as we had hoped for, was not achieved. To be honest, it would have been a surprise anyway. In fact, a supersonic isothermal turbulent flow is one of the worst setups one can choose to run higher-order Galerkin methods on.

In essence, what we have shown is that discontinuous Galerkin methods can work in strong shock environments. It makes sense, now, to look for astrophysical problems where DG methods indeed have a chance to yield better results without worrying that occasional shock conditions crash the simulation.

Protoplanetary disk simulations, for example, still have problems with spurious angular momentum dissipation. Higher-order discontinuous Galerkin methods, in combination with recent flux functions, might yield promising results.

³Counting the cells under the peaks in fig. 19 (isothermal Sod w. strong shock) yields the same number, by the way.

References

- [1] Milton Abramowitz and Irene A Stegun. *Handbook of mathematical functions: with formulas, graphs, and mathematical tables*, volume 55. Courier Corporation, 1964.
- [2] Harold Atkins and Alyssa Pampell. Robust and accurate shock capturing method for high-order discontinuous galerkin methods. In *20th AIAA Computational Fluid Dynamics Conference*, page 3058, 2011.
- [3] Dinshaw S. Balsara. Multidimensional hll riemann solver: Application to euler and magnetohydrodynamic flows. *Journal of Computational Physics*, 229(6):1970–1993, 2010.
- [4] Dinshaw S Balsara, Christoph Altmann, Claus-Dieter Munz, and Michael Dumbser. A sub-cell based indicator for troubled zones in rkdg schemes and a novel class of hybrid rkdg+ hweno schemes. *Journal of Computational Physics*, 226(1):586–620, 2007.
- [5] Dieter Biskamp. *Magnetohydrodynamic turbulence*. Cambridge University Press, 2003.
- [6] Stanislav Boldyrev, Åke Nordlund, and Paolo Padoan. Scaling relations of supersonic turbulence in star-forming molecular clouds. *The Astrophysical Journal*, 573(2):678, 2002.
- [7] François Bouchut, Christian Klingenberg, and Knut Waagan. A multiwave approximate riemann solver for ideal mhd based on relaxation. i: theoretical framework. *Numerische Mathematik*, 108(1):7–42, 2007.
- [8] François Bouchut, Christian Klingenberg, and Knut Waagan. A multiwave approximate riemann solver for ideal mhd based on relaxation ii: numerical implementation with 3 and 5 waves. *Numerische Mathematik*, 115(4):647–679, 2010.
- [9] Phillip Colella and Paul R Woodward. The piecewise parabolic method (ppm) for gas-dynamical simulations. *Journal of computational physics*, 54(1):174–201, 1984.
- [10] Dominik Derigs, Andrew R Winters, Gregor J Gassner, and Stefanie Walch. A novel high-order, entropy stable, 3d amr mhd solver with guaranteed positive pressure. *Journal of Computational Physics*, 317:223–256, 2016.
- [11] Dominik Derigs, Andrew R Winters, Gregor J Gassner, and Stefanie Walch. A novel averaging technique for discrete entropy-stable dissipation operators for ideal mhd. *Journal of Computational Physics*, 330:624–632, 2017.
- [12] Christoph Federrath. On the universality of supersonic turbulence. *Monthly Notices of the Royal Astronomical Society*, page stt1644, 2013.
- [13] Christoph Federrath, Ralf S. Klessen, and Wolfram Schmidt. The density probability distribution in compressible isothermal turbulence: Solenoidal versus compressive forcing. *The Astrophysical Journal*, 688(2), 2008.
- [14] B Fryxell, AC Calder, LJ Dursi, DQ Lamb, P MacNeice, K Olson, P Ricker, R Rosner, FX Timmes, JW Truran, et al. Adaptive mesh simulations of astrophysical detonations using the asci flash code. In *AIP Conference Proceedings*, volume 583, pages 223–225. AIP, 2001.
- [15] Gregor Gassner. *Discontinuous Galerkin methods for the unsteady compressible Navier-Stokes equations*. PhD thesis, Universität Stuttgart, 2009.

- [16] Gregor Gassner and David A Kopriva. A comparison of the dispersion and dissipation errors of gauss and gauss–lobatto discontinuous galerkin spectral element methods. *SIAM Journal on Scientific Computing*, 33(5):2560–2579, 2011.
- [17] Florian Hindenlang. *Mesh curving techniques for high order parallel simulations on unstructured meshes*. PhD thesis, University of Stuttgart, 2014.
- [18] Florian Hindenlang, Gregor J Gassner, Christoph Altmann, Andrea Beck, Marc Staudenmaier, and Claus-Dieter Munz. Explicit discontinuous galerkin methods for unsteady problems. *Computers & Fluids*, 61:86–93, 2012.
- [19] P. F. Hopkins. A model for (non-lognormal) density distributions in isothermal turbulence. *Monthly Notices of the Royal Astronomical Society*, 430(3):1880–1891, Aug 2013.
- [20] George Paul Horedt. *Polytropes: applications in astrophysics and related fields*, volume 306. Springer Science & Business Media, 2004.
- [21] Antony Jameson, Wolfgang Schmidt, and Eli Turkel. Numerical solution of the euler equations by finite volume methods using runge kutta time stepping schemes. In *14th fluid and plasma dynamics conference*, page 1259, 1981.
- [22] S Kitsionas, C Federrath, RS Klessen, W Schmidt, DJ Price, LJ Dursi, M Gritschneider, S Walch, R Piontek, Jongsoo Kim, et al. Algorithmic comparisons of decaying, isothermal, supersonic turbulence. *Astronomy & Astrophysics*, 508(1):541–560, 2009.
- [23] Ralf S Klessen and Simon CO Glover. Physical processes in the interstellar medium. In *Star Formation in Galaxy Evolution: Connecting Numerical Models to Reality*, pages 85–249. Springer, 2016.
- [24] Andrey Nikolaevich Kolmogorov. Dissipation of energy in the locally isotropic turbulence. *Proceedings: Mathematical and Physical Sciences*, 434(1890):15–17, 1991.
- [25] L. Konstandin, P. Girichidis, C. Federrath, and R. S. Klessen. A new density variance–mach number relation for subsonic and supersonic isothermal turbulence. *The Astrophysical Journal*, 761(2):149, 2012.
- [26] Lukas Konstandin, Wolfram Schmidt, Philipp Girichidis, Thomas Peters, Rahul Shetty, and Ralf S Klessen. Mach number study of supersonic turbulence: the properties of the density field. *Monthly Notices of the Royal Astronomical Society*, 460(4):4483–4491, 2016.
- [27] Alexei G. Krtsuk, Michael L. Norman, Paolo Padoan, and Rick Wagner. The statistics of supersonic isothermal turbulence. *The Astrophysical Journal*, 665(1):416, 2007.
- [28] Alexander Kurganov and Yu Liu. New adaptive artificial viscosity method for hyperbolic systems of conservation laws. *Journal of Computational Physics*, 231(24):8114–8132, 2012.
- [29] D Lee, G Xia, C Daley, A Dubey, S Gopal, C Graziani, D Lamb, and K Weide. Progress in development of hdp capabilities in flash’s unsplit staggered mesh mhd solver. *Astrophysics and Space Science*, 336(1):157–162, 2011.
- [30] S-C Lo, GA Blaisdell, and AS Lyrintzis. High-order shock capturing schemes for turbulence calculations. *International Journal for Numerical Methods in Fluids*, 62(5):473–498, 2010.
- [31] Mordecai-Mark Mac Low. Turbulence in the interstellar medium. In *From Observations to Self-Consistent Modelling of the ISM in Galaxies*, pages 147–155. Springer, 2004.

- [32] Mordecai-Mark Mac Low, Ralf S Klessen, Andreas Burkert, and Michael D Smith. Kinetic energy decay rates of supersonic and super-alfvénic turbulence in star-forming clouds. *Physical Review Letters*, 80(13):2754, 1998.
- [33] Wolf-Christian Müller and Dieter Biskamp. The evolving phenomenological view on magnetohydrodynamic turbulence. In *Turbulence and Magnetic Fields in Astrophysics*, pages 3–27. Springer, 2003.
- [34] Å. K. Nordlund and P. Padoan. The Density PDFs of Supersonic Random Flows. In J. Franco and A. Carraminana, editors, *Interstellar Turbulence*, page 218, 1999.
- [35] Paolo Padoan and Åke Nordlund. The stellar initial mass function from turbulent fragmentation. *The Astrophysical Journal*, 576(2):870, 2002.
- [36] Per-Olof Persson and Jaime Peraire. Sub-cell shock capturing for discontinuous galerkin methods. *44th AIAA Aerospace Sciences Meeting and Exhibit*, Sep 2006.
- [37] Paul H Roberts. Alfvén’s theorem and the frozen flux approximation. In *Encyclopedia of Geomagnetism and Paleomagnetism*, pages 7–11. Springer, 2007.
- [38] Manuel D. Salas and Angelo Iollo. Entropy jump across an inviscid shock wave. *Theoretical and Computational Fluid Dynamics*, 8(5):365–375, 1996.
- [39] Wolfram Schmidt, Christoph Federrath, Markus Hupp, Sebastian Kern, and Jens C Niemeyer. Numerical simulations of compressively driven interstellar turbulence-i. isothermal gas. *Astronomy & Astrophysics*, 494(1):127–145, 2009.
- [40] Claude Elwood Shannon. Communication in the presence of noise. *Proceedings of the IRE*, 37(1):10–21, 1949.
- [41] Zhen-Su She and Emmanuel Leveque. Universal scaling laws in fully developed turbulence. *Physical review letters*, 72(3):336, 1994.
- [42] Gary A Sod. A survey of several finite difference methods for systems of nonlinear hyperbolic conservation laws. *Journal of computational physics*, 27(1):1–31, 1978.
- [43] Matthias Sonntag and Claus-Dieter Munz. Shock capturing for discontinuous galerkin methods using finite volume subcells. In *Finite Volumes for Complex Applications VII-Elliptic, Parabolic and Hyperbolic Problems*, pages 945–953. Springer, 2014.
- [44] James M Stone, Eve C Ostriker, and Charles F Gammie. Dissipation in compressible magnetohydrodynamic turbulence. *The Astrophysical Journal Letters*, 508(1):L99, 1998.
- [45] O. Tange. Gnu parallel - the command-line power tool. *;login: The USENIX Magazine*, 36(1):42–47, Feb 2011.
- [46] Matteo Tugnoli, Antonella Abbà, Luca Bonaventura, and Marco Restelli. A locally p-adaptive approach for large eddy simulation of compressible flows in a dg framework. *arXiv preprint arXiv:1610.03319*, 2016.
- [47] Leon van Dommelen. Partial differential equations: 3.5 the inviscid burgers’ equation. webpage, 06 2017. URL: http://www.eng.famu.fsu.edu/dommelen/pdes/style_a/burgers.
- [48] S Walch, P Girichidis, T Naab, A Gatto, SCO Glover, R Wünsch, RS Klessen, PC Clark, T Peters, D Derigs, et al. The silcc (simulating the lifecycle of molecular clouds) project–i. chemical evolution of the supernova-driven ism. *Monthly Notices of the Royal Astronomical Society*, 454(1):246–276, 2015.

- [49] Andrew R Winters and Gregor J Gassner. Affordable, entropy conserving and entropy stable flux functions for the ideal mhd equations. *Journal of Computational Physics*, 304:72–108, 2016.
- [50] Akira Yoshizawa. *Hydrodynamic and Magnetohydrodynamic Turbulent Flows: Modelling and Statistical Theory*, volume 48. Springer Science & Business Media, 2013.
- [51] Meilin Yu and Zhijian Wang. On the accuracy and efficiency of several discontinuous high-order formulations. In *51st AIAA Aerospace Sciences Meeting including the New Horizons Forum and Aerospace Exposition*, page 855, 2013.